NUMERICAL SIMULATION OF UNCONVENTIONAL RESERVOIRS CONSIDERING EFFECTS OF NANOPORES USING RESERVOIR-SCALE AND PORE-SCALE APPROACHES

A Dissertation

by

JINGWEI HUANG

Submitted to the Office of Graduate and Professional Studies of
Texas A&M University
in partial fulfillment of the requirements for the degree of

DOCTOR OF PHILOSOPHY

Chair of Committee,	John E. Killough
Committee Members,	Maria A. Barrufet
	Eduardo Gildin
	Hadi Nasrabadi
Head of Department,	Jeff Spath

May 2020

Major Subject: Petroleum Engineering

ABSTRACT

Difficulties have been encountered in modelling unconventional reservoirs using traditional approaches. One of the reasons causing the failure is that the mechanisms of fluid flow, phase change etc. in nanopores have not been thoroughly investigated and understood. To study effects of nanopores, in this study, we use both reservoir-scale and pore-scale approaches which could help understand the physics of fluids in nanopores from different levels.

At reservoir scale, effects of distribution of nanopores are first studied. To incorporate pore size distribution into reservoir simulation, multi-porosity model is applied to divide shale matrix into different continua based on experimental data. Then phase behavior in different kind of pores is considered by coupling capillary pressure into vapor-liquid equilibrium of the compositional simulator. Besides, production from mixed-wet shale reservoir is studied. Mixed-wettability is modeled explicitly by dividing shale matrix into organic matter and inorganic matter. To construct relative permeability for three-phase flow, interaction between water and oil is simulated by directly performing immiscible displacement on digital rocks; relative permeability of oil and gas is obtained from calculated capillary pressure curve. Then, CO_2 injection into shale reservoir is evaluated for both enhanced gas recovery and permeant CO_2 sequestration. The dispersed nature of kerogen is characterized and its effects are comprehensively. Critical factors during CO_2 injection are evaluated including total organic carbon, injection rate and diffusion coefficient etc.

At pore-scale, a pseudo-potential lattice Boltzmann model is extended to study the phase equilibrium in nanopores. The interaction force between molecules in pseudo-potential model is associated with equation of state. The proposed model is validated by comparing equilibrium densities and saturation pressures with predictions from Maxwell construction and equation of state. Simulated interfacial tensions are found consistent with Young-Laplace equation and parachor model. The model is then applied to study the phase change under effects of interface curvature. The deviations of phase equilibrium caused by curved interface curvature is characterized by Kelvin equation. Besides, the length scales of pseudo-potential model for simulating different fluids are determined quantitatively by non-dimensionalizing the interfacial tensions. The length of the lattice spacing in pseudo-potential model is found on the order of a few angstroms due to its interfacial properties.

DEDICATION

To My wife Fengshuang Du

ACKNOWLEDGEMENTS

My deepest gratitude goes to my advisor Dr. John E. Killough for his guidance of the Ph.D. study. It’s a great honor to work with him and his broad knowledge in reservoir engineering and unreserved help make all these works happen. I am also grateful for his selfless support to investigate any topics I am interested in.

I would like to thank Dr. Maria Barrufet, Dr. Eduardo Gildin, and Dr. Hadi Nasrabadi, for being my committee members. They provided valuable guidance and support throughout the course of this work. Special thanks go to Dr. Xiaolong Yin from Colorado School of Mines, who is my advisor of master study and continue providing help for the pore-scale simulation.

I also appreciate the time spent with friends and colleagues at Dr. Killough’s group and Petroleum Engineering department. Their company and supports makes the Ph.D. study enjoyable.

Finally, I like to take this opportunity to thank my family for their endless love, supports and encouragements all the time.

CONTRIBUTORS AND FUNDING SOURCES

Contributors

This work was supported by a dissertation committee consisting of Professor John E. Killough [advisor], Professor Eduardo Gildin and Professor Hadi Nasrabadi of the Department of Petroleum Engineering and Professor Maria A. Barrufet of the Department of Chemical Engineering.

The reservoir simulator GURU was originally developed by Dr. Bicheng Yan and modified for this study. The Embedded Discrete Fracture Model (EDFM) was developed by Dr. Zhi Chai. The original pore-scale simulator was developed by Jingwei Huang under guidance of Dr. Xiaolong Yin from Colorado School of Mines. The PVT data in Chapter 3 is from Marathon Corp. The computational resources and access to supercomputers were provided by the Texas A&M High Performance Research Computing.

All the other work conducted in this study was completed by the student independently.

Funding Sources

The Graduate study was financially supported by Marathon Corp from Petroleum Engineering Department of Texas A&M University.

NOMENCLATURE

Variables

A_i	contact area between two connected grid blocks
A	parameter that controls the value of interfacial tension
B_i	weight parameters in two-phase collision operator
$\boldsymbol{c}_i$	lattice velocity
c_s	speed of sound
c_0	constant depending on the lattice structure
C_A	shape factor
$d_{m,i}$	collision diameter of component *i*
d_{nnc}	distance of the connection
$dis(x, y, z)$	distance from location (x, y, z) to the fracture
D_{ij}	binary diffusion coefficient
f_i^l	fugacity of component *i* at liquid phase
f_i^v	fugacity of component *i* at vapor phase
f_i^k	distribution function
f_j^{eq}	equilibrium distribution function
g	strength of interaction
$\mathrm{G}(\boldsymbol{x}, \boldsymbol{x}')$	Green's function
J_i	component diffusion flux
k_i	permeability of grid block

k_0	intrinsic permeability of medium
k_a	apparent gas permeability
k_{ro}	relative permeability of oil
k_{rg}	relative permeability of gas
K_i	component equilibrium ratio ($K_i = y_i/x_i$).
$K_{n,i}$	Knudsen number
L_i	nodal distance from block center to interface
m	mean value for the data set
$\boldsymbol{M}$	transformation matrix
M_i	moles of component *i* adsorbed on unit volume of rock
N_A	Avogadro’s number
Nc	number of components
$P_{L,i}$	Langmuir pressure of component *i*
p_c	critical pressure
p_r	reduced saturation pressures (p/p_c)
P^l	mechanical partial pressure of liquid phase
P^v	mechanical partial pressure of vapor phase
P_{in}	pressure inside a droplet (bubble)
P_{out}	pressure outside a droplet (bubble)
P_{cap}	capillary pressure
P^α	saturation vapor pressure with interface curvature

P_{vp}	saturation pressure when the interface is flat
q	Darcy flux rate
q_g^p	source/sink strength of gas phase
q_w^p	source/sink strength of water phase
r	pore radii
R	gas constant
R_o	initial radius of the droplet or bubble
R_r	residual of Rachford-Rice equation
s	standard deviation
$\boldsymbol{S}$	diagonal collision matrix
S_g	gas saturation
S_w	water saturation
$S_{o,r}$	residual oil saturation
T	temperature
T_c	critical temperature
T_r	reduced temperature (T/T_c)
$T_{i,j}$	inter-block transmissibility
v^β	molar volume of the liquid phase at equilibrium with the vapor phase when the interface is flat
$\boldsymbol{u}$	fluid velocity
V_i	bulk volume of grid block

$V_{L,i}$	Langmuir volume of component *i*
V_m^l	the molar volume of liquid phase
V_m^v	the molar volume of vapor phase
$w_{f,i}$	width of fracture
W	initial width of interface
x	data set
x_i	mole fraction in liquid phase
x_0 y_0 z_0	the coordinates of the center of the droplet or bubble
y_i	mole fraction in vapor phase
z_i	mole fraction composition of component *i*

Greeks

β	weighting parameter
γ	free parameter controls interface thickness
σ	interfacial tension
η	permeability multiplier
υ	fluid viscosity
θ	contact angle
ε	tolerance
τ	relaxation time
Δt	time step
ϕ	porosity

ω_i	weighting coefficient
ρ	density
ρ_R	density of red fluid
ρ_B	density of blue fluid
ρ_s	rock density
ρ_v	density of vapor phase
ρ_l	density of liquid phase
ρ_r	reduced density (ρ/ρ_c)
ρ^N	phase field function
$\tilde{\rho}_o$	molar density of oil
$\tilde{\rho}_g$	molar density of gas
$\tilde{\rho}_w$	molar density of water
$\tilde{\rho}_g^{sc}$	molar volume of gas at surface condition
λ_i	mean free path of component *i*
λ_{ro}	relative mobility of oil
λ_{rg}	relative mobility of gas
λ_{rw}	relative mobility of water
ϕ_i^l	fugacity coefficient of component *i* at liquid phase
ϕ_i^v	fugacity coefficient of component *i* at vapor phase
$\Phi_{o,i}$	potential of oil
$\Phi_{g,i}$	potential of gas

Φ_w	potential of water
Ω_i^k	collision operator
χ_i	Parachor of component
φ_i	angle between the phase field function gradient $\nabla\rho^N$ and $\boldsymbol{c}_i$
ψ	pseudopotential

Acronyms

BET	Brunauer-Emmett-Teller
BGK	Bhatnagar–Gross–Krook
CCE	constant composition expansion
CDF	cumulative distribution function
CS	Carnahan-Starling
DL	differential liberation
EDFM	embedded discrete fracture model
EDM	exact difference method
EGR	enhance gas recovery
EOS	equation of state
GOR	gas oil ratio
LB	lattice Boltzmann
MD	molecular dynamics
MINC	multiple interacting continua
MRT	Multiple-relaxation-time

NC	neighbor connection
NNC	non-neighbor connection
NR	Newton-Raphson
OGCA	oil-gas contact angle
OOIP	original oil in place
PR	Peng-Robinson
PV	pore volume
SEM	scanning-electron-microscope
SSI	successive substation iteration
TOC	total organic carbon
WOCA	water-oil contact angle

TABLE OF CONTENTS

Page

LIST OF FIGURES

Page

LIST OF TABLES

Page

CHAPTER I

INTRODUCTION [*]

1.1 Background

Shale oil reservoirs have been a major contributor to oil production in recent years due to the unconventional resource revolution (Yu et al. 2015). It is reported that the technically recoverable shale oil resource can reach 345 billion barrels around the world (Yu et al. 2018). The production of tight oil is predicted to exceed conventional oil by the year of 2040 (Jia et al. 2019). Developments of shale oil and shale gas in North America have been a huge success by using the technique of horizontal well and hydraulic fracturing. However, it is still challenging to model the production performance of shale reservoirs due to the unconventional characteristics such as the ultralow porosity / permeability, complex facture networks, effects of nanopores etc. (Yan et al. 2018a; Huang et al. 2019a). When modeling shale reservoir, one of the difficulties is that the shale reservoir often contains a high heterogeneity coming from pore size distribution in shale matrix and hydraulic/natural fractures. Another difficulty is that the physics of fluid flow, transport and phase behavior in shale matrix are much more complex than that in conventional reservoir because of the existence of nanopores. To accurately capture the

---

[*] Part of data reported in this chapter is reprinted with permission from “Compositional simulation of fractured shale reservoir with distribution of nanopores using coupled multi-porosity and EDFM method” by Huang, J., Jin, T., Chai, Z., Barrufet, M., Killough, J., 2019. Journal of Petroleum Science and Engineering, Volume 179, Pages 1078-1089, Copyright 2019 by Elsevier.
Part of data reported in this chapter is reprinted with permission from “Compositional simulation of three-phase flow in mixed-wet shale oil reservoir” by Huang, J., Jin, T., Chai, Z., Barrufet, M., Killough, J., 2020. Fuel, Volume 260, 116361, Copyright 2020 by Elsevier.

complexity of flow and transport phenomenon in shale reservoir, certain physics must be taken into consideration including gas slippage, adsorption/desorption, diffusion, wettability, geo-mechanical effect, alteration of phase behavior in nanopores etc. (Yan et al. 2018a; Du et al. 2019a).

Efforts have been made by many researchers to deal with these challenges in modeling shale reservoir. A classic method to simulate fractured reservoir is the dual porosity model introduced by Warren and Root (1963). This approach treats matrix as a storage space and source of fluids to fractures with low permeability. Fractures are assumed as flow paths with high flow capacity and low pore volume. However, the dual porosity model may not be sufficient to model shale reservoir because it cannot capture the multiple continua in shale matrix. Thus, multi-porosity models have been developed (Yan et al. 2013; Yan et al. 2016; Hinkley et al. 2013) that allow different pore systems in shale matrix. In the multi-porosity model, matrix can be subdivided into any number of pore systems with different porosity, permeability, pore size, wettability, etc. Connections within or between different pore systems can be adjusted with flexibility. To model the complex fracture systems in shale, discrete fracture model (DFM) with unstructured gridding has been used to explicitly describe fractures (Karimi-Fard et al. 2004; Sandve et al. 2012; Sun and Schechter, 2015). However, DFM requires large number of gridding around fractures and the computation cost could be very high when fracture distribution is complex. A simplified DFM method named discrete fracture network (DFN) model (Sarda et al. 2002; Basquet et al. 2005; Yan et al. 2017) has been developed to reduce the number of required grids. In DFN model, fractures are discretized based on fracture intersections and fine gridding near fractures is not required. However, DFN model can only describe intersected fractures and is difficult to be implemented in 3D (Chai et al. 2018a). Another popular method to model fractures is embedded DFM (EDFM) introduced by Lee et al. (2001). In EDFM, fracture segments within grid blocks are represented by a control volume and are connected with other fracture segments or matrix via non-neighbor connections. The advantage of EDFM is that only structured grids are required, and number of grids is significantly reduced without using local grid refinement. Li and Lee (2008) adopted EDFM to model 2D vertical fractures using a black oil model. Moinfar et al. (2014) extended the method into 3D and factures can have arbitrary dip and strike angles. Chai et al. (2018a; 2018b) coupled EDFM and multi-porosity model that allows different pore systems in shale matrix together with complex fracture distributions.

1.1.1 Distribution of nanopores in shale

The pore size in shale varies from several to hundreds of nanometers (Kuila and Prasad 2013; Pommer 2014; Clarkson et al. 2013) as the examples shown in Figure 1.1. Since the size of most pores are in the magnitude of nanometers, the permeability of shale matrix is extremely low. Fluid flow in shale matrix is therefore non-Darcy and different physics need to be considered in nanopores such as gas slippage, diffusion, adsorption/desorption, and phase behavior under confinement. For instance, kerogen in shale has large capacity for adsorbed gas and gas adsorption/desorption in nanopores has significant effect on shale gas production (Ambrose et al. 2011; Yan et al. 2018b). In shale matrix, the mean free path of gas is comparable to the characteristic length of nanopores where gas slippage and Knudsen diffusion become important (Civan 2010; Javadpour 2009). Moreover, the large capillary pressure and fluid-solid interactions in nanopores can result in a different phase behavior of fluids compared to that in bulk condition. Nojabaei et al. (2013) studied the effect of capillary pressure on the phase behavior of Bakken oil. Du et al. (2018) considered high capillary pressure in their EOR study with injection of produced gas. Stimpson and Barrufet (2016) proposed a rigorous method to calculate capillary pressure in nanopores by coupling Young-Laplace equation with flash calculation. Siripatrachai et al. (2017) studied how capillary pressure affects original oil in place (OOIP) and oil production by compositional simulations. In most of the work considering effect of capillary pressure on phase behavior, suppressed bubble points were observed. On the other hand, some studies show that there is a shift of critical point for confined fluids. Zarragoicoechea and Kuz (2004) studied the critical shift of pure components in nanopores using a generalized van der Waals equation of state. Travalloni et al. (2014) extended Peng-Robinson equation of state to study the critical behavior of fluids in tight porous media. Li and Sheng (2017) investigated both capillary pressure's and critical shift's effect on phase equilibrium.

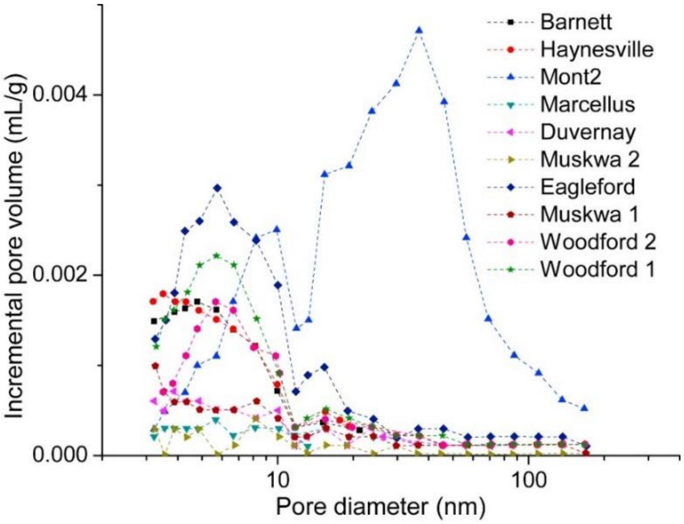

Figure 1.1: Pore size distributions of shale samples from shale gas reservoirs in North America (reprinted from Clarkson et al. 2013).

1.1.2 Mixed wettability in shale

The subsurface flow in shale oil reservoir often involves an oil phase, a gas phase and water. Modeling the interactions among the three phases are critical for numerical simulation and production forecast of shale oil reservoir. Relative permeability has been widely used to characterize multiphase flow in porous media. In a two-phase system, it is straightforward to measure the relative permeabilities since only two possible saturation paths exist (Kianinejad et al. 2015). In a three-phase system, relative permeabilities can be functions of any saturation and direct measurement is difficult (Kianinejad et al. 2015). Measurements of relative permeability can be classified into steady state and unsteady state methods (Fassihi and Potter 2009). The number of three-phase flow experiments is limited, and even contradictory results were reported (Skauge and Larsen 1994; Eleri et al. 1995; Alizadeh and Piri 2014). Some experimental data demonstrate that the permeabilities of strongly wetting phase or nonwetting phase primarily depend on their own saturations and are weak functions of saturations of other phases (Baker 1988; Saraf and Fatt 1967; Corey et al. 1956). The intermediate-wetting phase is more influenced by other phases and may show hysteresis (Baker 1988). In other cases, however, the dependency of intermediate-wetting phase's permeability on saturations of other phases is not apparent (Baker 1988). Theoretical and empirical models have been proposed to fit the experimental data such as the models of Corey et al. (1956), Stone (1970; 1973), Naar and Wygal (1961), Land et al. (1968) and each model has its assumptions and application range. However, it has been reported that these existing models are hard to match experimental results (Spiteri et al. 2008; Shahverdi et al. 2011). In reservoir simulation, relative permeabilities are obtained by history matching the production data. For unconventional reservoir, it is more difficult to measure relative permeability by experiment due to the ultralow permeability of shale rocks (Xiao and Yin 2016). The measurements are time-consuming, expensive and results are hard to interpret (Xiao and Yin 2016). In recent years, pore-scale direct numerical simulation has been proven an efficient tool to calculate relative permeability in porous media (Huang et al. 2017; Pan et al. 2004). With the advance of imaging techniques and high-performance computing, it is possible to directly simulate multiphase flow and transport on digital rock samples reconstructed from scanned images (Huang et al. 2017; Dong and Blunt 2009; Huang et al. 2019b).

Recent studies show that the shale rock contains different minerals that can be classified into inorganic matter and organic matter (Yassin 2016; Yan et al. 2018b). The inorganic matter includes quartz, feldspar, dolomite, clays and the organic matter is primarily pyrobitumen (Yassin et al. 2016). The petrophysical properties of organic and inorganic matter are obviously distinct and should be treated independently (Yan et al. 2018b). From the FIB/SEM image in Figure 1.2, it is seen that micropores primarily exist within the inorganic matter, while nanopores are widely distributed in organic matter. Thus, the organic matter has much smaller pore sizes and lower permeability than the inorganic matter. Meanwhile, it has been pointed out that the organic matter is a dispersed phase inside the inorganic matter and connectivity between organic matter is poor (Olorode et al. 2017). Therefore, it is essential to divide the shale matrix into organic matter and inorganic matter (Olorode et al. 2017). Besides, dual-wettability condition has been investigated in shale rock, that is the organic matter is strongly hydrophobic while the inorganic matter is hydrophilic. It is known that wettability is a strong factor that affects relative permeabilities. Extensive work has been conducted to study relative permeability in porous media under the condition of uniform wettability (Baker 1988; Huang et al. 2017; Pan et al. 2004). It has been found that the non-wetting phase tends to path through larger pores while the wetting phase occupies the small pores. Therefore, a larger relative permeability is often observed for non-wetting phase (Yassin et al. 2006). However, due to the mixed-wet condition in shale rock, the relative permeabilities obtained under uniform-wet condition may not be suitable for modeling shale reservoir. Theoretical analysis and experimental measurements have been applied to study relative permeability in mixed-wet porous media (Landry et al. 2014; Jackson et al. 2003; Jerauld and Rathmell 1997). Capillary pressure-saturation-relative permeability relations are measured in mixed-wet porous media and models are proposed to interpret the results

(Landry et al. 2014). It is reported that oil-water system is more influenced by mixed wettability and gas-water system is not sensitive to wettability due to the small contact angle (Landry et al. 2014). Pore-scale numerical simulation has also been used to model multiphase flow under mixed-wet condition (Piri and Blunt 2005a; Piri and Blunt 2005b). The simulation results show that the effect of mixed wettability on non-wetting phase is more pronounced than wetting phase (Landry et al. 2014).

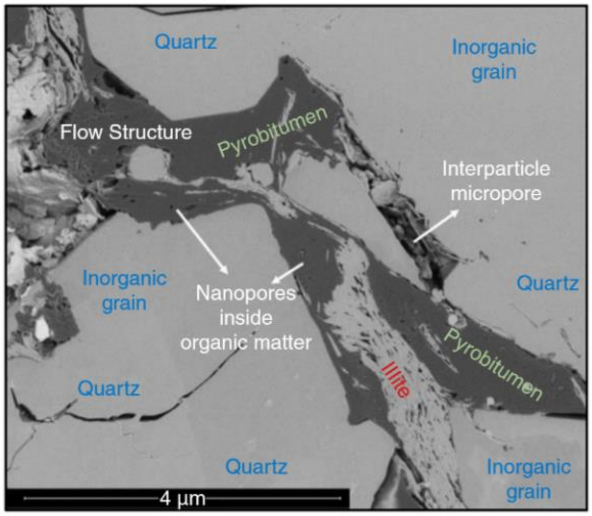

Figure 1.2 FIB/SEM image of a shale sample, reproduced from (reprinted from Yassin et al. 2016).

1.2 Study Objectives

To include pore size distribution into shale reservoir simulation and better investigate the effects of pore size distribution, a multi-porosity model is applied to represent the shale matrix and each matrix grid is subdivided into different continua based on experimental pore size data. Each continuum can have its own petrophysical properties such as pore size, permeability, porosity etc. Besides, EDFM approach is used in to model fractures on top of matrix which allows to model complex fracture systems in shale at the same time.

On the other hand, we notice that there are limited number of works studying multicomponent three-phase flow in shale oil reservoir, especially under the condition of mixed wettability. In this work, the different minerals in shale reservoir are distinguished and the mixed wettability is studied explicitly. Specifically, the shale matrix is first divided into organic matrix and inorganic matrix which are hydrophobic and hydrophilic respectively. The organic matrix has a smaller pore size and lower permeability than the inorganic matrix. To include the effects of wettability, relative permeabilities under different contact angles are calculated independently for both organic and inorganic matrix.

Moreover, apart from simulation of shale reservoirs using continua approaches, pore-scale simulation is also an efficient tool to study fluid flow, phase change and transport process in porous media, especially when dealing with nanopores. In this study, the lattice Boltzmann method is applied to study the physics of fluids in nanopores from a more fundamental level such as phase behavior under confinement and adsorption phenomenon. Knowledge learned from pore-scale studies can be applied into the reservoir-scale simulation.

1.3 Organization of the Dissertation

The rest of the dissertation is organized as follows: First, models at reservoir-scale are introduced including the multi-porosity model, EDFM approach and formulation of a multi-physics compositional simulator. Then, the procedure for incorporating pore size distribution and its effects on simulation of production are evaluated. Next, the mixed-wet condition in shale is characterized and three-phase relative permeability is built. Compositional simulation is then conducted including production from a fractured shale oil reservoir and gas injection into a shale gas reservoir. Besides, the pore-scale approach (a multiphase lattice Boltzmann method) is introduced and it is applied to model phase behavior and adsorption in nanopores. Results are compared with large-scale simulation and experimental results.

The details of each Chapter in the dissertation are described as follows:

Chapter I: Introduction to the background, motivations, and objectives of this study.

Chapter II: Models for reservoir-scale simulation: multi-porosity model, EDFM approach and formulations of compositional simulator.

Chapter III: The reservoir-scale models are applied to predict productions from shale reservoirs considering pore size distribution. Three-phase flow in shale reservoir under mixed-wet condition is modeled by separating matrix into organic matter and inorganic matter.

Chapter IV: CO_2 injection into shale gas reservoir is evaluated for both enhanced gas recovery and permanent CO_2 sequestration. The effect of dispersed distribution of kerogen is specifically studied.

Chapter V: A pseudo-potential based lattice Boltzmann model is built and validated.

Chapter VI: The lattice Boltzmann model is applied to model phase change under effect of interface curvature and results are compared with Kelvin equation. Adsorption is simulated by incorporating a fluid-solid interaction.

Chapter VII: Conclusions of this study and recommendations for future work are presented.

CHAPTER II

RESERVOIR-SCALE MODELS FOR UNCONVENTIONAL RESERVOIR SIMULATION[*]

2.1 Multi-porosity model

In this work, a multi-porosity model proposed by Yan et al. (2013) is implemented to describe the complex pore systems in shale matrix. In this model, any number of continua in shale matrix can be generated with different petrophysical properties including porosity, permeability, pore size, wettability etc. Mass transfer can take place within each type of continua (intra-connection) or between different types of continua (inter-connection). Thus, this model is flexible in modeling various types of continua in matrix with different properties and connectivities. Assume Darcy's law applies to the multi-porosity model, the mass transfer between different continua can be expressed as

$$q = T_{i,j}[\lambda_{ro}\tilde{\rho}_o x_i(\Phi_{o,i} - \Phi_{o,j}) + \lambda_{rg}\tilde{\rho}_g y_i(\Phi_{g,i} - \Phi_{g,j})] \tag{2.1}$$

where q is the Darcy flux rate, λ_{ro} and λ_{rg} are the relative mobility of oil and gas respectively, $\tilde{\rho}_o$ and $\tilde{\rho}_g$ are the molar density of oil and gas respectively, $\Phi_{o,i}$ and $\Phi_{g,i}$ are

---

[*] Part of data reported in this chapter is reprinted with permission from "Compositional simulation of fractured shale reservoir with distribution of nanopores using coupled multi-porosity and EDFM method" by Huang, J., Jin, T., Chai, Z., Barrufet, M., Killough, J., 2019. Journal of Petroleum Science and Engineering, Volume 179, Pages 1078-1089, Copyright 2019 by Elsevier.
Part of data reported in this chapter is reprinted with permission from "Compositional simulation of three-phase flow in mixed-wet shale oil reservoir" by Huang, J., Jin, T., Chai, Z., Barrufet, M., Killough, J., 2020. Fuel, Volume 260, 116361, Copyright 2020 by Elsevier.

the potential of oil and gas respectively, $T_{i,j}$ is the inter-block transmissibility that can be calculated by harmonic average

$$T_{i,j} = T_i T_j / (T_i + T_j) \tag{2.2}$$

In multi-porosity model, the half-block transmissibility T_i includes neighbor connection (NC) and non-neighbor connection (NNC). NC happens within the same continuum while NNC are between different continua and they can be expressed as

$$T_i = \begin{cases} k_i A_i / L_i & , NC \\ C_A V_i k_i & , NNC \end{cases} \tag{2.3}$$

where k_i is permeability of grid block, A_i is contact area between two connected grid blocks, L_i is nodal distance from block center to interface, V_i is bulk volume of grid block, C_A is shape factor.

2.2 EDFM approach

To describe the complex fracture systems in shale, the enhanced embedded discrete fracture model (EDFM) is applied in this work (Chai et al. 2018). By combining the multi-porosity model and EDFM approach, we are able to model the multiple continua in matrix (organic and inorganic) together with fractures. When using EDFM, the macro/micro fractures including hydraulic fractures/natural fractures are described explicitly with any strike and angles. The transmissibility between fractures and matrix grid block can be derived analytically. In EDFM implementation, three kinds of non-neighbor connection need to be considered including 1) connections between fracture and matrix grid blocks, 2) between two intersecting fracture grids and 3) between two neighboring fracture grids in the same fracture (Chai et al. 2018). Transmissibility in NNC type I can be written as

$$T_{nnc} = \frac{A_{nnc} k_{nnc}}{d_{nnc}} \tag{2.4}$$

where A_{nnc} is the contact area, k_{nnc} is the harmonic average of fracture permeability of fracture (k_f) and matrix (k_m)

$$k_{nnc} = \frac{2}{k_f^{-1} + k_m^{-1}} \tag{2.5}$$

d_{nnc} is distance of the connection that can be determined by

$$d_{nnc} = \frac{\int_v dist(x,y,z) dv}{V} \tag{2.6}$$

where $dis(x, y, z)$ is the distance from location (x, y, z) to the fracture, V is the bulk volume of grid block. For NNC type II and III, transmissibility is given as

$$T_{nnc} = \frac{1}{T_i^{-1} + T_j^{-1}} \tag{2.7}$$

The half-transmissibility is calculated by (Chai et al. 2018)

$$T_i = \frac{k_{f,i} \times l_{f1,f2} \times min(w_{f,i}, w_{f,j})}{d_{f,i}} \tag{2.8}$$

where $k_{f,i}$ is the permeability of fracture *i*, $l_{f1,f2}$ is length of connection, $w_{f,i}$ and $w_{f,i}$ are the width of fracture *i* and *j* respectively, $d_{f,i}$ is the characteristic distance.

2.3 Compositional simulation considering effects of nanopores

2.3.1 Formulation of compositional simulator

After building the multi-continua reservoir model, simulation of shale reservoir is conducted using the in-house compositional simulator GURU (Yan et al. 2017). The simulator uses a controlled-volume finite difference method and different physics can be applied in different types of continua based on their petrophysical properties. The gas mass balance equation for component *i* (*i* = 1, …, N_c) can be generally written as

$$\frac{V}{\Delta t}\Delta\left(\phi S_g \tilde{\rho}_g y_i\right) + \frac{V}{\Delta t}\Delta M_i + S_g J_i - \sum T\left(\lambda_g \tilde{\rho}_g y_i \Delta\Phi_g\right) - \sum_{well} \tilde{\rho}_g y_i q_g^p = 0 \qquad (2.9)$$

where ϕ is porosity, S_g is the gas saturation, y_i is the mole fraction of component i, q_g^p is the source/sink strength of gas phase, M_i is the number of moles of component *i* adsorbed on unit volume of rock, J_i is the component diffusion flux. In the mass balance equation, the first term on the left-hand side represents the accumulation of component *i* in compressed storage, the second term is the accumulation of component *i* by adsorption/desorption, the third term is the flux from molecular diffusion, the fourth term is the flux from pressure gradient, and the last term represents the well term (source or sink). The general extended Langmuir model is used for calculation of adsorption/desorption (Yan et al. 2018b)

$$M_i = (1-\phi)\rho_s \tilde{\rho}_g^{sc} \frac{V_{L,i} y_i \frac{P}{P_{L,i}}}{1 + \sum y_i \frac{P}{P_{L,i}}} \qquad (2.10)$$

where ρ_s is rock density, $\tilde{\rho}_g^{sc}$ is the molar volume of gas at surface condition, $V_{L,i}$ is Langmuir volume of component *i*, $P_{L,i}$ is Langmuir pressure of component *i*. The generalized Fick's model is applied to simulate the molecular diffusion of nonideal gas mixtures. The generalized Fickian diffusion flux can be expressed by (Alharthy et al. 2018)

$$J_i = -\tilde{\rho}_g \sum_{j=1}^{Nc-1} D_{ij} \nabla y_j \ , i = 1, \dots, Nc - 1 \qquad (2.11)$$

where D_{ij} is the binary diffusion coefficient. In our model, the phase behavior of shale gas is calculated using Peng-Robinson (PR) equation of state and gas viscosity is calculated using Lohrenz-Bray-Clark method.

The shale gas reservoir is extremely tight and the pore size in shale matrix is in the order of several to hundreds of nanometers (Pommer et al. 2015). Thus, the effect of non-Darcy flow should be considered such as gas slippage and Knudsen diffusion. The gas flow in nanopores in shale matrix can be corrected by using the apparent gas permeability (Yan et al. 2018b)

$$k_a = \begin{cases} \eta k_0, & if\ grid\ is\ in\ shale\ matrix \\ k_0, & otherwise \end{cases} \tag{2.12}$$

where k_a is the apparent gas permeability, k_0 is the intrinsic permeability of medium, η is the permeability multiplier which is a function of Knudsen number $K_{n,i}$ (Civan et al. 2011)

$$\eta_i = (1 + \frac{128K_{n,i}}{15\pi^2} arctan(4K_{n,i}^{0.4})) \times (1 + \frac{4K_{n,i}}{1+K_{n,i}}) \tag{2.13}$$

Knudsen number is defined as

$$K_{n,i} = \frac{\lambda_i}{r} \tag{2.14}$$

where *r* is pore radii and λ_i is the mean free path of component *i* which can be calculated by (Jiang and Younis 2016)

$$\lambda_i = \frac{1}{\sqrt{2}\pi\tilde{\rho}_g N_A d_{m,i}^2} \tag{2.15}$$

where N_A is Avogadro's number, $d_{m,i}$ is collision diameter of component *i*.

Similarly, the mass balance equation of water is

$$\frac{V}{\Delta t}\Delta(\phi S_w \tilde{\rho}_w) - \sum T(\lambda_{rw}\tilde{\rho}_w \Delta\Phi_w) - \sum_{well}\tilde{\rho}_w q_w^p = 0 \tag{2.16}$$

where S_w, λ_{rw}, $\tilde{\rho}_w$, Φ_w and q_w^p are the saturation, relative mobility, molar density, potential and source/sink strength of water respectively.

2.3.2 Vapor-liquid equilibrium with capillary pressure

In compositional simulation, vapor-liquid equilibrium (VLE) method is used to calculate oil and gas properties. In VLE, an equilibrium state is reached when material and chemical balance are both satisfied. The material balance can be described by Rachford-Rice equation (1952) given as

$$R_r = \sum_{i-1}^{N_c} \frac{z_i(K_i-1)}{1+f_v(K_i-1)} = 0 \tag{2.17}$$

where f_v is the mole fraction of vapor, z_i is mole fraction composition of component i, N_c is number of components and K_i is component equilibrium ratio ($K_i = y_i/x_i$). In chemical thermodynamics, fugacity of a real gas is used to describe the chemical equilibrium. Fugacity of a component in a hydrocarbon mixture can be expressed by

$$f_i^l = x_i \phi_i^l P^l \tag{2.18a}$$

$$f_i^v = y_i \phi_i^v P^v \tag{2.18b}$$

where f_i^l and f_i^v are fugacity of component *i* at liquid and vapor phase, ϕ_i^l and ϕ_i^v are fugacity coefficient of component *i* at liquid and vapor phase, P^l and P^v are mechanical partial pressure of liquid and vapor phase. The fugacity coefficient can be determined by equation of state (EOS). In this study, Peng-Robinson EOS is applied and detailed calculations of fugacity coefficients are shown in Appendix A.

The chemical balance is reached when fugacity in liquid phase equals to that in vapor phase and it can be described as

$$R_{f,i} = lnK_i + ln\phi_i^v - ln\phi_i^l + lnP^v - lnP^l = 0 \tag{2.19}$$

At bulk condition (condition of large volume), it is convenient to assume that the partial pressure of liquid phase P^l equals to that of vapor phase P^v. In confined space such as nanopores, the difference between liquid and vapor pressures can be significant. One simple method to describe the pressure difference is the Young-Laplace equation

$$P_{cap} = |P^v - P^l| = 2\sigma cos\theta/r \tag{2.20}$$

where P_{cap} is capillary pressure, σ is the interfacial tension and θ is contact angle. The interfacial tension σ is dependent on phase composition and can be determined by Parachor model proposed by Weinau and Katz (1943)

$$\sigma^{1/4} = \sum_{i=1}^{N_c} \chi_i (x_i/V_m^l - y_i/V_m^v) \tag{2.21}$$

where χ_i is the Parachor of component, V_m^l and V_m^v are the molar volume of liquid and vapor phase.

In a previous work, a combining Successive Substitution Iteration method (SSI) and Newton-Raphson (NR) method is used to solve the conventional flash calculation (Yan et al. 2017). With initial guess of K_i, Eqn. (2.17) is solved first using SSI scheme to determine mole fraction of vapor (f_v) and composition in each phase (x_i, y_i). Then fugacity can be calculated and K_i is updated by

$$K_i^{n+1} = K_i^n (f_i^l/f_i^v)^n \tag{2.22}$$

until

$$\sum_{i=1}^{N_c} \left(f_i^l/f_i^v - 1\right)^2 < \varepsilon \tag{2.23}$$

, ε is the tolerance. When tolerance is reduced to lower than 10^{-2} or iteration times go beyond 5, SSI is terminated and NR process is activated. In this way, SSI is actually used to provide a good initial guess for NR. In NR, Eqn. (2.17) and Eqn. (2.19) are solved simultaneously. The logarithm of equilibrium ratio lnK_i and mole fraction of vapor f_v are used to construct Jacobian matrix and residual factor respectively. Gaussian elimination with partial pivoting is used to solve the linear matrix (Yan et al. 2017).

In order to incorporate capillary pressure into flash calculation rigorously, we apply the methodology proposed by Stimpson and Barrufet (2016). In their method, capillary pressure is updated within every loop, parallel to the calculation of fugacity. Flash calculation is first conducted with a capillary pressure ($P_{cap[}^{old}$) (in first loop, an initial guess of capillary pressure is used which is zero in this work). With calculated x_i, y_i, V_m^l, V_m^v, a new capillary pressure (P_{cap}^{new}) can be obtained in current loop. In the next loop, capillary pressure is updated by

$$P_{cap}^{old,n+1} = 0.5(P_{cap}^{old,n} + P_{cap}^{new,n}) \tag{2.24}$$

Therefore, another convergence criterion is needed to determine the equilibrium

$$\left|P_{cap}^{old,n} - P_{cap}^{new,n}\right| < \varepsilon \tag{2.25}$$

When convergence criteria in Eqn. (2.23) and Eqn. (2.25) are both satisfied, an equilibrium state is considered to be reached.

CHAPTER III

COMPOSTIONAL SIMULATION CONSDERING EFFECTS OF NANOPORES *

3.1 Introduction

In previous works, a single continuum is often used to represent shale matrix and effect of pore size were studied by running multiple simulations with different pore sizes. However, the shale matrix has a wide range of pore size distribution, from several to hundreds of nanometers (Kuila and Prasad 2013; Pommer 2014). In different size of nanopores, fluids may have different flow properties and phase behavior. Thus, a single continuum approach cannot capture the co-existing of fluids with different flow and phase properties in a same grid block. Some researchers studied pore size distribution by assigning different pore sizes to grid blocks in different locations (Jimenez et al. 2018). Such an assignment is not physical since pore size distribution should be in every grid block in reservoir-scale simulation. Besides, mixed-wet condition has been well recognized in shale rock which will greatly affect the multiphase flow. Thus, in this Chapter, we aim to study the effects of pore-size distribution and mixed wettability using proposed reservoir-scale approaches.

---

[*] Part of data reported in this chapter is reprinted with permission from "Compositional simulation of fractured shale reservoir with distribution of nanopores using coupled multi-porosity and EDFM method" by Huang, J., Jin, T., Chai, Z., Barrufet, M., Killough, J., 2019. Journal of Petroleum Science and Engineering, Volume 179, Pages 1078-1089, Copyright 2019 by Elsevier.

Part of data reported in this chapter is reprinted with permission from "Compositional simulation of three-phase flow in mixed-wet shale oil reservoir" by Huang, J., Jin, T., Chai, Z., Barrufet, M., Killough, J., 2020. Fuel, Volume 260, 116361, Copyright 2020 by Elsevier.

3.2 Effect of pore-size distribution

3.2.1 Shale matrix subdivision based on pore size distribution

In this part, the shale matrix is subdivided into multiple continua based on pore size distribution data. Pommer et al. (2015) evaluated pore size distributions from multiple Eagle Ford core samples and they found that the pore sizes in shale yields a lognormal distribution. To describe a lognormal distribution, the cumulative distribution function (CDF) can be applied which is expressed as

$$\mathrm{CDF} = \frac{1}{2}\left[1 + \mathrm{erf}\left(\frac{\ln x - m}{\sqrt{2}s}\right)\right] \tag{3.1}$$

where m and s are the mean value and standard deviation for the data set respectively.

The shale sample studied in this work is from an anonymous oilfield in north America**.** Figure. 3.1 shows the pore size distribution from Brunauer-Emmett-Teller (BET) analysis as well as the simple regression of CDF. As shown, CDF can well describe pore size distribution of this sample. It is also observed that the pore size of this shale sample varies from several nanometers to two hundred nanometers, and more than 50% pore volume are occupied by the pores with diameter less than 30 nm. To include pore size distribution in simulation, the multi-porosity model is applied to subdivide the matrix into different continua with different pore sizes. In this study, three cases with different number of continua in shale matrix are tested, which has one continuum, two continua and three continua respectively. Based on the fitted CDF data, we use pore volume (PV) averaged pore diameter, which is 38.8 nm for the one continuum case. And for the two continua case, the total pore volume is subdivided into two parts. As shown in Figure 3.1(b): one continuum occupies 82% PV with an average pore diameter of 25.7 nm

(IA+IB), and the other continuum occupies 18% PV with an average pore diameter of 116.7 nm (II). The three continua case further divides the first continuum (IA+IB) in two continua case into another two continua: one that occupies 67% PV with an average diameter of 18.6 nm (IA), and the other occupies 15% PV with an average diameter of 58.6 nm (IB). The detailed information of every continuum is summarized in Table 3.1.

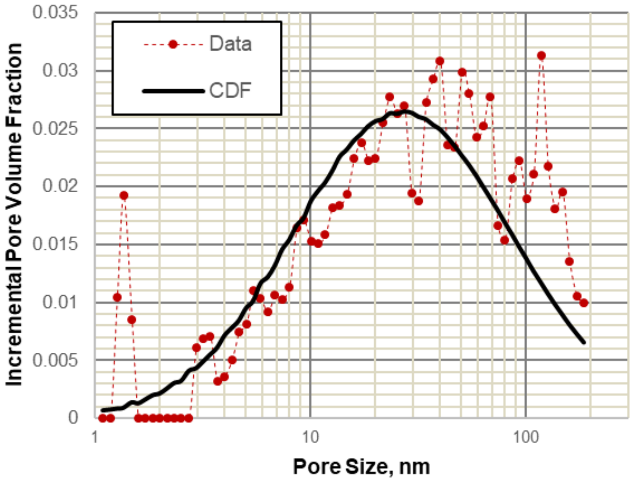

(a)

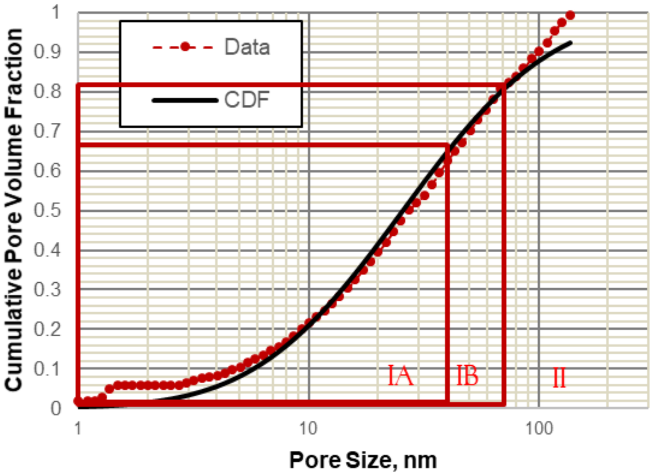

(b)

Figure 3.1 Pore size distribution of rock sample, (a) incremental distribution, (b) cumulative distribution (μ=3.245, σ=1.160).

Table 3.1 Matrix subdivision using different number of continua

<table>
<tr><th>Type</th><th colspan="6">Pore size and volume fraction</th></tr>
<tr><td>One continuum</td><td colspan="6">38.8 nm (100%)</td></tr>
<tr><td>Two continua</td><td colspan="3">25.7 nm (82%)</td><td colspan="3">116.7 nm (18%)</td></tr>
<tr><td>Three continua</td><td colspan="2">18.6 nm (67%)</td><td colspan="2">58.6 nm (15%)</td><td colspan="2">116.7 nm (18%)</td></tr>
</table>

3.2.2 Compositional simulation of fractured shale reservoir

In this part, compositional simulation is conducted in a fractured 2D reservoir model as shown in Figure 3.2. By using EDFM, the complex fractures with different angles and intersections can be modeled. The red lines represent hydraulic fractures and the green lines represent natural fractures. All the hydraulic fractures are perforated, and the horizontal well is constrained by a constant bottom-hole pressure. No flow boundary condition is applied in the outer boundary of this reservoir model. The basic parameters of this reservoir are presented in Table 3.2. As stated in Section 3.2.1, the shale matrix is further subdivided into different continua with different pore sizes. The petrophysical properties of these continua are summarized in Table 3.3. Porosity of each continuum is calculated based on its pore volume fraction in Table 3.1. Permeability of each continuum is obtained by a correlation between pore size, porosity and permeability which is given by (Aguilera 2014)

$$k = 100\phi\left(\frac{0.001r}{2.665}\right)^{1/0.45} \tag{3.2}$$

where r is pore radius.

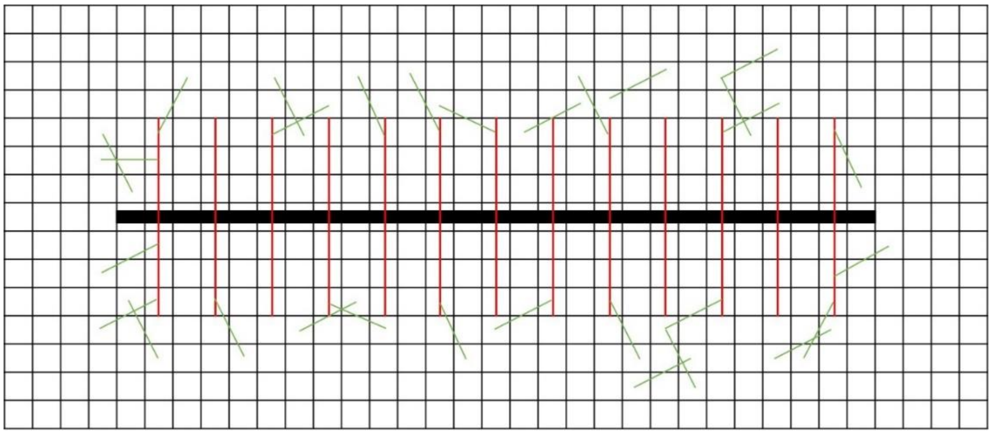

Figure 3.2 Fractured shale reservoir model for case study (hydraulic fracture-red; natural fracture-green).

Table 3.2 Basic parameters for fractured shale reservoir model

Reservoir conditions	
Initial Pressure (Psia)	3500
Initial Temperature (^oF)	165
Producer BHP (Psia)	500
Matrix	
Grid number	35 x 15 x 1
Grid size (ft)	50 x 50 x 50
Porosity (fraction)	0.08
Water saturation (fraction)	0.12
Hydraulic Fracture	
Fracture number	13
Fracture half length (ft)	175
Fracture conductivity (mD.ft)	500
Natural Fracture	
Fracture number	30
Fracture conductivity (mD.ft)	0.005

Table 3.3 Petrophysical properties of different type of continua in shale matrix

Case 1	Parameter	Continuum 1		
	Diameter(nm)	38.8		
	Porosity	0.08		
	Permeability(md)	1.420E-04		
Case 2	Parameter	Continuum 1	Continuum 2	
	Diameter(nm)	25.7	116.7	
	Porosity	0.0656	0.0144	
	Permeability(md)	4.661E-05	2.953E-04	
Case 3	Parameter	Continuum 1	Continuum 2	Continuum 3
	Diameter(nm)	18.6	58.6	116.7
	Porosity	0.0536	0.012	0.0144
	Permeability(md)	1.856E-05	5.324E-05	2.953E-04

The fluid model used in this study is a volatile oil from an anonymous oilfield in north America. The initial compositions are grouped into five pseudo-components for simulation. The properties of compositions and the binary interaction coefficients are presented in Table 3.4 and Table 3.5 respectively. The properties of these pseudo-components are calculated and calibrated by comparing the simulated results with those from PVT experiment. Under reservoir temperature (165 ^{o}F), the bubble point from flash calculation is 3411 Psi, compared to experimental result which is 3406 psi. Other properties such as density and viscosity of this fluid can be well reproduced using our fluid model, comparing to those from constant composition expansion (CCE) and differential liberation (DL) experiments (Figure 3.3). Using calibrated fluid model, the same mole fractions of composition are initialized in every kind of continua. Rock-fluid interaction can also be applied in different continua such as relative permeability and contact angle. In this study, a constant contact angle (30°) is used and relative permeability shown in Figure 3.4 is applied in shale matrix and fractures. Note that initial water saturation is 0.1 which is under irreducible saturation.

Table 3.4 Composition data of fluid model

Component	Mole fraction (%)	Critical Pressure (psia)	Critical temperature (°F)	Acentric factor	Mole weight	Parachor
CO_2	0.001924	1069.87	87.89	0.22450	44.01	78
N_2+C_1	0.503155	661.78	-120.18	0.00899	16.26	76.18
C_2-C_3	0.139236	661.59	148.59	0.12527	35.83	130.62
C_4-C_6	0.104671	492.99	371.24	0.23813	69.32	227.18
C_{7+}	0.251013	277.38	811.47	0.76355	198.88	785.52

Table 3.5 Binary interaction coefficient of fluid model

	CO_2	N_2+C_1	C_2-C_3	C_4-C_6	C_{7+}
CO_2	-	0	0	0	0
N_2+C_1	0	-	0	0	0
C_2-C_3	0	0	-	0	0
C_4-C_6	0	0	0	-	0.009
C_{7+}	0	0	0	0.009	-

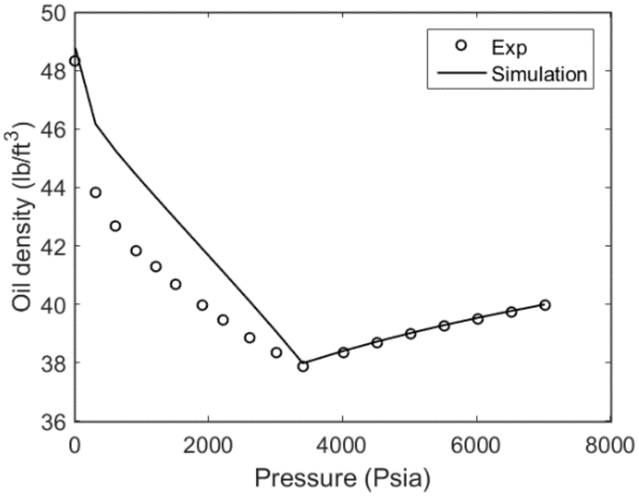

(a)

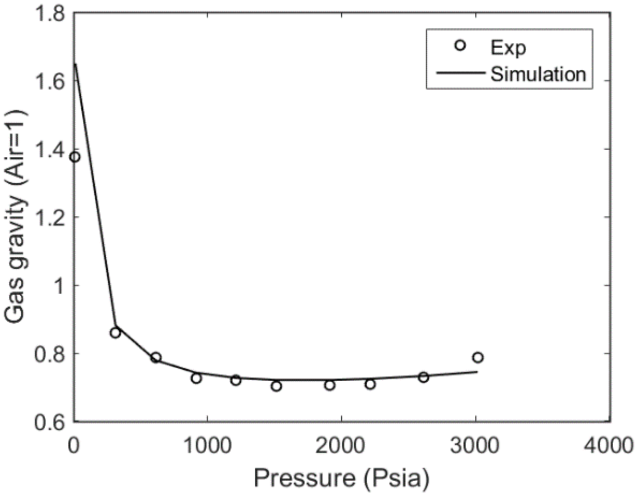

(b)

Figure 3.3 Comparison of PVT results from experiment and flash calculation; (a) Oil density, (b) Gas gravity, (c) Oil viscosity, (d) Gas viscosity.

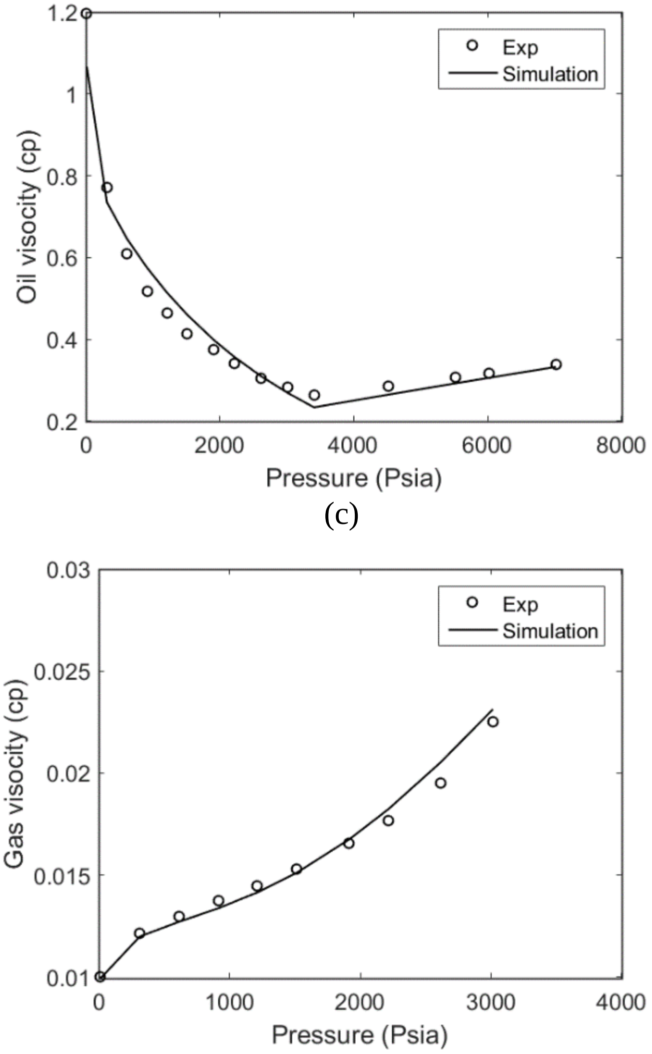

(c)

(d)

Figure 3.3 Continued.

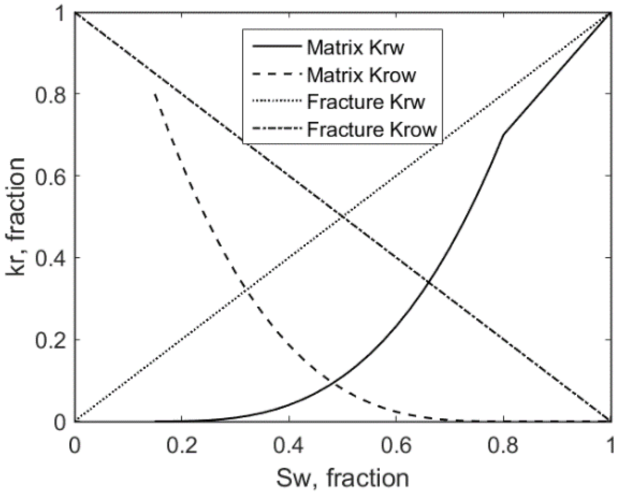

(a)

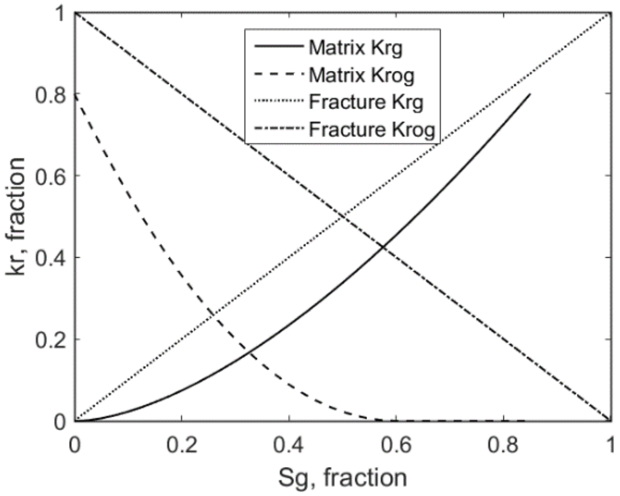

(b)

Figure 3.4 Oil and water relative permeability in matrix and fracture (a); Oil and gas relative permeability in matrix and fracture (b).

The reservoir performance using different number of continua are compared in Figure 3.5. It is seen that there is faster pressure decline when a single continuum is used in shale matrix. The pressures using two continua and three continua are close. The different performance of pressure decline should be due to the existence of low permeable continuum when using multiple continua in matrix. For instance, 82% of pore volume in case 2 is occupied by the continuum that has permeability of 4.661E-05 md. Though the other continuum has a higher permeability (2.953E-04 md) than that in case 1 (1.420E-04 md), the upscaled permeability is still lower in case 2 which leads to a higher pressure. In case 3, the lower permeable continuum in case 2 is further divided into two continua which has 1.856E-05 md and 5.324E-05 md permeability respectively. The subdivision of low permeable continuum does not have a significant effect in terms of pressure. Besides, a lower GOR is observed when using multiple continua because of the relatively higher pressure. From Figure 3.5, the oil production rates using multiple continua are lower than that using single continuum at early production period and then becomes higher at later period. Though having close average pressure, the three continua case has a higher oil rate than two continua case. The gas production rates, on the other hand, are always lower when using multiple continua and there is small difference between two and three continua cases.

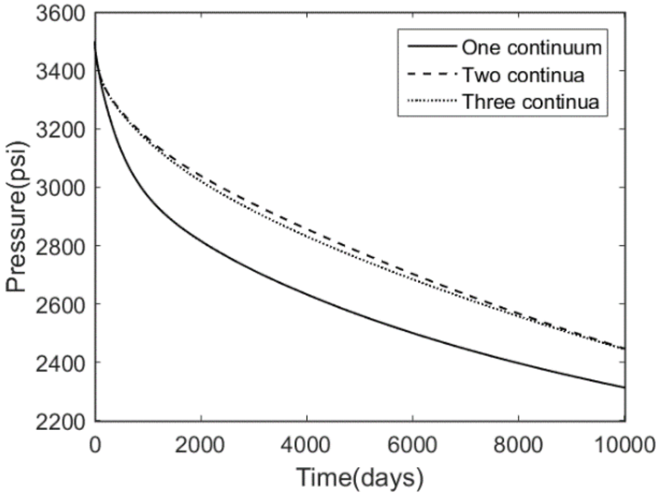

(a)

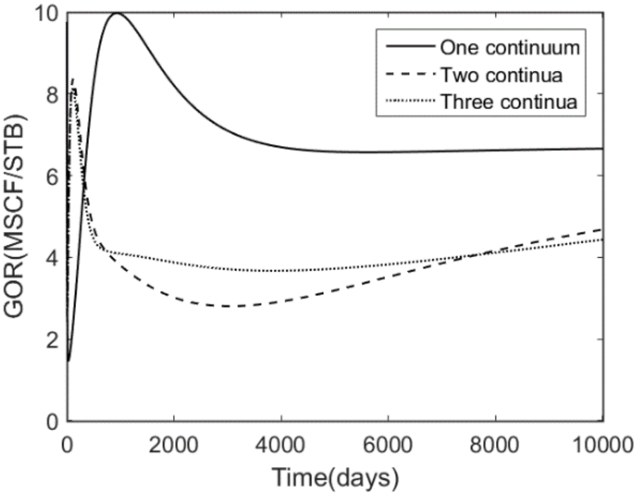

(b)

Figure 3.5 Comparison of reservoir performance using different number of continua in matrix; (a) Pressure, (b) GOR, (c) Cumulative oil production, (d) Cumulative gas production.

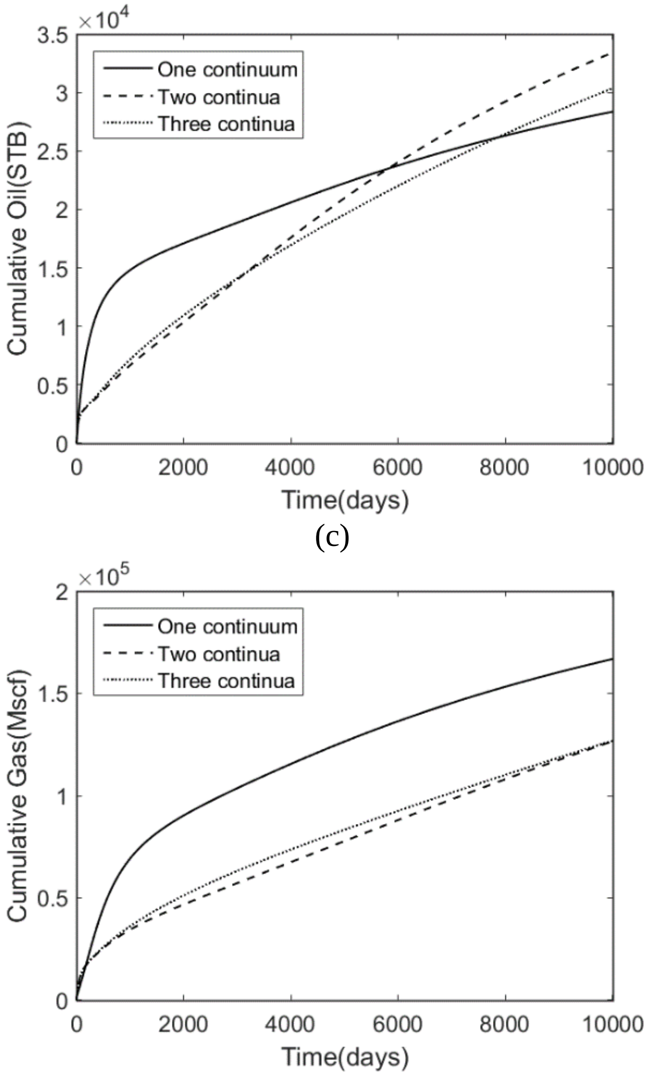

(c)

(d)

Figure 3.5 Continued.

To have a closer analysis, the different continua in shale matrix are further investigated independently. Figure 3.6 illustrates the pressure field and gas saturation field in different continua in all three cases after 7000 days of production. In multiple continua cases, it is not surprising to see that the low permeable continuum has a higher pressure than high permeable continuum. The different pressure in different continuum leads to different gas saturation. More gas come out in higher permeable continuum due to the lower pressure.

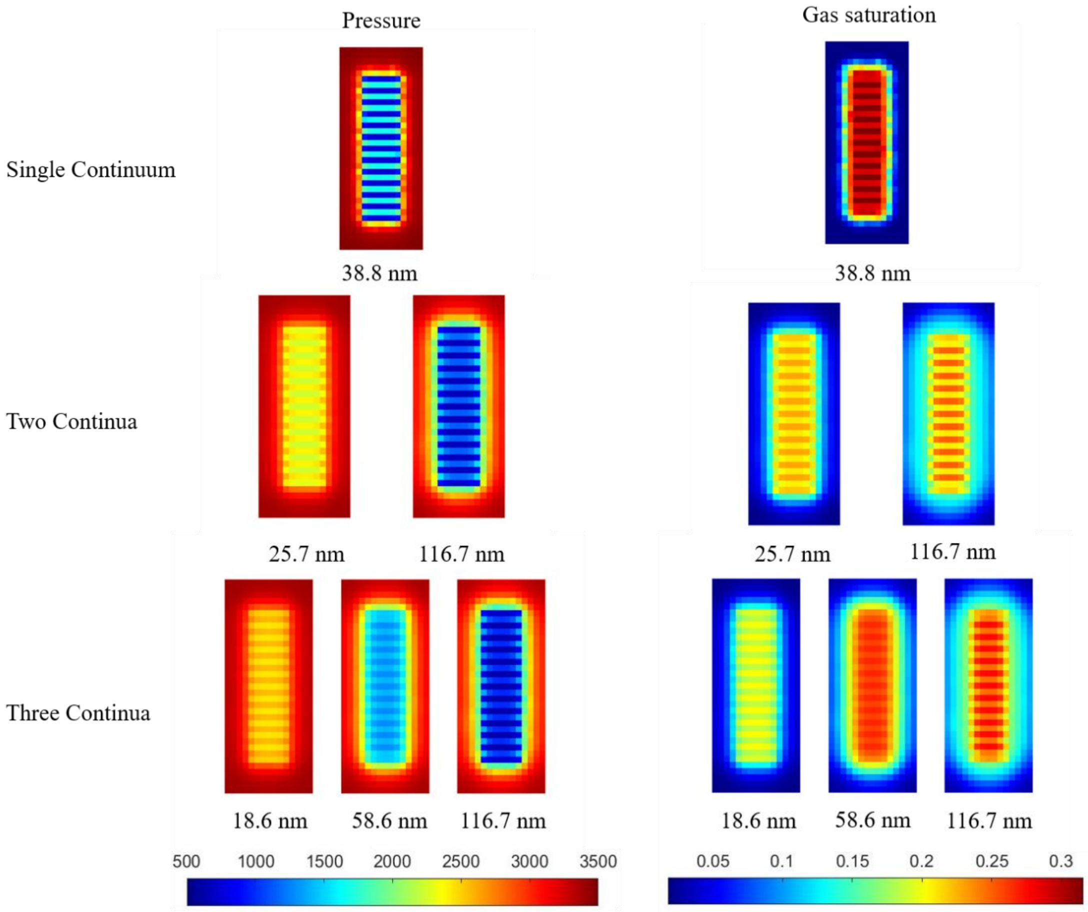

Figure 3.6 Pressure and gas saturation in different kind of continua after 7000 days of production.

Figure 3.7 further presents the pressures and gas saturations in different continua during production. There is always a higher pressure and lower gas saturation in low permeable continua. Apart from gas saturation, different pressure in different continua also leads to different composition. Figure 3.8 presents mole fraction of N_2+C_1 and C_{7+} in different continua. Compared to initial composition, the mole fraction of N_2+C_1 decreases and that of C_{7+} increases in all cases which indicates a heavier residual oil. Moreover, the continua with smaller pore sizes have lighter residual oil.

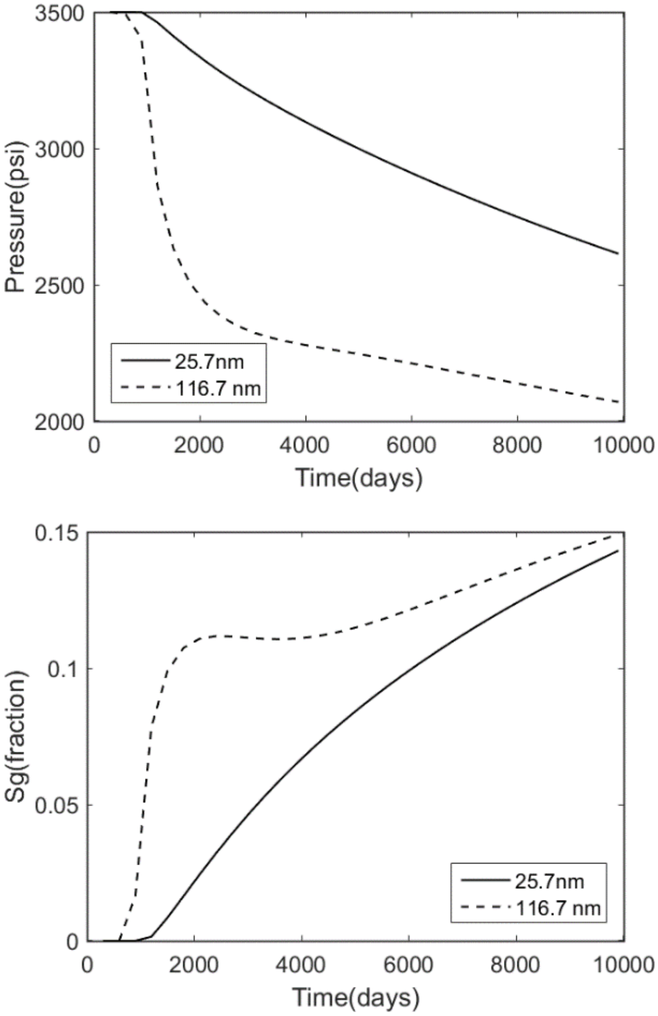

(a)

Figure 3.7 Pressures and gas saturations in different kind of continua during production, (a) two continua case, (b) three continua case.

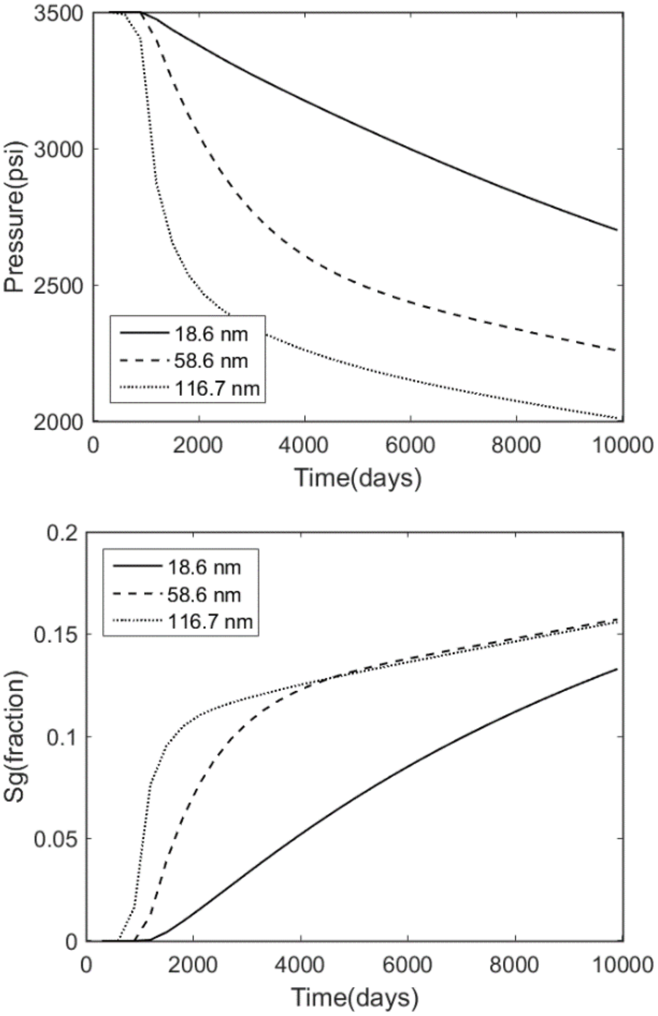

(b)

Figure 3.7 Continued.

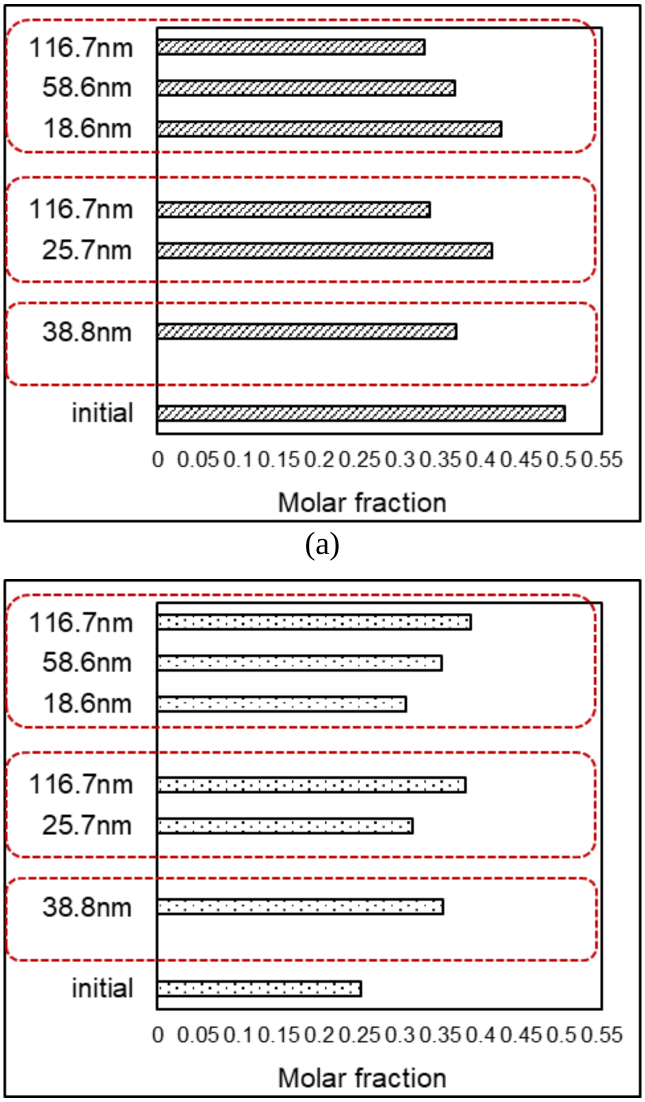

(a)

(b)

Figure 3.8 Mole fraction of N_2+C_1 (a) and C_{7+} (b) in residual oil.

3.2.3 Effect of capillary pressure on phase behavior and production

In Section 3.2.2, we have shown the different reservoir performance when using different number of continua in shale matrix. The difference mainly comes from the different upscaled permeability of matrix. Meanwhile, the physics in different continua should also vary due to the different size of nanopores which may have further effects on production performance. In this section, the phase behavior under confinement is investigated in shale matrix. The degree of confinement in different continua depends on their pore sizes. First, we show that how capillary pressure affects the phase behavior of our fluid model. The fluid composition data have been presented in Table 3.4 and Table 3.5 in Section 3.2.2. The properties of our fluid model under effect of capillary pressure are then evaluated following the procedure introduced in the methodology part. Contact angle is set as 30^o when calculating capillary pressure. Figure 3.9 compares the phase envelop of the fluid model at bulk condition and under effect of capillary pressure. It is observed that the existence of large capillary pressure suppresses both bubble point and dew point and there is a more significant effect on bubble point. At reservoir temperature (165 ^{o}F), the bubble point pressure at bulk condition is 3411 psi and the suppression can be as large as 486 psi when pore diameter is reduced to 18.6 nm.

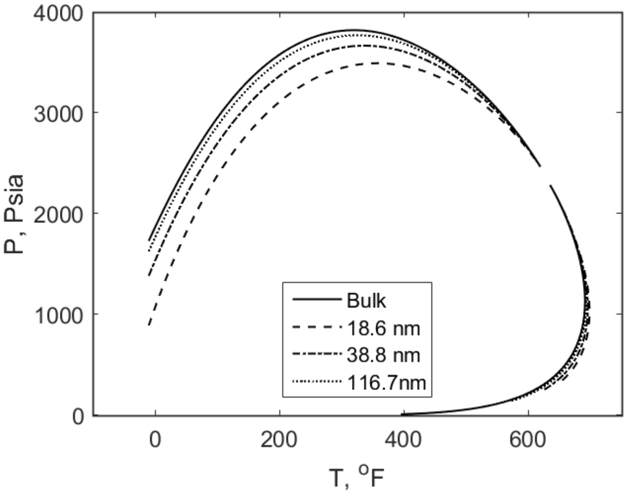

Figure 3.9 Phase envelop of the fluid model under effect of capillary pressure.

Compared to bulk condition, a suppressed bubble point indicates a different composition of oil and gas phases in small pores. Thus, the densities and viscosities of phases under effect of capillary pressure are compared with those at bulk condition in Figure 3.10. A volume shift method (Péneloux et al. 1982) is used to calculate fluid density and Lohrenz-Bray-Clark correlation (Lohrenz et al. 1964) is applied for fluid viscosity. From Figure 3.10, oil density is decreased under the effect of capillary pressure. Gas density, on the other hand, increases under the effect of capillary pressure. Besides, capillary pressure results in a lower oil viscosity and a higher gas viscosity in nanopores. The different fluid properties in different nanopores also suggest that a uniform pore size in shale matrix is not able to describe the complex physics in nanopores and a pore size distribution needs to be introduced. For instance, the bubble point pressures are 2802 psi, 2973 psi, 3132 psi, 3249 psi and 3369 psi in pores with diameter of 18.6 nm, 25.7 nm, 38.8 nm, 58.6 nm, 116.7 nm respectively. Therefore, oil and gas with different properties could coexist in shale matrix even at same pressure and temperature.

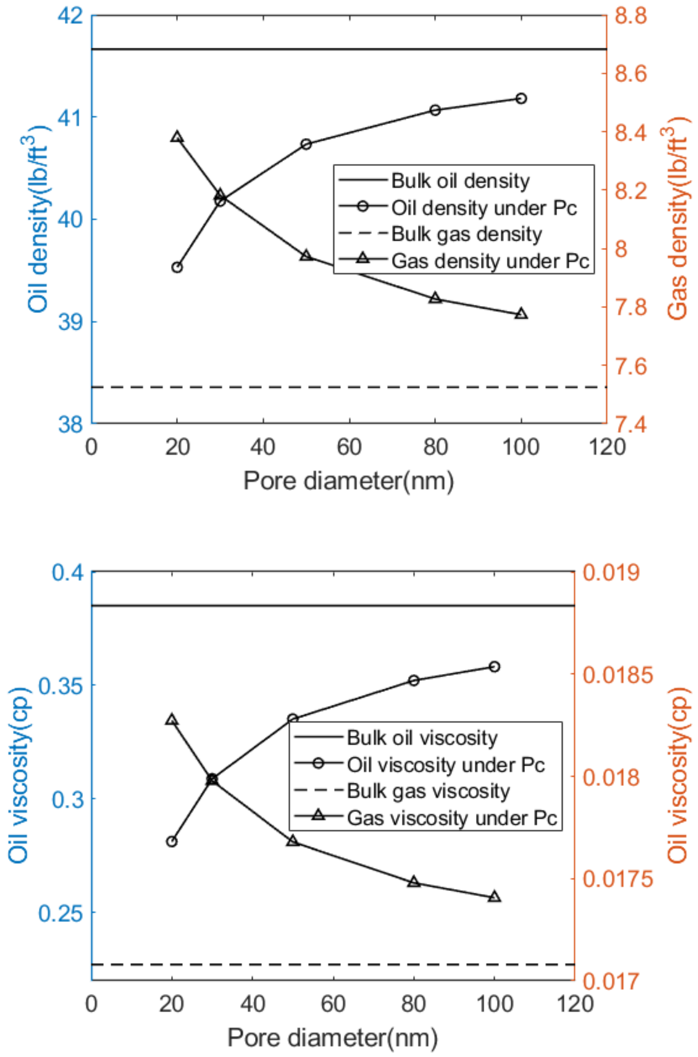

Figure 3.10 Effect of capillary pressure on oil density, gas density, oil viscosity and gas viscosity of the fluid model at 165 ^{o}F and 2000 psia.

The high capillary pressure not only affects phase behavior, but also affects the fluid flow. Thus, capillary pressures in different kind of continua are calculated as a function of gas saturation which is presented in Figure 3.11.

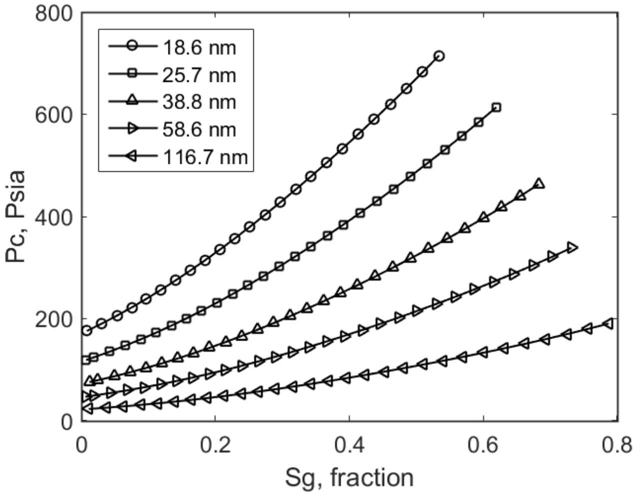

Figure 3.11 Capillary pressure as a function of gas saturation in different kind of continua.

Productions from the same shale reservoir in Section 3.2.2 are then simulated considering effect of capillary pressure in different continua (on both flow and phase behavior). Figure 3.12 compares reservoir performance in different scenarios. It is seen that pressures are all higher when using multiple continua regardless of considering capillary pressure. There is faster pressure decline with capillary pressure in all cases. Oil production rates are all deceased with capillary pressure, especially when single continuum is applied in matrix. The cumulative productions of oil are decreased by 16.9%, 3.6%, 5.9% in one continuum, two continua and three continua cases respectively when capillary pressure is considered. Capillary pressure also decreases gas production rate because of the suppressed bubble point. The cumulative productions of gas are decreased by 10.8%, 8.7%, 8.7% in one continuum, two continua and three continua cases respectively when considering capillary pressure. Besides, GOR in one continuum case is increased under effect of capillary pressure, while GOR in multiple continua cases are slightly decreased. Therefore, we can see that capillary pressure has a more significant effect on reservoir performance when single continuum is applied in matrix, which has also been found in other literatures (Nojabaei et al. 2013, Siripatrachai et al. 2017). However, when multiple continua are applied in matrix, the overall reservoir performance is only slightly affected by capillary pressure.

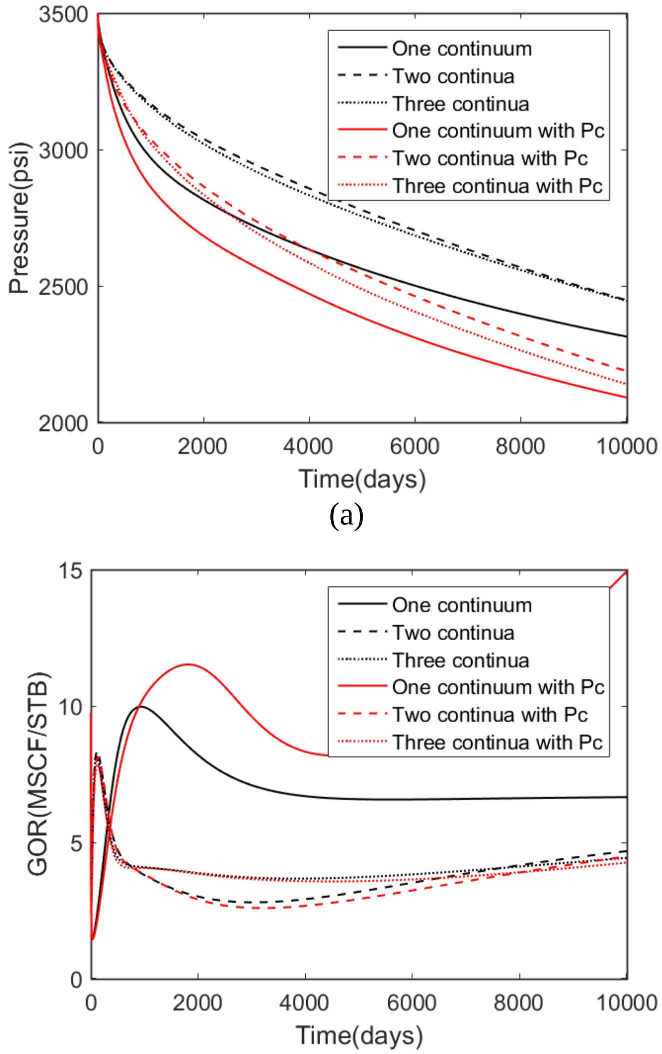

(a)

(b)

Figure 3.12 Effect of capillary pressure on reservoir pressure (a), gas-oil ratio (b), oil production rate (c) and gas production rate (d).

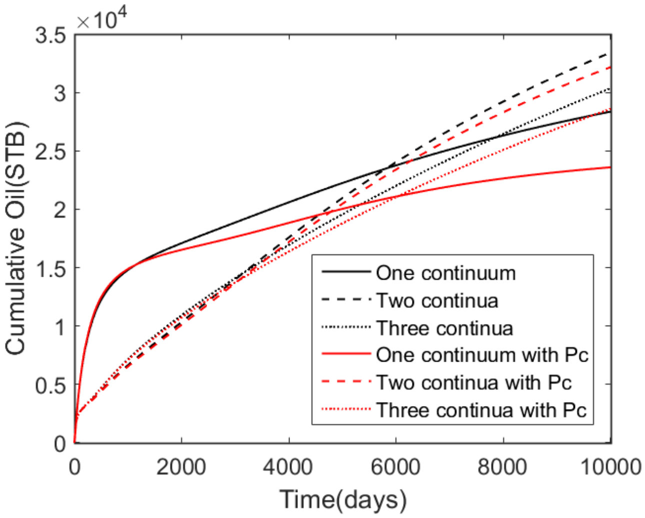

(c)

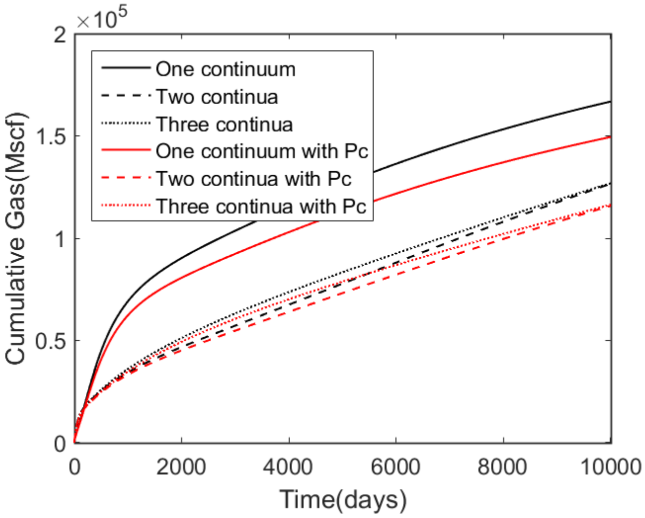

(d)

Figure 3.12 Continued.

Then we further evaluate the performance of every continuum. Figure 3.13 illustrates the oil pressure, capillary pressure and gas saturation in different continua after 7000 days of production. It is also observed that there is a higher pressure and lower gas saturation in low permeable continua. Besides, there exists a very high capillary pressure, especially in the continuum with small pore size. Figure 3.14 compares the pressure and gas saturation in different continua during production with and without capillary pressure. Pressures in every continuum are lower when capillary pressure is considered. Gas saturations are also lower due to the low pressure and suppressed bubble point with capillary pressure. In both two and three continua cases, capillary pressure has a more significant effect in lower permeable continuum where pore size is smaller. Besides, capillary pressure also alters compositions of oil and gas phases.

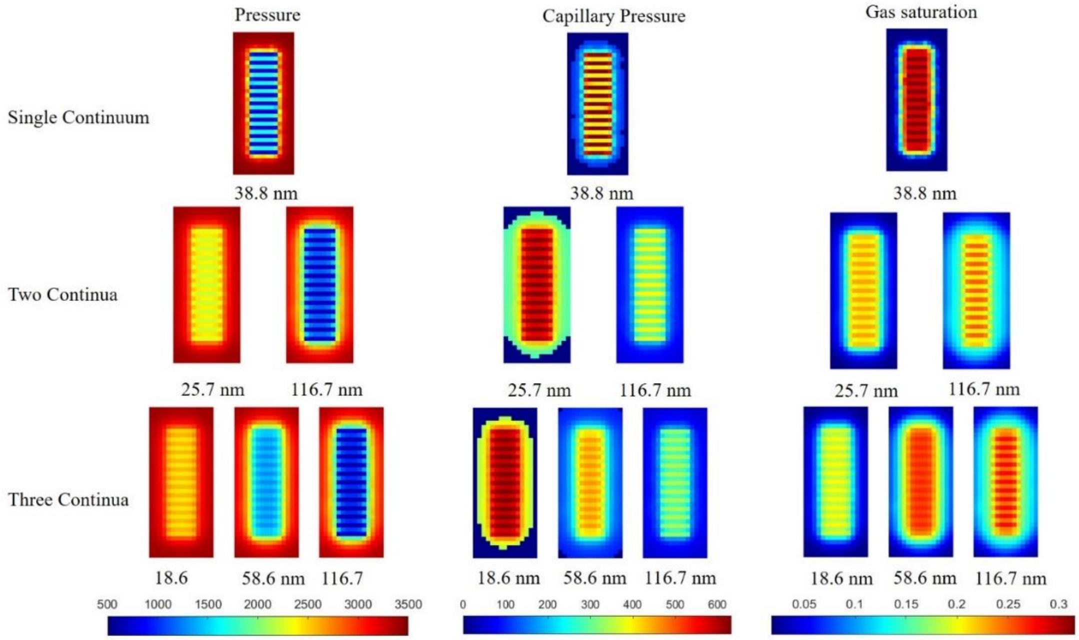

Figure 3.13 Oil pressure, capillary pressure and gas saturation in different kind of continua after 7000 days of production.

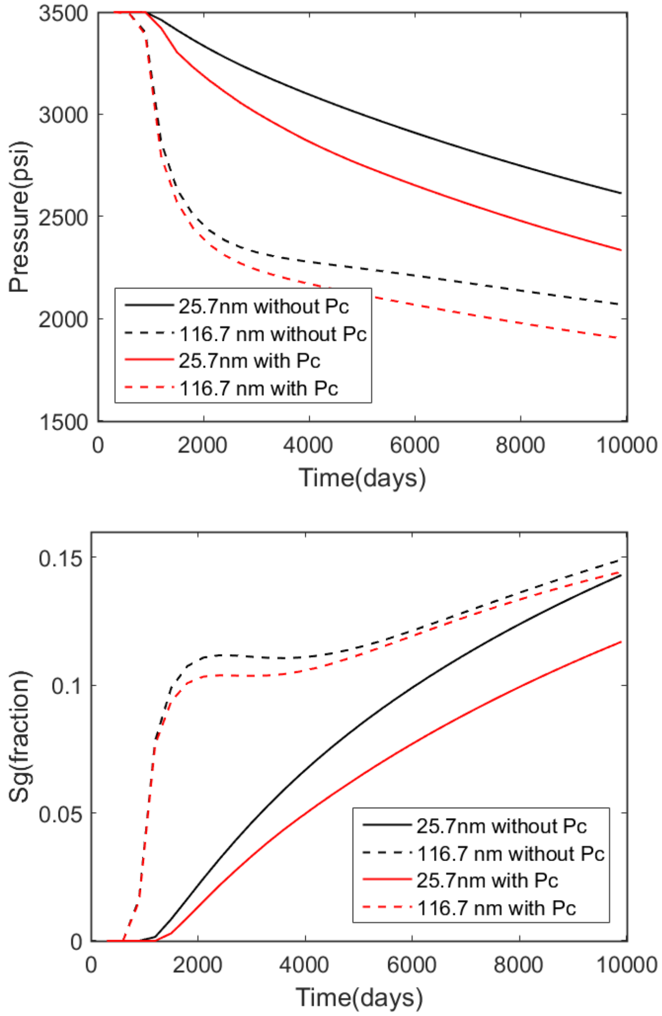

(a)

Figure 3.14 Effect of capillary pressure on different continuum (a) two continua case, (b) three continua case.

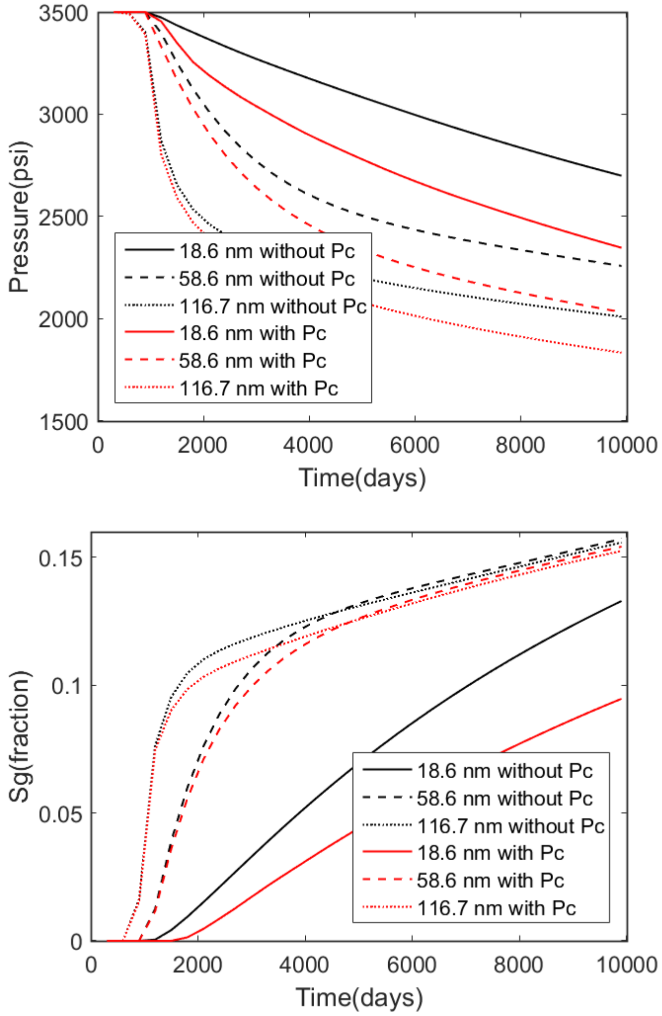

(b)

Figure 3.14 Continued.

Figure 3.15 shows the mole fraction of N_2+C_1 and C_{7+} in residual oil. Compared to initial composition, the residual oil all become heavier with or without capillary pressure. Moreover, residual oil is lighter in the continua with small pore sizes where effect of capillary pressure is significant.

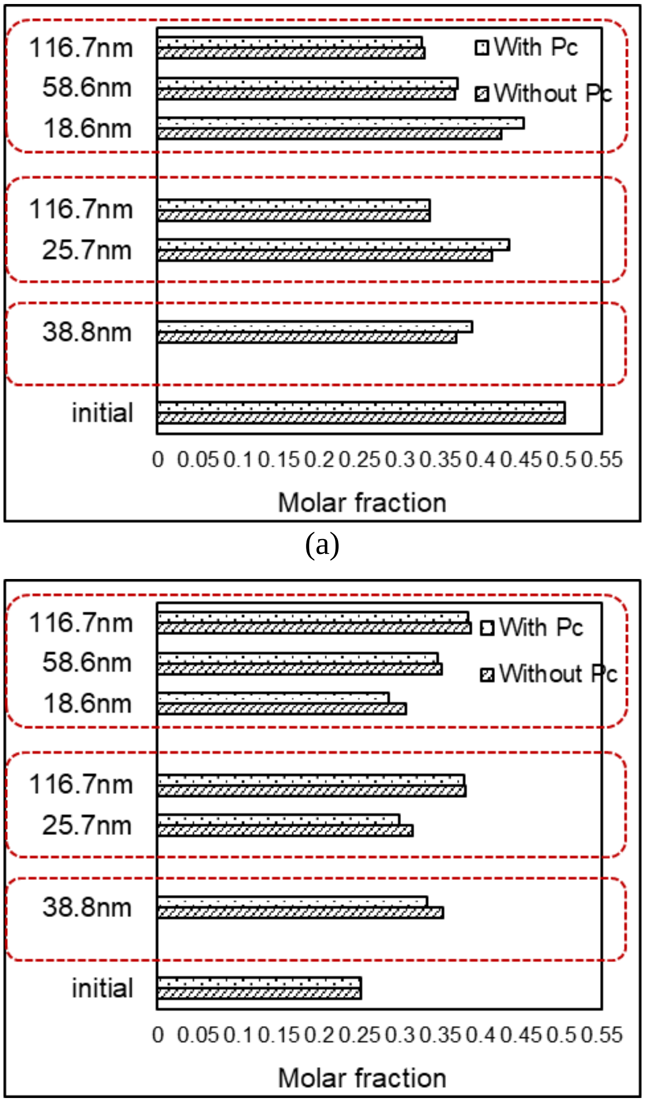

(a)

(b)

Figure 3.15 Effect of capillary pressure on the mole fraction of N_2+C_1 (a) and C_{7+} (b) in residual oil.

3.3 Three-phase flow in mixed-wet shale reservoir

Three-phase flow (oil-gas-water) is often involved when modeling subsurface flow. To characterize the integration between different phases, relative permeability is often required. To obtain three-phase relative permeability, in this study, it is assumed that oil and gas do not dissolve in water and mass transfer is allowed between oil and gas by phase equilibria calculation. Relative permeabilities of water and gas are functions of their own saturations and relative permeabilities of oil are influenced by other saturations. The water-oil system is modeled by direct numerical simulation using a multiphase lattice Boltzmann method. The oil-gas system is evaluated by confined vapor liquid equilibria coupled with Young-Laplace equation and relative permeabilities are obtained from the calculated capillary pressure curve.

3.3.1 Three-phase relative permeability calculation

Relative permeabilities are a function of saturation, fluid and rock properties. Following the widely used method of Stone (Stone 1970; Stone 1973), it is assumed that the water and gas relative permeabilities are only functions of their own saturations. In this way, water-oil and oil-gas system can be evaluated separately. Note that it is assumed oil/gas do not dissolve in water.

For the water-oil system, the two phases are treated as nearly immiscible. Direct numerical simulation has been proven an efficient tool for simulating immiscible two-phase displacement. Among the techniques, lattice Boltzmann (LB) method has been widely used to calculate relative permeability in porous media. In this work, the color-gradient model is applied which can model immiscible two-phase flow accurately and handle a wide range of viscosity contrast and interfacial tension (Huang et al. 2017). In LB method, the fluid dynamics and equilibrium are described by the distribution of pseudo-particles. The evolution equation can be written as (Huang et al. 2017)

$$f_i^k(\boldsymbol{x} + \boldsymbol{c}_i \Delta t, t + \Delta t) = f_i^k(\boldsymbol{x}, t) + \Omega_i^k(\boldsymbol{x}, t) \tag{3.3}$$

where $f_i^k(\boldsymbol{x}, t)$ is the distribution function of pseudoparticles at position $\boldsymbol{x}$ and time t, $\boldsymbol{c}_i$ is lattice velocity, Δt is the time step, Ω_i^k is the collision operator, *k*=*R* or *B* denotes red or blue fluid. For the color gradient LB model, Ω_i^k includes three parts (Tölke et al. 2002)

$$\Omega_i^k = \left(\Omega_i^k\right)^3 \left[\left(\Omega_i^k\right)^1 + \left(\Omega_i^k\right)^2\right] \tag{3.4}$$

where $\left(\Omega_i^k\right)^1$ is the single-phase collision operator that simulates viscous relaxation of stress (d'Humières 2002)

$$(\Omega_i)^1 = -(\boldsymbol{M}^{-1}\boldsymbol{S}\boldsymbol{M})_{ij}[f_j - f_j^{eq}] \tag{3.5}$$

where $\boldsymbol{M}$ is the transformation matrix, $\boldsymbol{S}$ is the diagonal collision matrix, f_j^{eq} is equilibrium distribution function. $\left(\Omega_i^k\right)^2$ is the two-phase collision operator that generates interfacial tension (Liu et al. 2012)

$$(\Omega_i)^2 = \frac{A}{2}|\nabla\rho^N| \left[\omega_i \frac{\left(\boldsymbol{c}_i.\nabla\rho^N\right)^2}{|\nabla\rho^N|^2} - B_i\right] \tag{3.6}$$

where ω_i is the weighting coefficient, B_i are parameters following the work of Liu et al. (2012), *A* is a parameter that controls the value of interfacial tension. ρ^N is the phase field function defined as $\rho^N(\boldsymbol{x}, t) = \frac{\rho_R(\boldsymbol{x},t) - \rho_B(\boldsymbol{x},t)}{\rho_R(\boldsymbol{x},t) + \rho_B(\boldsymbol{x},t)}$. $\left(\Omega_i^k\right)^3$ is the recoloring operator that forces the phase separation (Latva-Kokko and Rothman 2005)

$$(\Omega_i^R)^3(f_i^R) = \frac{\rho_R}{\rho} f_i + \gamma \frac{\rho_R \rho_B}{\rho^2} cos(\varphi_i) f_i^{eq}(\rho, 0) \tag{3.7a}$$

$$(\Omega_i^B)^3(f_i^B) = \frac{\rho_B}{\rho} f_i - \gamma \frac{\rho_R \rho_B}{\rho^2} cos(\varphi_i) f_i^{eq}(\rho, 0) \tag{3.7b}$$

where f_i is total distribution function, ρ is total density, ρ_R and ρ_B are the density of red fluid and blue fluid respectively, φ_i is the angle between the phase field function gradient

$\nabla\rho^N$ and $\boldsymbol{c}_i$, γ is a free parameter controls interface thickness. To implement wettability in color-gradient model, it is assumed that the rock surface is a mixture of two fluids with a certain value of ρ^N. For instance, if the contact angle of red fluid is θ, ρ^N on rock surface will be set as $cos\theta$. To construct water-oil relative permeability, the porous media is first fully saturated with oil and water saturation is increased step by step. Simulation in each step is conducted until a quasi-stationary state is reached.

For the oil-gas system in shale reservoir, the relative permeability largely depends on the phase behavior. When limited data provided, predictive modeling from first principle models is a proper choice to obtain relative permeability (Stimpson and Barrufet 2017) and a commonly used one is to infer from capillary pressure correlation. In a confined pore space, capillary pressure can be calculated by Young-Laplace equation

$$P_{cap} = 2\sigma cos\theta / r \tag{3.8}$$

where r is pore radius and θ is the oil-gas contact angle. Interfacial tension σ can be calculated by (Weinaug and Katz 1943)

$$\sigma^{1/E} = \sum_{i=1}^{N_c} \chi_i (x_i / V_m^l - y_i / V_m^v) \tag{3.9}$$

where χ_i is the Parachor of component i, V_m^l and V_m^v are the molar volume of liquid and vapor phase respectively, and the exponent parameter E is given as (Danesh et al. 1991)

$$E = 3.583 + 0.16(1/V_m^l - 1/V_m^v) \tag{3.10}$$

For an isothermal system, capillary pressure changes with reservoir pressure and there is a certain oil saturation at every pressure. Thus, capillary pressure can also be described as a function of oil saturation. With the capillary pressure curve, relative permeability of oil and gas can be obtained using (Nakornthap and Evans 1986)

$$k_{ro} = (S_o^*)^2 \frac{\int_0^{S_o^*} \frac{1}{P_c^2} dS_o^*}{\int_0^1 \frac{1}{P_c^2} dS_o^*} \tag{3.11a}$$

$$k_{rg} = (1 - S_o^*)^2 \frac{\int_{S_o^*}^1 \frac{1}{P_c^2} dS_o^*}{\int_0^1 \frac{1}{P_c^2} dS_o^*} \tag{3.11b}$$

where

$$S_o^* = \frac{S_o - S_{o,r}}{1 - S_{o,r}} \tag{3.12}$$

In this work, the capillary pressure curve is fitted using a rational polynomial to calculate the integral in Eqn. (3.11a) and Eqn. (3.11b).

3.3.2 Simulation setup for mixed-wet shale reservoir

To study three-phase flow in shale oil reservoir, a reservoir model shown in Figure 3.16 is built with parameters presented in Table 3.6. The shale matrix is divided into organic matrix and inorganic matrix with different petrophysical properties. The organic matrix has a smaller pore size, lower permeability and lower initial water saturation due to its hydrophobic condition. By subdividing the shale matrix, TOC can be modeled explicitly. To quantify the content of organic matter, a volumetric TOC is defined by (Olorode et al. 2017)

$$\mathrm{TOC} = \frac{V_o}{V} \tag{3.13}$$

where V_o is volume of organic matrix and V is the total volume of matrix. TOC is set as 0.4 at the beginning and effect of TOC will be evaluated in the following section. Besides, the complex hydraulic fractures shown in Figure 3.16 are modeled using EDFM. The fluid model used in this study is a volatile oil from north America (Huang et al. 2019a). The compositional parameters of the fluid are provided in Table 3.7.

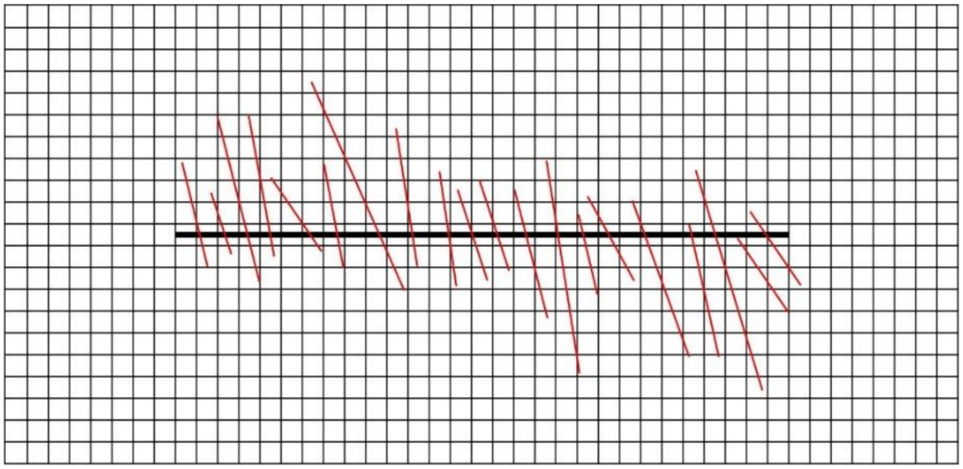

Figure 3.16 Fractured shale oil reservoir model; bold black line represents the horizontal well and red lines represent hydraulic fractures.

Table 3.6 Basic parameters for shale oil reservoir

Reservoir conditions	
Initial Pressure (Psia)	3500
Initial Temperature (^oF)	160
Porosity (fraction)	0.08
Grid number	45 x 21 x 1
Grid size (ft)	50 x 50 x 50
Organic Matrix	
Pore diameter (nm)	15
Permeability (nd)	10
Water saturation (fraction)	0.25
Inorganic matrix	
Pore diameter (nm)	100
Permeability (nd)	100
Water saturation (fraction)	0.35
Hydraulic Fracture	
Fracture number	20
Fracture conductivity (mD.ft)	300

Table 3.7 Compositional parameters of fluid model

Component	Mole fraction	Critical Pressure (psia)	Critical temperature (^oF)	Acentric factor	Molecular weight	Parachor
CO_2	0.001924	1069.87	87.89	0.22450	44.01	78
N_2+C_1	0.503155	661.78	-120.18	0.00899	16.26	76.18
C_2-C_3	0.139236	661.59	148.59	0.12527	35.83	130.62
C_4-C_6	0.104671	492.99	371.24	0.23813	69.32	227.18
C_{7+}	0.251013	277.38	811.47	0.76355	198.88	785.52

The three-phase relative permeability in shale matrix is obtained by using a two-step method. In the first step, the oil-water relative permeability is obtained by digital rock analysis. Figure 3.17 presents the digital rock sample of a shale rock. The oil-water relative permeability is then calculated by directly simulating two-phase flow on the digital rock. Different contact angles are used in simulation to investigate effect of wettability. Figure 3.18 shows the calculated relative permeabilities under conditions of oil-wet (water-oil contact angle 135^o) and water-wet (water-oil contact angle 54^o). Secondly, the oil-gas relative permeability is obtained by using first principle models. Provided with the compositional parameters in Table 3.7, interfacial tension between oil and gas can be calculated using Eqn. (3.9) as well as the capillary pressures at different saturations (Figure 3.19a). With capillary pressure curves, oil-gas relative permeabilities are obtained by calculating the integral in Eqn. (3.11a) and Eqn. (3.11b). The gas phase is treated as the nonwetting phase in both organic and inorganic matrix and the relative permeabilities in Figure 3.19b is under the condition when the oil-gas contact angle is 60^o. With water-oil and oil-gas relative permeabilities, the three-phase relative permeabilities in matrix are constructed using the method of Stone II (Stone 1973). Besides, water-oil and oil-gas relative permeabilities in fractures are assumed to be a linear function for simplicity.

Provided with the reservoir model, fluid model and calculated relative permeabilities, compositional simulation of this shale oil reservoir then can be conducted. Production is constrained by a constant bottomhole pressure of 500 Psi and no flow boundary condition is applied in the outer boundary.

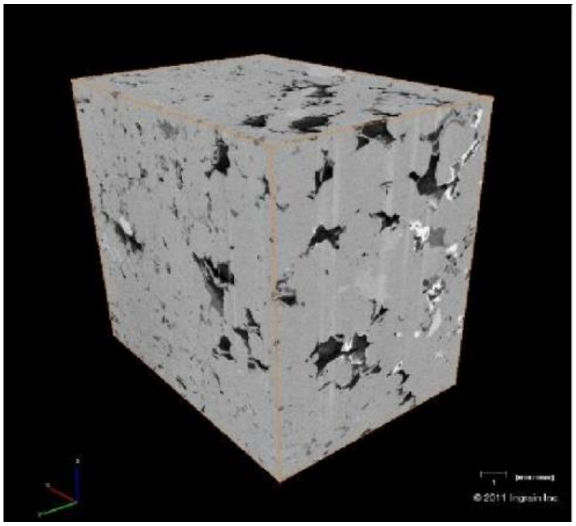

Figure 3.17 Digital rock sample for the calculation of water-oil relative permeability; gray part is solid grain, black part is pore (reprinted from Cantisano et al. 2013).

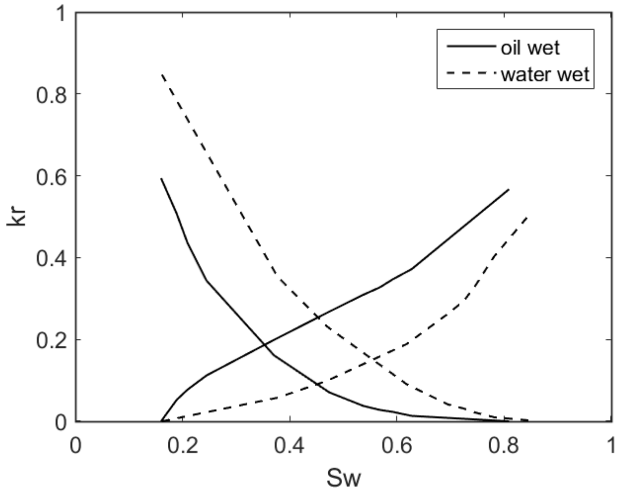

Figure 3.18 Oil-water relative permeabilities from lattice Boltzmann simulations under different conditions of wettability (data obtained from Cantisano et al. 2013).

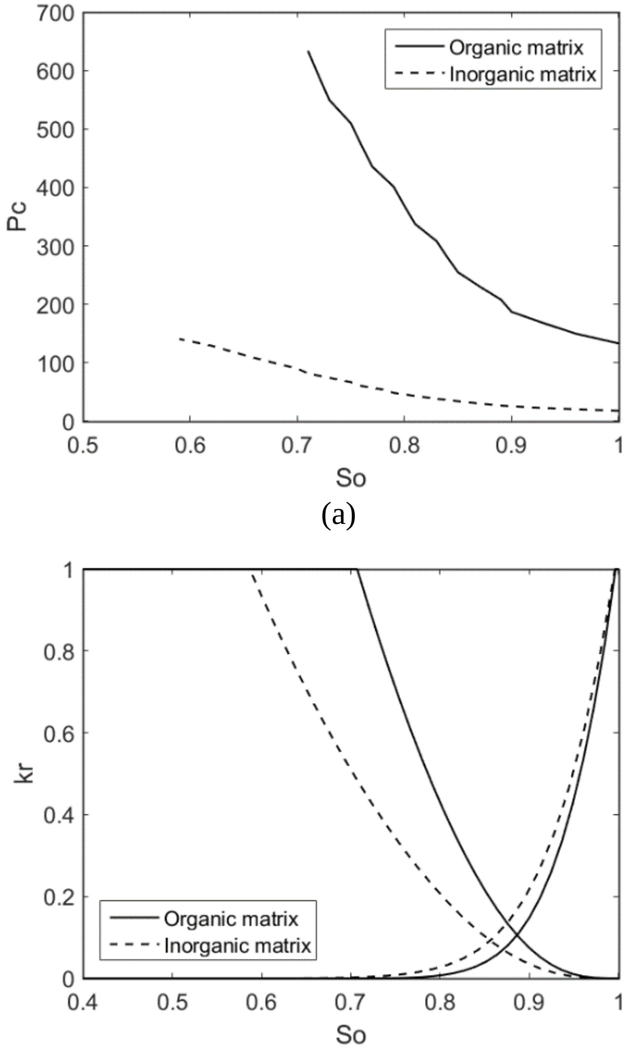

(a)

(b)

Figure 3.19 Calculated oil-gas capillary pressures (a) and relative permeabilities (b) when oil-gas contact angle is 60^0.

3.3.3 Results and Discussions

In this section, the three-phase flow in mixed-wet shale oil reservoir is modeled using the proposed approach. Phase saturations in organic and inorganic matrix are obtained and production rates of water, oil and gas are particularly analyzed. By changing the volume fraction of organic matrix, effects of TOC are evaluated explicitly. Simulations results under mixed-wet condition are then compared to those where a uniform wettability is applied. Finally, the effects of contact angles on production are investigated including different water-oil contact angles and oil-gas contact angles, in both organic and inorganic matrix.

In this study, the mixed-wet condition is considered explicitly in shale matrix. Specifically, the organic matrix is set as oil-wet while the inorganic matrix is water-wet. The water-oil relative permeabilities in organic and inorganic matrix are using the ones presented in Figure 3.18. Besides, the oil-gas relative permeabilities in Figure 3.19b are applied. Figure 3.20 presents the pressure distributions, water saturations, oil saturations and gas saturations in both organic and inorganic matrix, after ten years of production. It is seen that most of the pressure-decline and production of fluids happens in the stimulated area. Though having similar pressure distributions, the inorganic matrix and organic matrix have very different saturations of fluids. A higher oil/gas saturation and lower water saturation are observed in organic matrix. Since the organic matrix is not directly connected to fractures, fluids must go through the inorganic matrix before reaching fractures. Besides, because the organic matrix is oil-wet while inorganic matrix is water-wet, the oil mobility is lower and water mobility is higher in organic matrix. Thus, the rich hydrocarbon in organic matrix is more difficult to be produced.

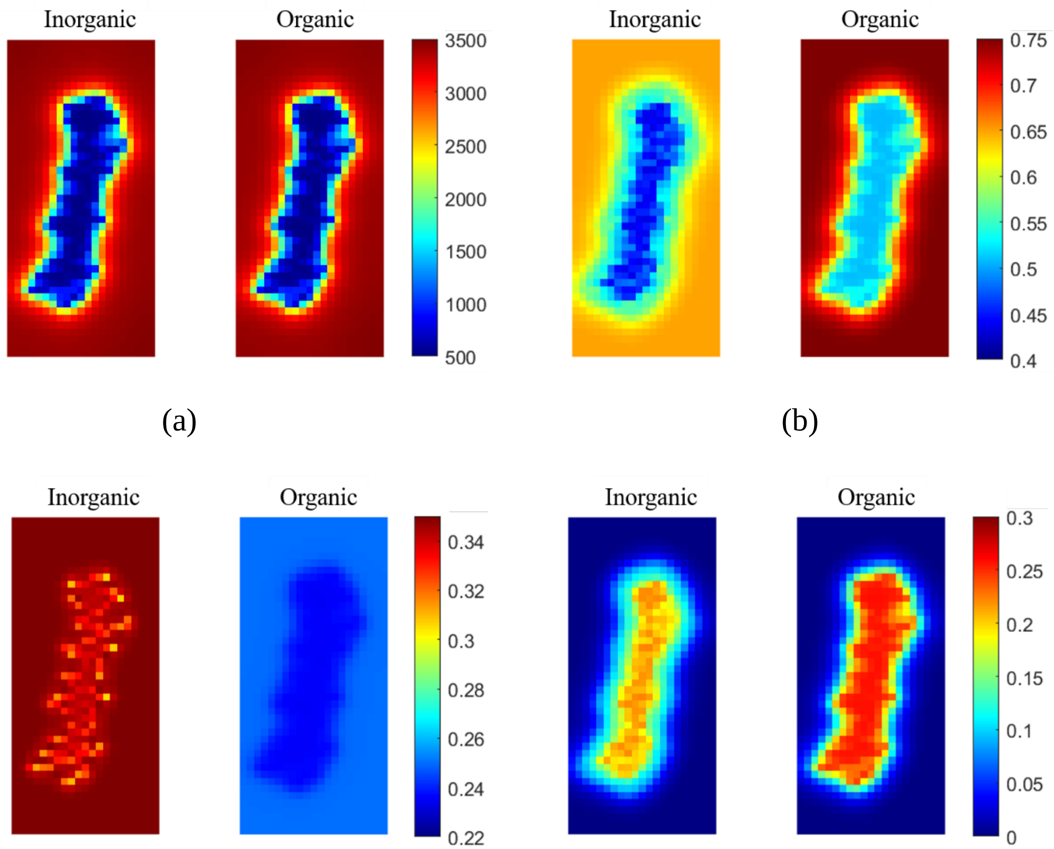

(a) (b)

(c) (d)

Figure 3.20 Pressure distribution (a), oil saturation (b), water saturation (c) and gas saturation (d) in mixed-wet shale reservoir after 10 years of production.

The overall production performance of this mixed-wet shale oil reservoir is shown in Figure 3.21. To analyze the effect of organic matter, three different TOC in shale matrix are compared. From Figure 3.21, it is seen that a higher reservoir pressure can be maintained when TOC is high due to the relative lower permeability of organic matrix. The oil and water production from shale reservoir with high TOC are lower at early stage of production, but higher at later period. Gas production in high-TOC case, on the other hand, is lower at the beginning but close to those in low-TOC cases in the end. From the comparisons, we find that effects of TOC can be classified into two stages: (1) at early stage, the low permeability of organic matrix leads to lower production rates but (2) at later stage, the rich hydrocarbon in organic matrix starts to take effect and increases the overall production.

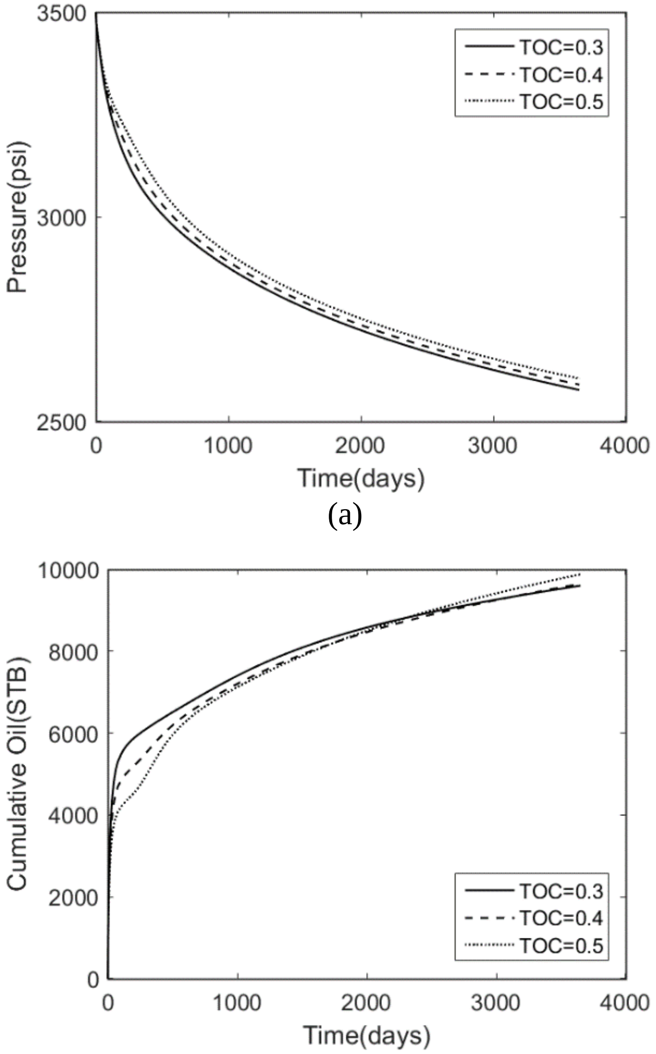

(a)

(b)

Figure 3.21 Effect of TOC on the production performance of shale reservoir; (a) pressure, (b) oil production, (c) gas production (d) water production.

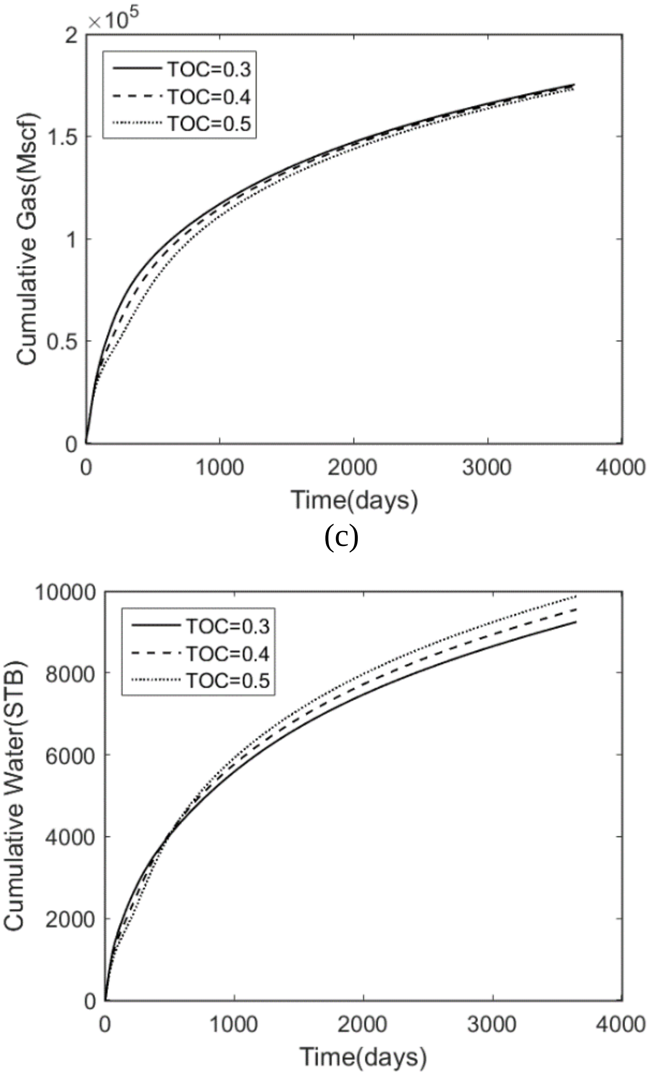

(c)

(d)

Figure 3.21 Continued.

To further illustrate the effects of mixed wettability, another two cases with uniform wettability are conducted for comparison. In the water-wet case, all matrix is set as water-wet and the water-oil relative permeability with contact angle of 54^o is applied in both organic and inorganic matrix. In the oil-wet case, matrix is oil wet and the water-oil relative permeability with contact angle of 135^o is applied. Figure 3.22 compares the reservoir pressure, oil, gas and water production under different conditions of wettability. Compared to mixed-wet case, the oil production is much lower, gas production is higher and water production is much higher when the shale matrix is uniformly oil wet. The significant difference comes from the fact that the inorganic matrix is water wet in mixed-wet case but is oil wet in oil-wet case. Based on the relative permeabilities in Figure 3.18, the oil mobility is largely suppressed, and water mobility is much increased when inorganic matrix is oil wet. Thus, the lower oil production and higher water production have been observed. When the shale matrix is uniformly water wet, both oil and water production is lower and gas production is slightly higher compared to mixed-wet case. It is seen that the difference between mixed-wet case and water-wet case is not very significant. The organic matrix becomes water wet in water-wet case which means that water mobility should be lower and oil mobility should be higher in organic matrix. However, because organic matrix is embedded in inorganic matrix, all the fluids in organic matrix must go through inorganic matrix first before being produced through fractures. Therefore, the relative permeability in inorganic matrix is the dominant factor that controls the production rates of fluids. Since the wettability of inorganic matrix is the same in mixed-wet case and water-wet case, the production performances are thus closer.

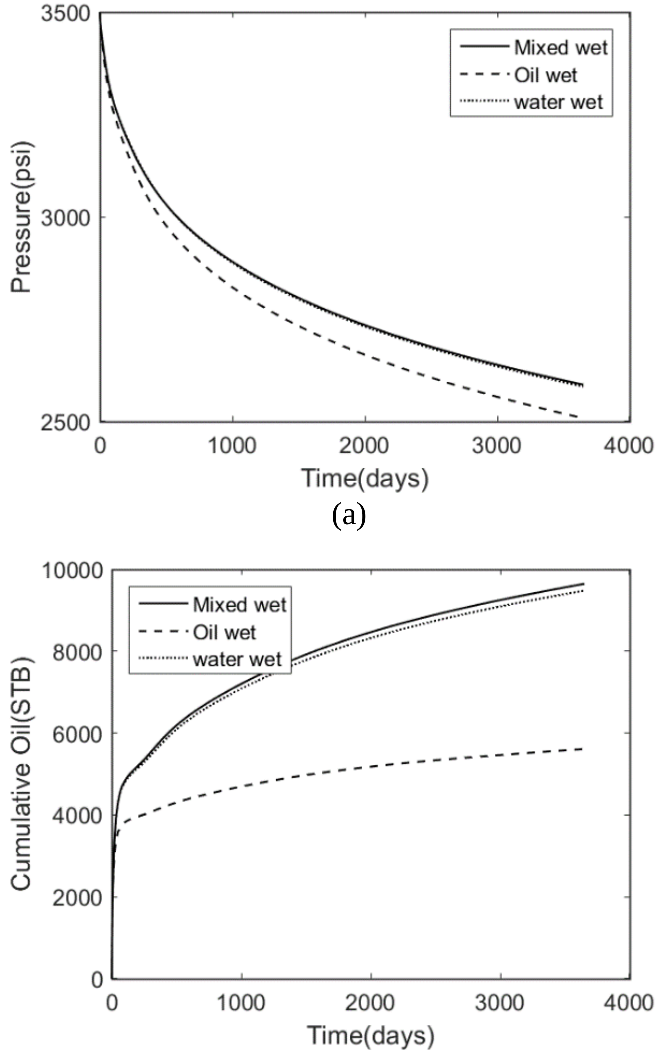

(a)

(b)

Figure 3.22 Comparison of production performance between mixed-wet shale reservoir and uniform-wet shale reservoir; (a) pressure, (b) oil production, (c) gas production (d) water production.

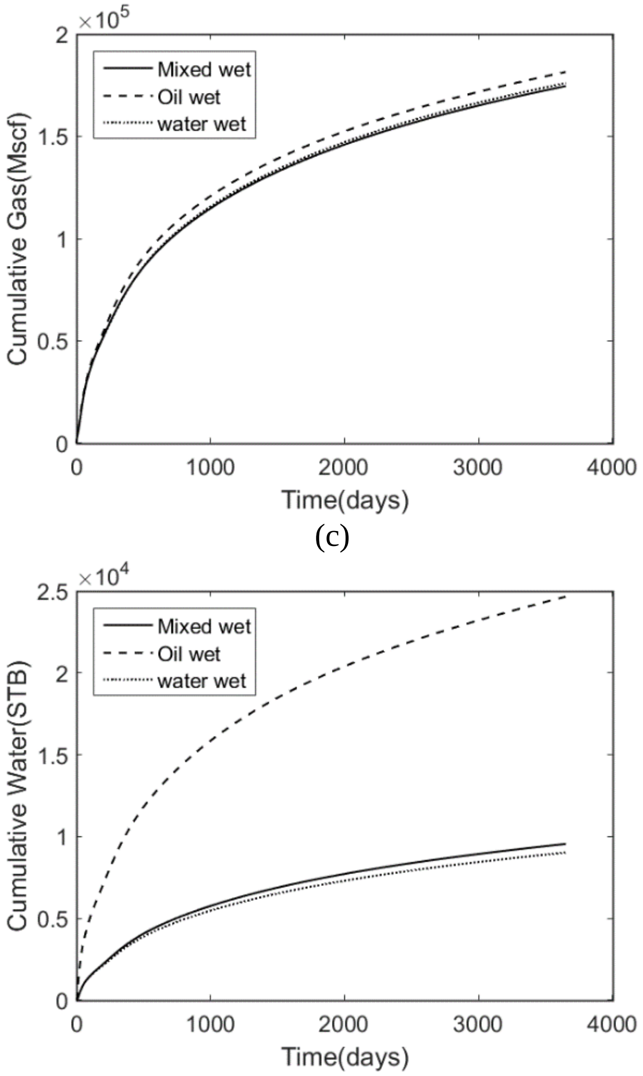

(c)

(d)

Figure 3.22 Continued.

It has been found that the relative permeability depends on contact angles (Huang et al. 2017; Pan et al. 2004). Thus, it is essential to evaluate the three-phase flow in shale reservoir using different contact angles. In this part, the effects of water-oil contact angle (WOCA) are investigated. Three cases are conducted: (1) WOCA in organic matrix is 135^o and in inorganic matrix is 54^o, (2) WOCA in organic matrix is 160^o and in inorganic matrix is 54°, (3) WOCA in organic matrix is 135° and in inorganic matrix is 30°. Figure 3.23 presents the water-oil relative permeabilities under different contact angles, in both organic and inorganic matrix. It is seen that the water permeability is lower and oil permeability is higher in inorganic matrix, when the contact angle is decreased to 30°. On the other hand, the water permeability is increased, and oil permeability is decreased in organic matrix, when contact angle is set to 160°. The altered relative permeabilities due to contact angles in turn affect the production performance of the shale reservoir. Figure 3.24 compares the pressure decline and production rates under different conditions of contact angles. No obvious differences are observed in terms of pressure decline and gas production. By comparing case (1) and case (2), the change of contact angle in organic matrix slightly affects oil and water productions. Results from case (1) and case (3) indicate that the contact angle in inorganic matrix has a significant effect on oil and water production: a stronger water-wet inorganic matrix leads to a higher oil production and lower water production. This finding further confirms the conclusion that the relative permeability (wettability) in inorganic matrix controls the overall water and oil productions.

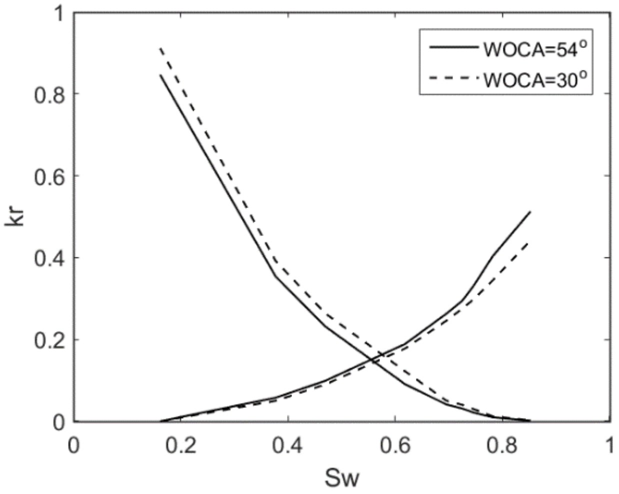

(a)

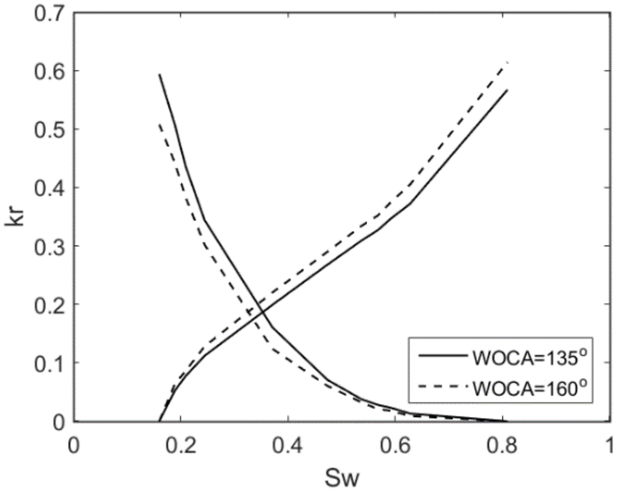

(b)

Figure 3.23 Effect of contact angle on water-oil relative permeability in inorganic matrix (a) and organic matrix (b).

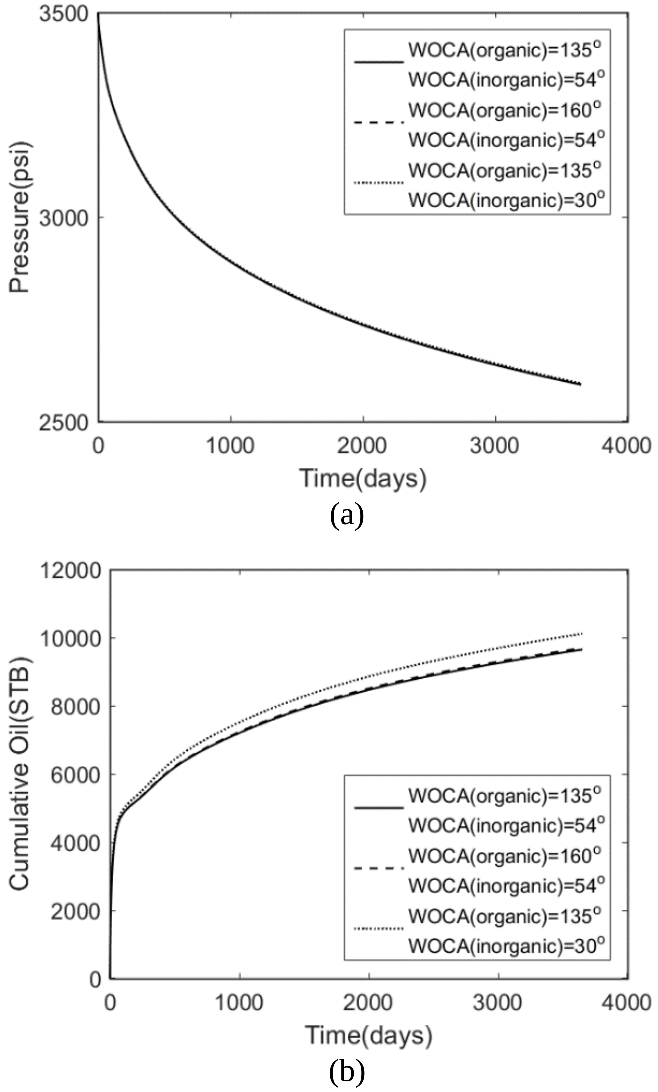

Figure 3.24 Effect of water-oil contact angle on the production performance of shale reservoir; (a) pressure, (b) oil production, (c) gas production (d) water production.

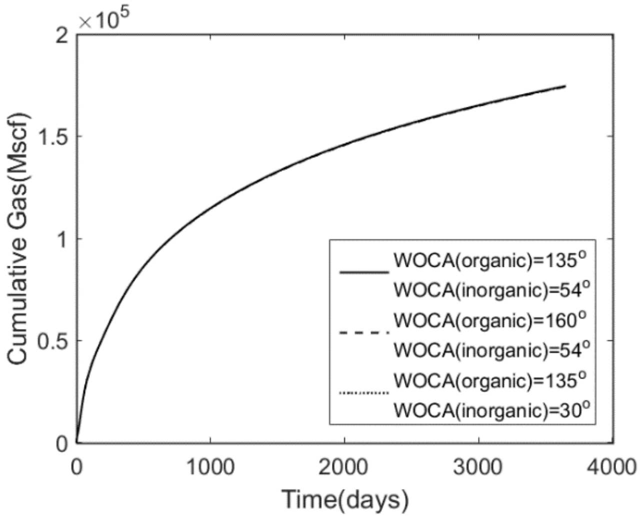

(c)

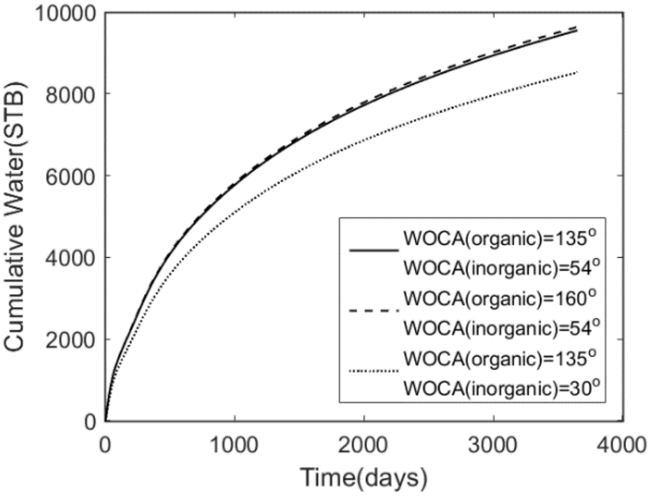

(d)

Figure 3.24 Continued.

Oil-gas relative permeability is also affected by oil-gas contact angle (OGCA). With the same fluid compositions and pore size, contact angle controls oil-gas capillary pressure, from which oil-gas relative permeability is extracted. Figure 3.25 shows the oil-gas relative permeabilities with different OGCA in both organic and inorganic matrix. In inorganic matrix where pore size is relatively larger, the oil permeability is more sensitive to contact angle. Oil permeability is increased when contact angle is decreased to 30^o. Gas permeability is lower at high oil saturation and higher at lower oil saturation when contact angle is turned to 30^o. On the other hand, gas permeability is more sensitive to contact angle in organic matrix where pore size is smaller. Gas permeability is increased, and oil permeability is slightly decreased when contact angle becomes 30^o. The production performance with different OGCA are compared in Figure 3.26. The water production rate when contact angle is 30^o is slightly higher than that when contact angle is 60^o. Oil production rate is significantly increased when contact angle is 30^o due to the increased oil permeability in the inorganic matrix. Though gas permeability is higher in organic matrix, the gas production rate has negligible changes from different contact angles. Again, it is found that the oil-gas contact angle in inorganic matrix has much larger effects than that in organic matrix.

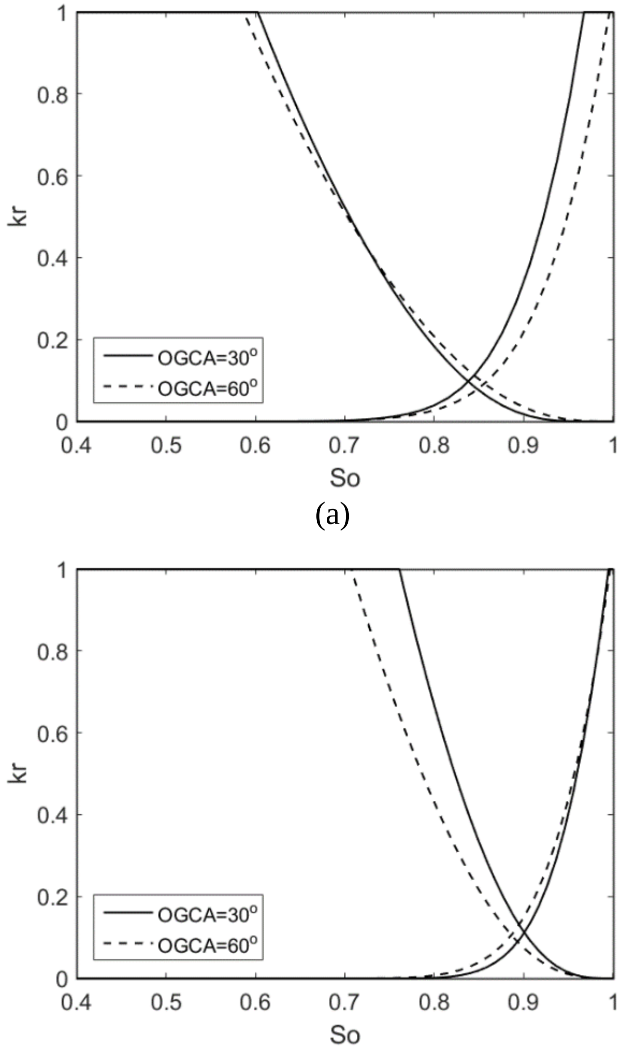

(a)

(b)

Figure 3.25 Effect of oil-gas contact angle on the relative permeabilities in inorganic matrix (a) and organic matrix (b).

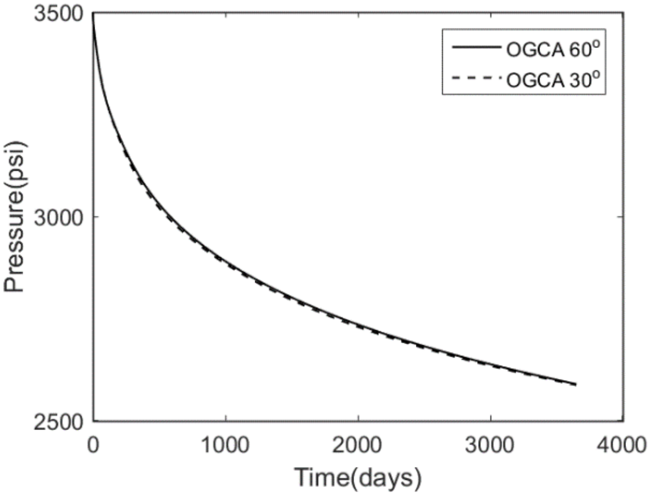

(a)

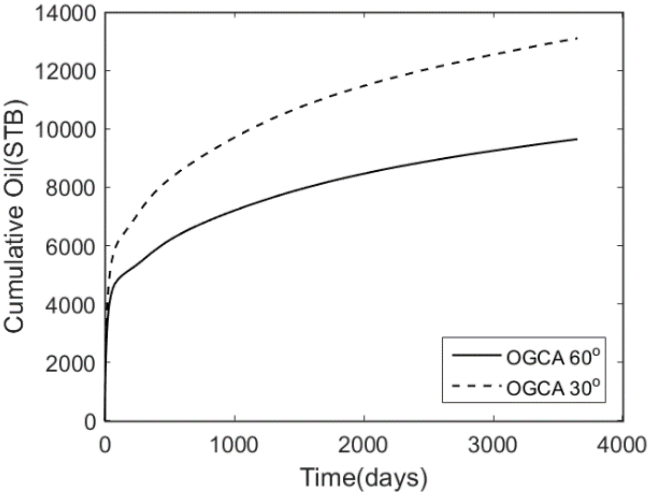

(b)

Figure 3.26 Effect of oil-gas contact angle on the production performance of shale reservoir; (a) pressure, (b) oil production, (c) gas production (d) water production.

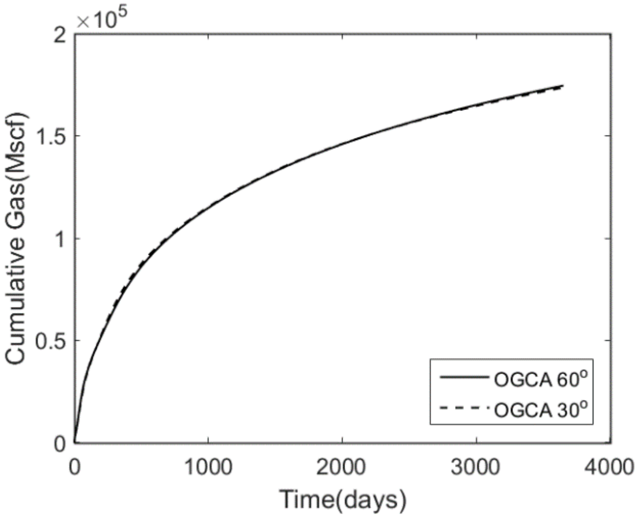

(c)

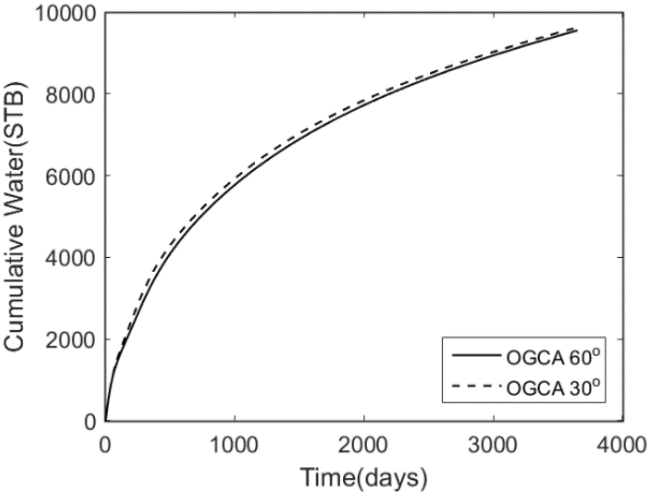

(d)

Figure 3.26 Continued.

3.4 Conclusions and Discussions

In this Chapter, effect of pore size distribution in shale reservoir simulation is first studied. A fractured shale oil reservoir with distribution of nanopores is modeled by using a multi-porosity model coupled with EDFM approach. Based on experimental data of pore size from BET analysis, the shale matrix is subdivided into different number of continua for analysis. Hydraulic and natural fractures with different angles and intersections are modeled explicitly using EDFM. Compositional simulations show that there is a lower pressure decline, lower oil and gas production when using multiple continua in matrix. The continua with smaller pore sizes have a higher pressure and lower gas saturation. The existence of continua with small pore sizes reduces oil and gas recovery due to their low permeability. By analyzing compositions, it is found that the residual oil is becoming heavier during production in every type of continua. The continua with smaller pore sizes have lighter residual oil compared to that in other continua. Besides, capillary pressure leads to different fluid properties in different nanopores such as bubble point, density and viscosity. Oil production are decreased when capillary pressure is considered, especially in one continuum case. Gas production are also suppressed with capillary pressure in all cases. GOR is increased with capillary pressure in one continuum case, while slightly decreased in multiple continua cases. Residual oil is lighter in the continua with small pore sizes where effect of capillary pressure is significant.

As a conclusion, different rates of pressure decline in different size of nanopores are modeled by applying multiple continua in shale matrix, which cannot be captured when one continuum is used. Besides, it is shown that oil and gas with different properties could coexist in shale matrix even at same pressure and temperature when effects of confinement are considered. The application of multiple continua allows different kinds of fluids at the same location and captures the complex flow properties and phase behaviors in different kind of nanopores. Meanwhile, we are also aware that the application of multiple continua in shale matrix inevitably introduces more uncertainties and complexities into simulation and increases the computational time. However, this work aims to provide some understanding on the effects of distribution of nanopores in shale reservoir simulation.

Besides, compositional simulation of three-phase flow is conducted considering mixed wettability in shale oil reservoir. By using the multi-porosity model, mixed-wettability is modeled explicitly by dividing the shale matrix into organic and inorganic matrix, which are oil-wet and water-wet respectively. To construct relative permeability for three-phase flow, the Stone II method is applied that assumes the permeabilities of water and gas are only functions of their own saturations. Water-oil relative permeability is obtained by performing immiscible two-phase flow directly on digital rock sample using a multiphase lattice Boltzmann method. Oil-gas relative permeability is extracted from oil-gas capillary pressure curve, which is calculated from fluid compositions and phase behavior. Different three-phase relative permeabilities are applied to organic and inorganic matrix according to the condition of wettability.

From the simulation results, we obtain the following findings and conclusions: Firstly, the rich hydrocarbon in organic matrix is hard to be produced due to its low permeability, low oil mobility and poor connection to hydraulic fractures. Secondly, a higher TOC in shale matrix leads to lower production rates at early stage due to the low permeability of organic matter, but oil/gas production is increased at later stage when the rich hydrocarbon in organic matrix starts to take effect. Thirdly, comparisons with uniform-wet cases indicate that productions from mixed-wet and water-wet reservoir are close. On the other hand, oil production is much lower and water production is higher from oil-wet reservoir. Last, different water-oil contact angles and oil-gas contact angles are evaluated, in both organic and inorganic matrix. It is found that the contact angles in inorganic matrix have more significant effects on production. Due to the dispersed nature of organic matter, the fluids in organic matrix must go through inorganic matrix first before reaching fractures. Therefore, the production rates largely depend on the mass transfer between inorganic matrix and fractures. The relative permeability in inorganic matrix, which is affected by wettability, is thus a dominant factor that controls the overall production in shale reservoir.

CHAPTER IV

SIMULATION OF GAS INJECTION INTO SHALE RESERVOIR [*]

4.1 Introduction

With the techniques of horizontal well and hydraulic fracturing (Yuan et al. 2015), productions of natural gas from shale reservoirs have been a huge success in US (Weijermars, 2014). Shale gas has been a main contributor in energizing US and the world economically (Middleton et al. 2017; Arora and Cai 2014). Meanwhile, the fast decline of production rates during shale gas development brought attentions to enhance gas recovery (EGR) such as refracturing (Shah et al. 2017; Eshkalak et al. 2014), infill well drilling (Urban et al. 2016) or gas injection (Du and Nojabaei 2019; Godec et al. 2014). Among these techniques, carbon dioxide (CO_2) injection into depleted shale reservoirs is a promising one because it provides great potential for both CO_2 storage and enhanced gas recovery. It has been estimated that 71 Tcm of shale gas could be recovered by EGR globally, which could facilitate the potential storage of 281 Gt of CO_2 (Godec et al. 2014). One important mechanism of CO_2 injection is that the adsorption capacity of shale for CO_2 is larger than that for methane (CH_4) (Yuan et al. 2014; Pan et al. 2018) and some studies show that CO_2 is preferentially adsorbed over CH_4 with a ratio up to 5:1 (Nuttall et al.

---

[*] Part of data reported in this chapter is reprinted with permission from “Evaluation of CO_2 injection into shale gas reservoirs considering dispersed distribution of kerogen” by by Huang, J., Jin, T., Barrufet, M., Killough, J., 2020. Applied Energy, Volume 260, 114285, Copyright 2020 by Elsevier.

2005). Thus, CO_2 could replace the adsorbed methane via competitive adsorption when CO_2 is introduced in shale (Nuttall 2010).

Potential and sensitivity tests for CO_2 injection and storage have been conducted in Barnett shale (Yu et al. 2014), Marcellus shale (Godec et al. 2013), Devonian shale (Schepers et al. 2009), New Albany Shale (Liu et al. 2013), and Bakken shale (Jin et al. 2017). Experimental investigation showed that the geochemical interactions between CO_2 and shale (Pan et al. 2018), methane adsorption and diffusion (Yuan et al. 2014), and swelling of organic rich shale (Chen et al. 2015; Lu et al. 2016) have impacts on both EGR and CO_2 storage. Effects of hydraulic fractures (Kalantari-Dahaghi 2010), multi-component transport and stress change (Kim et al. 2017) during CO_2 injection have also been conducted. Among the work on CO_2 injection into shale gas reservoir, two kinds of production modes were often investigated, namely CO_2 flooding and CO_2 huff-n-puff. In CO_2 flooding, one well is used for injection while the other well produces all the time. In CO_2 huff-n-puff, a well goes through three stages: injection, soaking and production (Yu et al. 2014). Yu et al. (2014) conducted a sensitivity test on CO_2 injection for EGR in Barnett shale reservoir. They found that CO_2 flooding can improve the gas recovery while CO_2 huff-n-puff cannot. Eshkalak et al. (2014) compared CO_2 flooding and CO_2 huff-n-puff and they concluded that CO_2 huff n puff is not a viable option for EGR. Kim et al. (2017) evaluated CO_2 injection using different shale models considering multi-component adsorption and stress-dependent permeability. It is observed that both CO_2 flooding and CO_2 huff-n-puff can increase the gas recovery, though huff-n-puff is not preferred compared to the flooding case. Also, more CO_2 can be stored underground when using

CO_2 flooding. Apart from production modes, the presence of nanopores in shale matrix makes the fluid behavior deviate from the predictions of conventional theory and different mechanisms need to be considered such as multi-component diffusion, adsorption and slippage etc. Adsorption was found to have a nontrivial effect on shale gas production and CO_2 storage (Kang et al. 2011; Fathi and Akkutlu 2014). Kang et al. (2011) conducted experiment on the detail CO_2 storage in organic-rich shale and found that 97% of gas is stored in adsorbed state inside the organic pores. Fathi and Akkutlu (2014) studied effects of competitive transport and adsorption in organic pores during CO_2 injection. They concluded that the mechanisms of counter diffusion and competitive adsorption are the key factor for improving the gas recovery. From the studies above, several findings can be summarized. First, the CO_2 flooding works better than CO_2 huff-n-puff in terms of EGR and CO_2 storage. The complex flow mechanisms in shale matrix need to be carefully investigated when evaluating CO_2 injection into shale gas reservoirs.

It is well known that shale is highly heterogeneous with extremely small pore size, high total organic carbon (TOC), low permeability and porosity in shale matrix as well as the complex hydraulic/natural fractures (Ambrose et al. 2012; Luo et al. 2013). Meanwhile, the shale matrix contains different minerals that can be classified into organic matter (kerogen) and inorganic matter including clay, quartz, pyrite etc. (Olorode et al. 2017; Yan et al. 2018b). The nanopores are widely developed in kerogen during geological ages (Jin et al. 2019) and most of the pores are micro pores (< 2nm) and mesopores (2-50 nm) (Kang et al. 2011). Those organic matter have large capacity for both compressed gas and adsorbed gas (Ambrose et al. 2012; Yan et al. 2018b). Due to the nanoscale pores, effects of molecule-solid interaction become significant and gas slippage and diffusion cannot be ignored (Civan et al. 2011). On the other hand, the inorganic matter has larger pores compared to organic matter, and thus the permeability of inorganic matter is much larger than that of organic matter (Wasaki and Akkutlu 2015). Besides, the affinity of inorganic matter for gas is weak and can be ignored (Yan et al. 2018b). Since the mechanisms of gas flow and storage in organic and inorganic matter are quite different, it is essential to divide the shale matrix based on minerals as well as to apply different physics to different kind of matrix (Yan et al. 2018b; Huang et al. 2020). Moreover, from scanning-electron-microscope (SEM) images of shale samples, the kerogen appears to be a dispersed phase inside the inorganic matrix at the micron scale (Ambrose et al. 2012; Huang et al. 2020). At the scale of reservoir simulation, which is in meters or even larger, the connectivity of kerogen should be poor (Olorode et al. 2017). Thus, the organic matrix can be regarded as discontinuous in reservoir simulation while the inorganic matrix is continuous (Olorode et al. 2017; Akkutlu and Fathi 2012). Then the mass transfer between organic and inorganic matrix will be in series which has also been found in a gas injection experiment (Kang et al. 2011).

The complexity in modelling shale reservoir also comes from the complex fracture systems. Fathi and Akkutlu (2014) argued that the mass transfer in shale gas reservoir has three stages: 1) convective/dispersive flow of gas in fractures, 2) diffusive/dispersive gas transport in fractures and macropores of shale matrix, 3) multicomponent sorption in the micropores of shale matrix. These different mechanisms of gas flow and storage take place at different characteristic time and length of scales (Fathi and Akkutlu 2014) and make it more difficult to model shale gas reservoir. To simulate the interactions between fractures and shale matrix, several approaches have been developed including the dual porosity model (Warren and Root 1963), discrete fracture model (Karimi-Fard et al. 2004, Sandve et al. 2012), and embedded discrete fracture model (EDFM) (Li and Lee 2008, Chai et al. 2018a). The dual porosity mode treats fractures as a continuous porosity type (Warren and Root 1963). The discrete fracture model describes the fractures explicitly using unstructured grids to conform fracture geometries (Karimi-Fard et al. 2004). The EDFM approach calculates the transmissibility between fractures and matrix analytically without the need of unstructured mesh and local grid refinement (Chai et al. 2018a). Besides, the EDFM can be coupled with multi-porosity model in a straightforward manner that enables us to consider multiple continua in shale matrix as well as the complex fracture systems (Huang et al. 2019a).

Previous studies have shown how organic and inorganic matter in shale matrix affect the shale gas production during depletion (Olorode et al. 2017; Yan et al. 2018b). However, the effects of dispersed distribution of kerogen during injection of CO_2 have not been thoroughly investigated, especially when there exists a complex network of fractures. Since competitive adsorption between CO_2 and methane only happens in the organic matter, the dispersed nature of kerogen will affect the efficiency of CO_2 injection. In view of this unaddressed question, this work aims to evaluate CO_2 injection into shale gas reservoirs considering multiple continua and physics in matrix. Specifically, we divide the shale matrix into organic and inorganic matrix using the multi-porosity model. The facture systems are modelled explicitly using EDFM. Then three continua in the shale gas reservoir are modeled: organic matrix, inorganic matrix and fractures. To consider the dispersed distribution of kerogen, the organic matrix is embedded inside inorganic matrix and discontinuous. The inorganic matrix is continuous and directly connected to fractures. Each continuum has its own petrophysical properties including pore size, permeability, porosity etc. Different physics are applied in different continua: viscous flow in fractures and inorganic matrix, gas slippage and diffusive transport in organic and inorganic matrix, adsorption/desorption in organic matrix. By using multiple continua in matrix, the effects of TOC can be investigated explicitly. The rest of the paper is organized as follows: first the multi-porosity model and EDFM approach are briefly introduced and the multi-physics compositional simulation is formulated. Then the CO_2 injection into a fractured shale gas reservoir is evaluated using the proposed methods, followed by discussions and conclusions.

4.2 Simulation setup

To evaluate the effects of CO_2 injection, a shale reservoir model in Figure 4.1 was built. As shown, two parallel horizontal wells were drilled, either for production or injection. Each horizonal well has 13 stages of hydraulic fractures shown as red lines. The blue lines in Figure 4.1 represent the natural fractures that are directly connected to hydraulic fractures. Different from the dual porosity model, all the fractures are described explicitly. The basic parameters of this fractured reservoir are summarized in Table 4.1. Gas production is constrained by using a constant bottomhole pressure (500 psi). No flow boundary condition is applied in the outer boundary of the reservoir. Then the shale matrix is further divided into organic and inorganic matrix. Note that the organic matrix is discontinuous between simulation grids. The petrophysical properties of organic and inorganic matrix are listed in Table 4.2. The organic matrix has a smaller pore size and lower permeability compared to the inorganic matrix. Since the organic matrix is hydrophobic and inorganic matrix is hydrophilic (Yan et al. 2018b), the initial water saturation in organic matrix is 0 while that in inorganic matrix is 0.1 (immobile). A low water saturation in shale matrix is to reduce the uncertainty for this study. The initial water saturation in fracture is 0.1. Water-gas relative permeability in fractures are assumed to be a linear function. Different physics are considered in different continua. Viscous flow is considered in fractures and shale matrix. In both organic and inorganic matrix, gas slippage and molecular diffusion are implemented. Adsorption/desorption are only considered in organic matrix. The Langmuir adsorption constants of CO_2 and methane in Table 4.3 are used in this study, which are obtained from core experiments in Barnett shale (Vermylen 2011).

Then the effects of dispersed distribution of kerogen during CO_2 injection are studied under different scenarios. Both CO_2 flooding and CO_2 huff-n-puff are investigated. In CO_2 flooding cases, after 4 years of primary production, CO_2 is injected into one well with a constant injection rate of 20 Mscf/day while the other well continues producing. After 4 years of injection, the injecting well is shut in and the other well produces till 30 years. In CO_2 huff-n-puff cases, after 4 years of primary production, CO_2 is injected into both wells for 3 months with a constant injection rate of 20 Mscf/day, followed by one month of soaking. Then both wells are turned into production for 8 months. This cycle repeats for 8 times. Then both wells continue producing till 30 years of production.

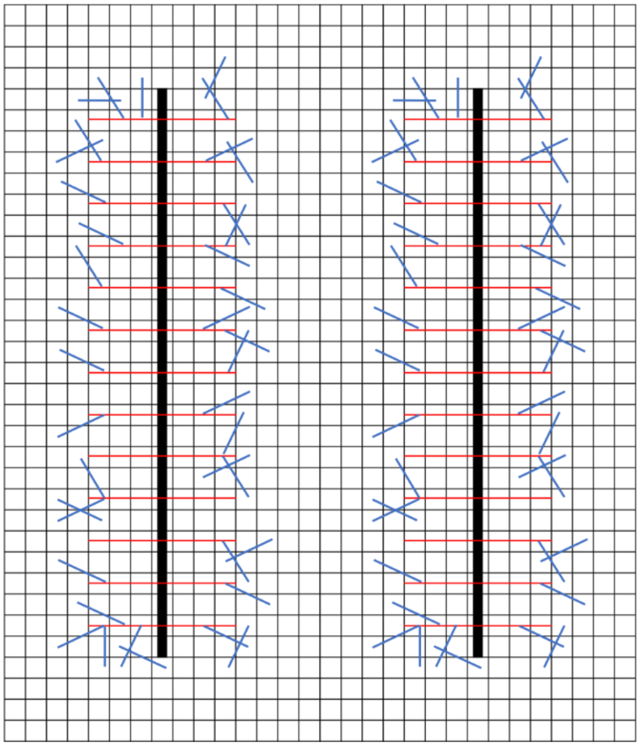

Figure 4.1 Fractured shale reservoir model (well-bold black lines; hydraulic fractures-red lines; natural fractures-blue lines).

Table 4.1 Basic parameters for the fractured shale reservoir

Reservoir conditions	
Initial Pressure (Psia)	2500
Initial Temperature (^{o}F)	106
Producer BHP (Psia)	500
Matrix	
Grid number	35 x 30 x 1
Grid size (ft)	50 x 50 x 50
Porosity (fraction)	0.03
Hydraulic Fracture	
Fracture number	26
Fracture half length (ft)	175
Fracture conductivity (mD.ft)	30
Natural Fracture	
Fracture number	80
Fracture conductivity (mD.ft)	0.3

Table 4.2 Petrophysical properties of organic and inorganic matrix

Organic matrix	
Pore diameter (nm)	6
Permeability (nd)	2.8
Water saturation (fraction)	0
Inorganic matrix	
Pore diameter (nm)	50
Permeability (nd)	28
Water saturation (fraction)	0.1

Table 4.3 The Langmuir constants of CO_2 and methane for Barnett shale

CO_2	
PL (psi)	1596
VL (scf/ton)	183.6
Methane	
PL (psi)	1254
VL (scf/ton)	39.2

4.3 Results and discussions

4.3.1 CO_2 injection with dispersed distribution of kerogen

In this section, we compare the CO_2 injection into shale gas reservoir with and without considering dispersed distribution of kerogen. There is only one continuum existing in shale matrix when kerogen is considered implicitly, thus we name these cases as 1C. The cases considering kerogen explicitly have two continua in matrix (organic and inorganic) which are named as 2C. In the cases of Section 4.3.1, the TOC is set as 0.4, binary diffusion coefficient is $1e^{-4}$ and injecting rate is 20 Mscf/day in each well. Figure 4.2 presents the average reservoir pressures with time in different cases. Compared to depletion, CO_2 huff-n-puff can slightly help maintain the reservoir pressure. The reservoir pressures are much higher when doing CO_2 flooding because only one well is producing after CO_2 injection. Besides, the reservoir pressures are higher when considering kerogen explicitly due to the existence of low permeable organic matrix.

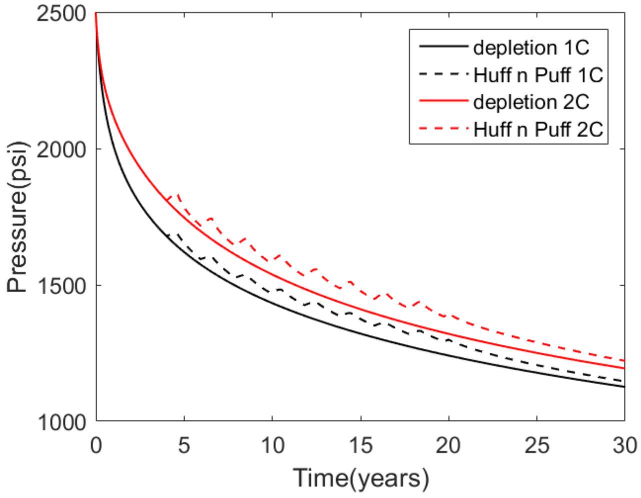

(a)

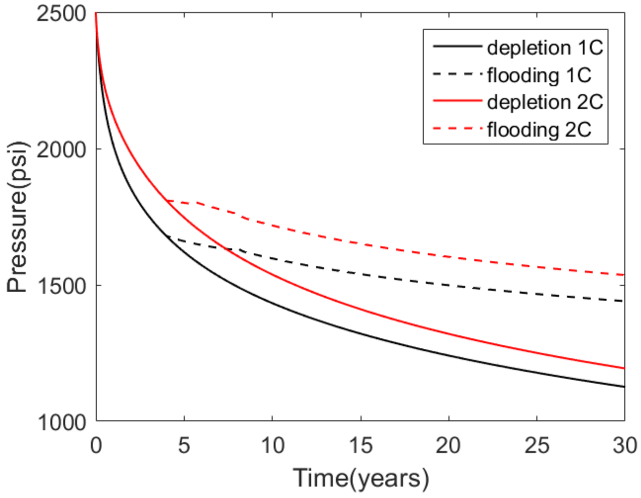

(b)

Figure 4.2 Comparison of average reservoir pressures with and without explicitly considering dispersed distribution of kerogen; (a) CO_2 huff-n-puff, (b) CO_2 flooding.

Figure 4.3 shows the cumulative production of methane and performance of CO_2 storage in different cases. It is observed that CO_2 huff-n-puff can slightly improve the gas recovery if kerogen is described implicitly. The gas recovery is decreased after CO_2 huff-n-puff if kerogen is considered explicitly. On the other hand, CO_2 flooding decreases the gas recovery significantly in both cases. Figure 4.3 also presents the injected, produced and stored CO_2 using CO_2 huff-n-puff and CO_2 flooding. It is seen that 44.6% of injected CO_2 is reproduced when kerogen is considered implicitly while 92% of injected CO_2 is reproduced when kerogen is considered explicitly, using CO_2 huff-n-puff. In CO_2 flooding cases, no CO_2 breakthrough occurs, and all the injected CO_2 can be stored in the reservoir. Though all injected CO_2 can be stored underground, the injectivity of CO_2 is low in CO_2 flooding case compared to that in CO_2 huff-n-puff cases. From Figure 4.3, $1.6e^5$ lb-mol of CO_2 can be injected into the reservoir using huff-n-puff, while only $7.6e^4$ lb-mole or $4.2e^4$ lb-mol of CO_2 can be injected into reservoir if kerogen is considered implicitly or explicitly. The reason of the low injectivity in CO_2 flooding case is that the injected CO_2 cannot move far from the fractures due to the ultralow permeability of shale matrix. Then the accumulation of CO_2 around the injecting well increases bottom-hole pressure which can quickly exceed the operation limit of injecting pressure (8000 psi in this work). Thus, a constant injecting rate cannot be maintained, and the cumulative injection of CO_2 is lower during CO_2 flooding. In CO_2 huff-n-puff, since injection and production are conducted in a cyclical manner, injectivity of CO_2 is higher. Some work claimed that CO_2 flooding can increase the recovery of shale gas reservoir. We note that those work either used a relatively large matrix permeability (Yu et al. 2014; Fathi and Akkutlu 2014), or the conductivity of shale matrix was significantly increased by modelling natural factures using the dual porosity model (Kim et al. 2017) or multiple interacting continua (MINC) method (Wu et al. 2019). In reality, the permeability of shale matrix is from several to tens of nanodarcy (Pommer and Milliken 2015) and growth of natural fractures are not ideal as that described by dual porosity model or MINC. Breakthrough of CO_2 from injection well to production well is not likely to happen in shale gas reservoir. Thus, CO_2 flooding in shale gas reservoir may not be practical in field operation, unless intensive fracture networks can be generated between two wells by intensive hydraulic fracturing.

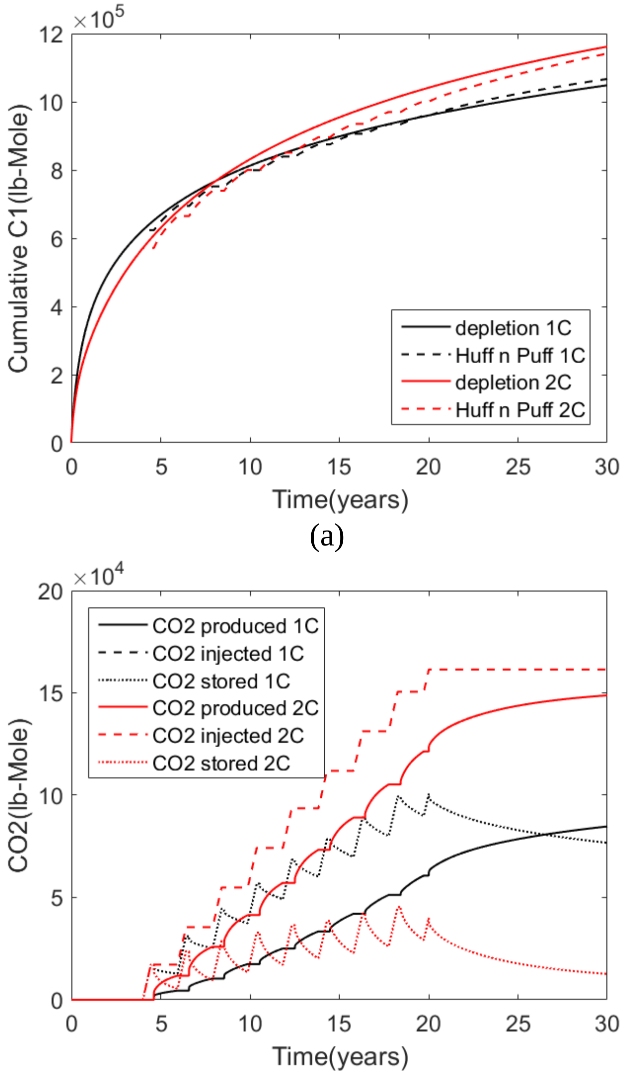

(a)

(b)

Figure 4.3 Cumulative production of methane by CO_2 huff-n-puff (a) and CO_2 flooding (c) and cumulative injected, produced and stored CO_2 by CO_2 huff-n-puff (b) and CO_2 flooding (d).

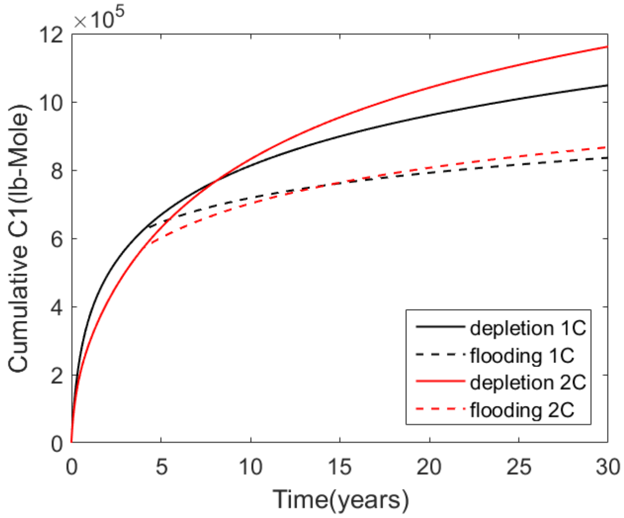

(c)

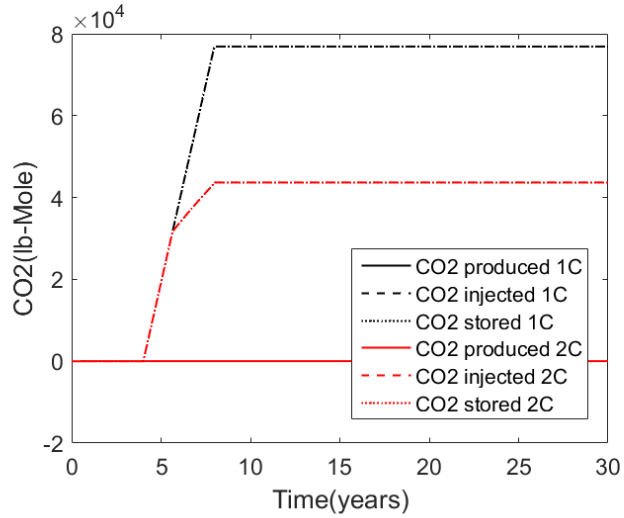

(d)

Figure 4.3 Continued.

To further estimate the effects of distribution of kerogen, the pressures and CO_2 mole fractions in organic and inorganic matrix are presented separately in Figure 4.4. From Figure 4.4(a) and 4.4(c), it is observed that the pressure in organic matrix is always higher than that in inorganic matrix, in both CO_2 huff-n-puff and flooding cases. The observed pressure difference comes from the fact that the inorganic matrix is directly connected to fractures and has a higher permeability. Thus, the mass transfer (pressure decline) between organic and inorganic matrix are in series. Also, it is obvious that the pressure of inorganic matrix is more easily influenced by CO_2 huff-n-puff. From Figure 4.4(b) and 4.4(d), we can see that most of the injected CO_2 enters the inorganic matrix via the fractures while limited amount of CO_2 can enter organic matrix due to the ultralow flow conductivity between organic and inorganic matrix. Since the inorganic matrix has no affinity to CO_2, CO_2 mole fraction in inorganic matrix declines quickly during period of production which explains why most of the injected CO_2 are reproduced when distribution of kerogen is considered explicitly. When kerogen is implicit, CO_2 will quickly replace adsorbed methane via competitive adsorption once enters the shale matrix and thus more CO_2 can be stored. Therefore, it is concluded that the capacity of shale reservoir for CO_2 storage can be overestimated if only one continuum is used in shale matrix. The pressure field and CO_2 mole fraction distribution are also presented in Figure 4.5. Most of pressure decline happens in the stimulated area with fractures. It is not surprising to see that most of the injected CO_2 is in the inorganic matrix and accumulates in the grids that connected to fractures. Due to the ultralow permeability of shale matrix, CO_2 cannot move far from the injection well and the flooding area is quite limited. The small flooding area reduces the effects of CO_2 injection in shale reservoirs, especially in CO_2 flooding case.

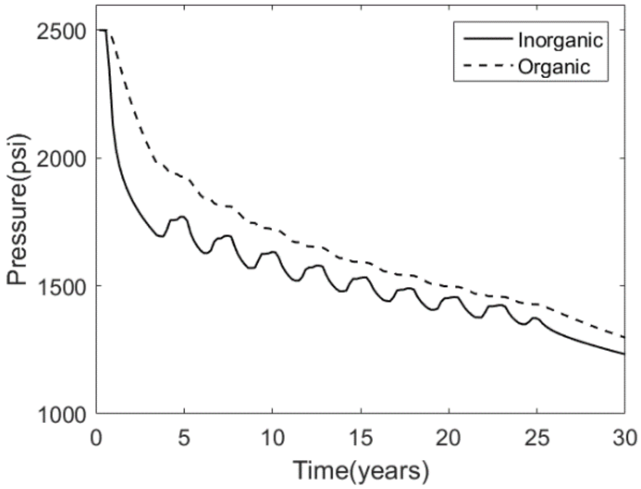

(a)

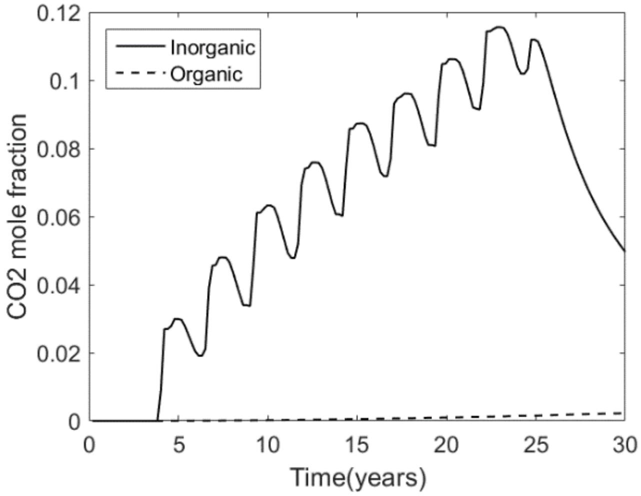

(b)

Figure 4.4 The average reservoir pressure during CO_2 huff-n-puff (a) and CO_2 flooding (c) in organic and inorganic matrix; The average CO_2 mole fraction during CO_2 huff-n-puff (b) and CO_2 flooding (d) in organic and inorganic matrix.

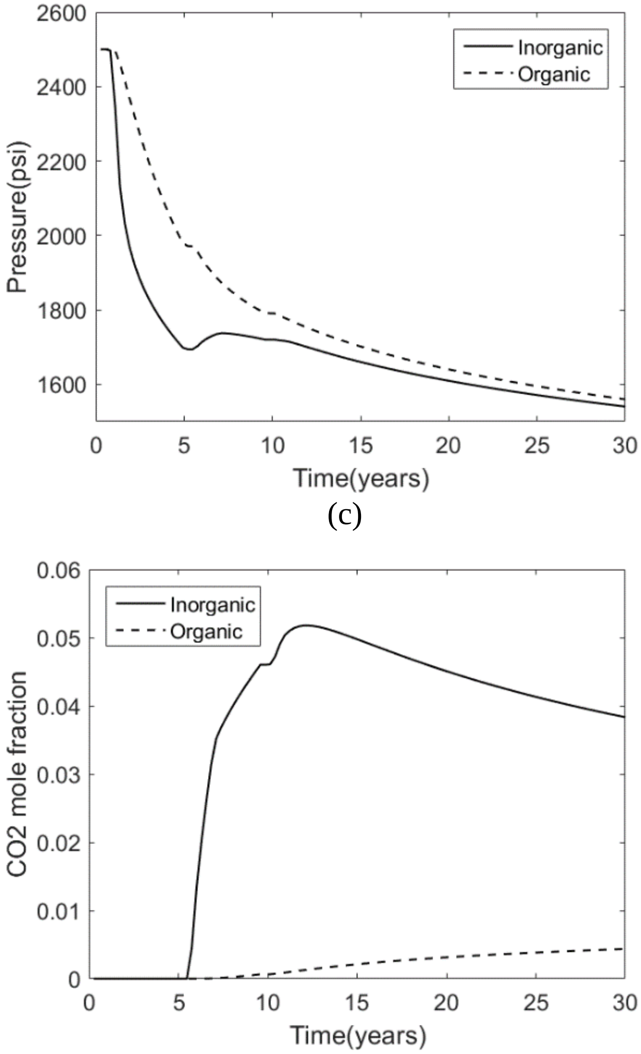

(c)

(d)

Figure 4.4 Continued.

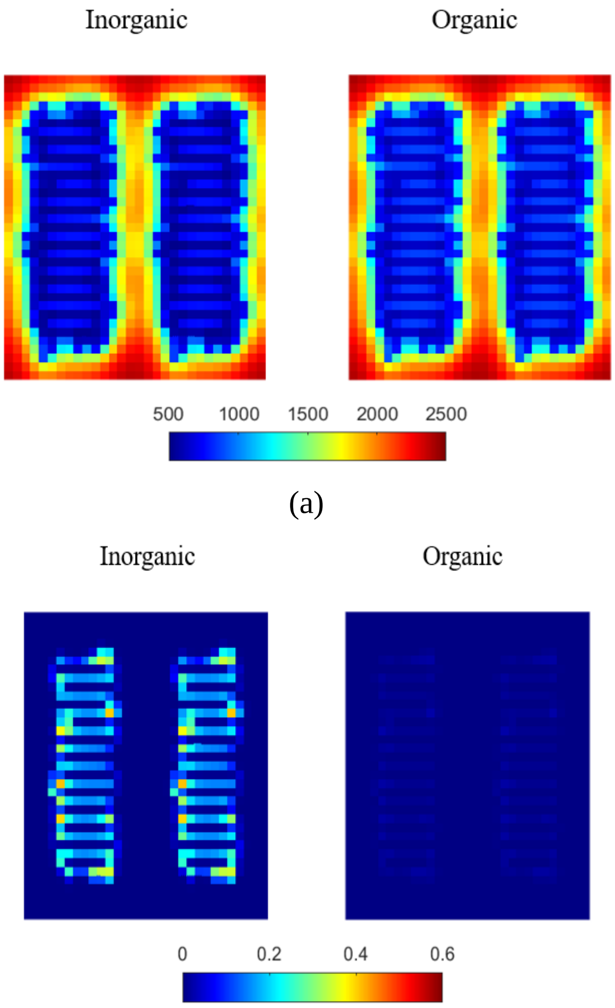

(a)

(b)

Figure 4.5 The pressure distribution during CO$_2$ huff-n-puff (a) and CO$_2$ flooding (c) in organic and inorganic matrix at T=30 years. The CO$_2$ mole fraction distribution during CO$_2$ huff-n-puff (b) and CO$_2$ flooding (d) in organic and inorganic matrix at T=30 years.

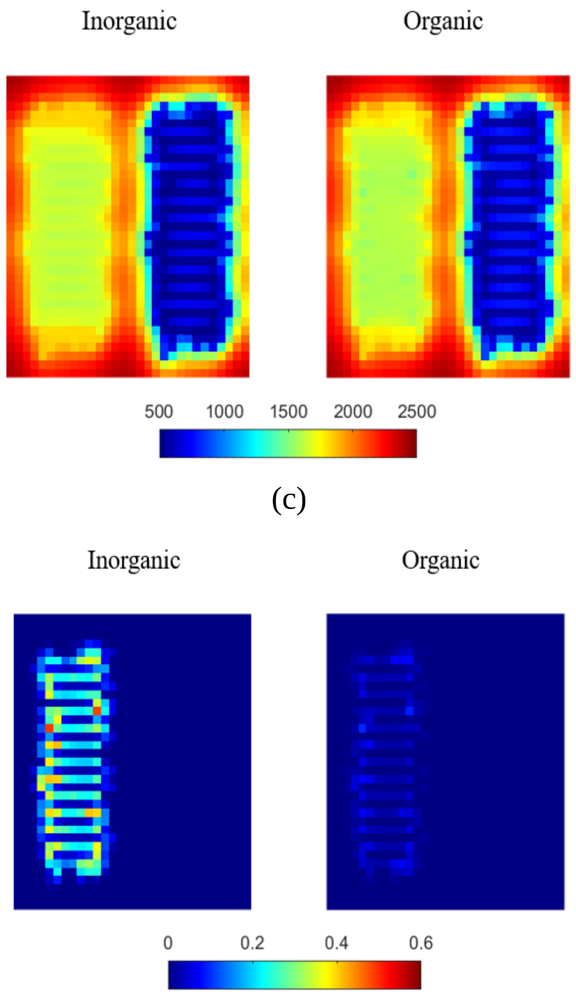

(c)

(d)

Figure 4.5 Continued.

4.3.2 Effect of TOC

By using the multi-porosity model, we are able to quantify TOC in shale matrix explicitly. Different TOC in shale matrix can be obtained by changing the volume fraction of the organic matrix. Note that the transmissibility between organic and inorganic matrix with different TOC needs to be calculated using Eqn. (3.13). Because no CO_2 breakthrough can occur during CO_2 flooding, all the injected CO_2 is stored, and the cumulative gas recovery is decreased. Therefore, only CO_2 huff-n-puff cases are discussed in this section. Figure 4.6 shows the cumulative production of methane when TOC equals to 0.3, 0.4 and 0.5. It is seen that there is a higher gas production rate when TOC is higher if kerogen is considered implicitly. This can be explained that more methane is adsorbed on the surface of rock when TOC is higher, and they can be replaced by the injected CO_2. However, the gas production rate is lower when TOC is higher if kerogen is considered explicitly. As discussed in Section 4.3.1, limited amount of CO_2 can enter organic matrix. Though more kerogen exists in shale matrix when TOC is high, the adsorbed methane cannot be replaced by CO_2 efficiently and the low permeability of organic matrix leads to the lower gas production rate. It is also noted that CO_2 huff-n-puff can slightly improve the gas recovery if kerogen is implicit, while still cannot improve gas recovery if kerogen is explicit. The effects of TOC on CO_2 storage are shown in Figure 4.7. More CO_2 can be stored in shale by adsorption when TOC is higher, if kerogen is considered implicitly. A higher TOC simply means a higher adsorption capacity for CO_2 when one continuum is applied in shale matrix. However, a higher TOC does not necessarily lead to more storage of CO_2 if kerogen is explicit. Though more kerogen exists in shale when TOC is high, most of the injected CO_2 are stored in the inorganic matrix and hard to reach organic matrix. Thus, CO_2 in inorganic matrix is reproduced quickly and cannot be stored in matrix permanently via adsorption.

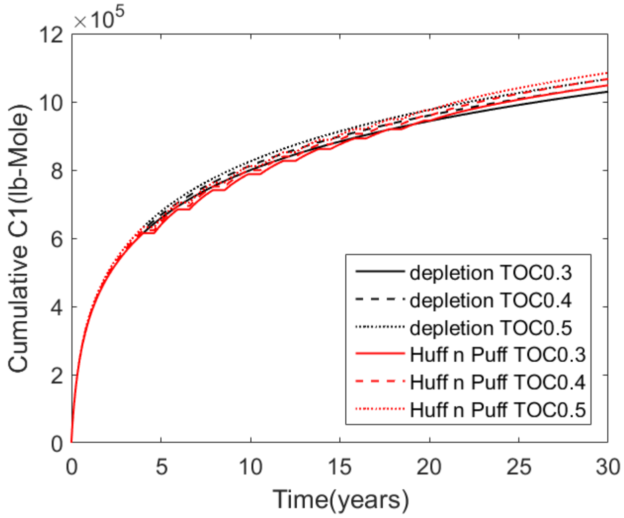

(a)

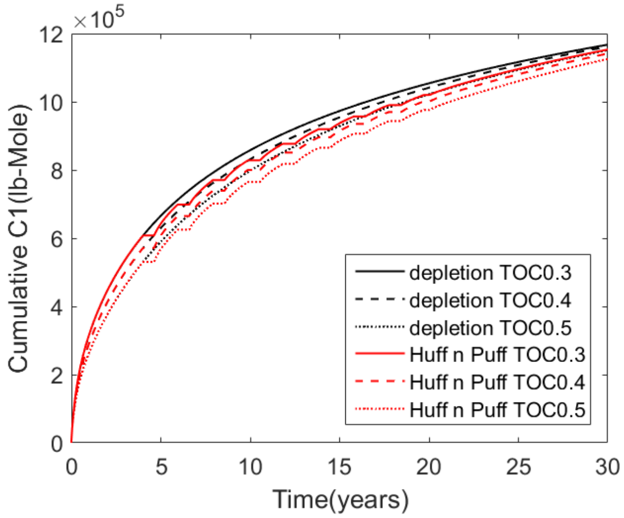

(b)

Figure 4.6 Effect of TOC on the cumulative production of methane when kerogen is implicit (a) and when kerogen is explicit (b).

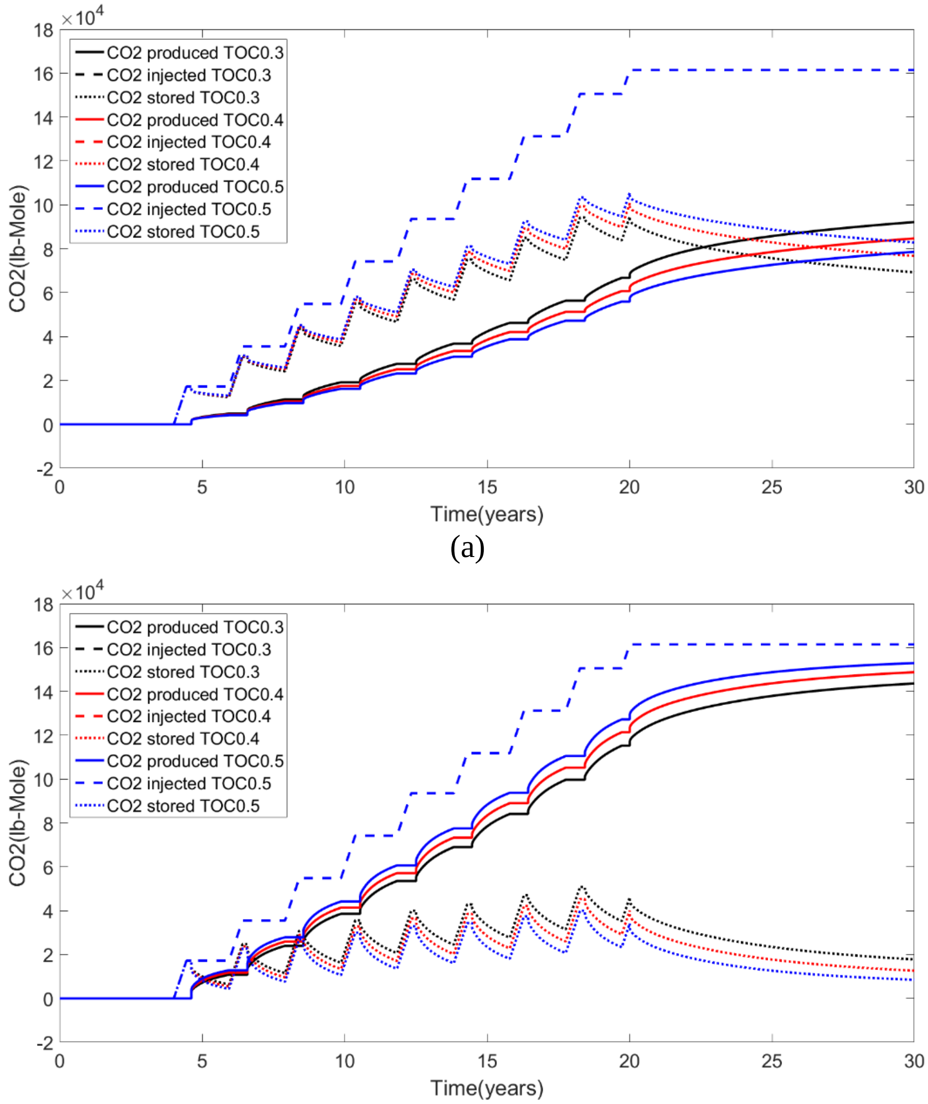

(a)

(b)

Figure 4.7 Effect of TOC on CO_2 storage when kerogen is implicit (a) and when kerogen is explicit (b).

4.3.3 Effect of diffusion coefficient

In this section, we study the effects of diffusion coefficient on the injection of CO_2 into shale gas reservoir. Diffusion has been found a critical factor affecting the injection of CO_2 into shale gas/oil reservoirs (Alharthy et al. 2018; Du and Nojabaei 2019b). The

CO_2 diffusion coefficient has been reported in a wide range from 0.00001 cm2/s to 0.001 cm2/s under reservoir pressure and temperature (Du and Nojabaei 2019a). It is still hard to measure the diffusion coefficient accurately from experiment (Wang and Yu 2019) and many different empirical or analytical relations have been proposed (Du and Nojabaei 2019b). Thus, CO_2 injection with different diffusion coefficients are worth to investigate. Figure 4.8 compares the cumulative production of methane when diffusion coefficient equals to 0.0001, 0.0005 and 0.001 cm2/s. It is found that diffusion coefficient has negligible effects on gas production when kerogen is implicit. A slightly higher gas recovery is observed with higher diffusion coefficient if distribution of kerogen is considered explicitly. The effects of diffusion coefficient on CO_2 storage are shown in Figure 4.9. Again, diffusion coefficient has little effects on CO_2 storage when kerogen is implicit. However, more CO_2 can be stored with a higher diffusion coefficient if kerogen is explicit. Therefore, we can conclude that diffusion coefficient has more significant effects if kerogen is considered explicitly.

The shale matrix only has one continuum with a relatively higher permeability when kerogen is considered implicitly. Viscous flow is therefore the main driving force for CO_2 transport and effect of diffusion is negligible. When kerogen is considered explicitly, the permeability of organic matrix is much lower and the flow conductivity between organic and inorganic matrix is extremely low. Thus, diffusion starts to play a role between organic and inorganic matrix. As discussed in Section 4.3.1, limited amount of CO_2 can enter organic matrix via convection. With a higher diffusion coefficient, more CO_2 can enter the organic matrix by the additional effects of diffusion. More CO_2 in organic matrix leads to a higher gas recovery and better CO_2 storage by means of competitive adsorption.

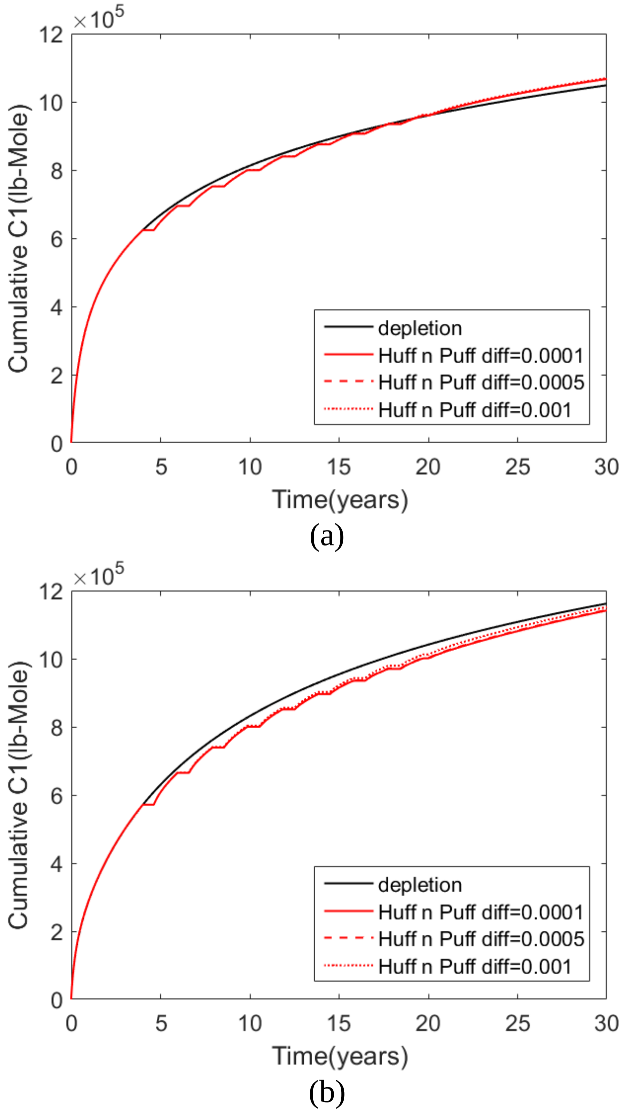

Figure 4.8 Effect of diffusion coefficient on the cumulative production of methane when kerogen is implicit (a) and when kerogen is explicit (b).

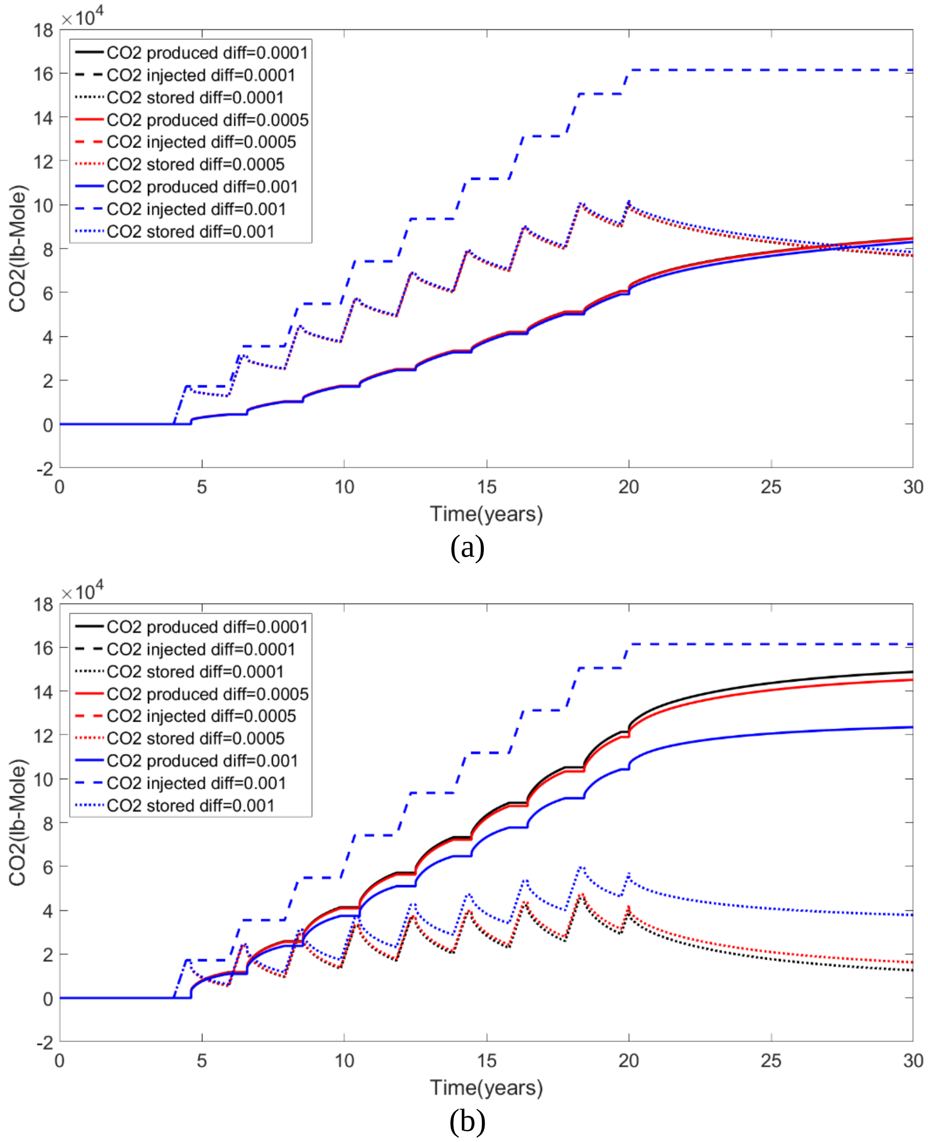
(a)

(b)

Figure 4.9 Effect of diffusion coefficient on CO_2 storage when kerogen is implicit (a) and when kerogen is explicit (b).

4.3.4 Effect of CO_2 injection rate

This section evaluates the effect of CO_2 injection rate on the reservoir performance. As shown in Figure 4.4 of Section 4.4.1, the injectivity of CO_2 is quite low during CO_2 flooding because the bottom-hole pressure quick exceeds the maximum operation pressure (8000 psi). So only CO_2 huff-n-puff with different injection rates are evaluated. Three different injection rates are tested (40, 60, 80 Mscf/day) in this section. Though having a better injectivity compared to CO_2 flooding, the bottom-hole pressure will exceed 8000 psi if the injection rate is larger than 100 Mscf/day during CO_2 huff-n-puff. Thus, the maximum injection rate is set to 80 Mscf/day. Figure 4.10 compares the gas recovery using different gas injection rates. It is observed that a higher injection rate leads to a slightly higher gas recovery if kerogen is implicit. However, the gas recovery is decreased with increasing injection rate if kerogen is considered explicitly. Effects of injection rate on CO_2 storage are presented in Figure 4.11. The higher injection rate can lead to more storage of CO_2 if kerogen is implicit. However, CO_2 injection rate has limited effect on CO_2 storage if kerogen is considered explicitly.

A higher CO_2 injection rate is expected to result in a larger flooding area and sweeping efficiency. When there is one continuum in matrix (kerogen is implicit), a larger flooding area means more CO_2 can contact shale matrix and then more methane can be replaced by CO_2. Thus, a larger injection rate helps both gas recovery and CO_2 storage. This finding is consistent with the results from other works (Yu et al. 2014; Kim et al. 2017). When kerogen is considered explicitly, though more CO_2 injected, most of the injected of CO2 stays in the inorganic matrix and cannot contact kerogen. As discussed in previous sections, CO_2 in inorganic matrix will be reproduced quickly. Therefore, higher injection rates cannot enhance gas recovery or CO_2 storage significantly when kerogen is considered explicitly.

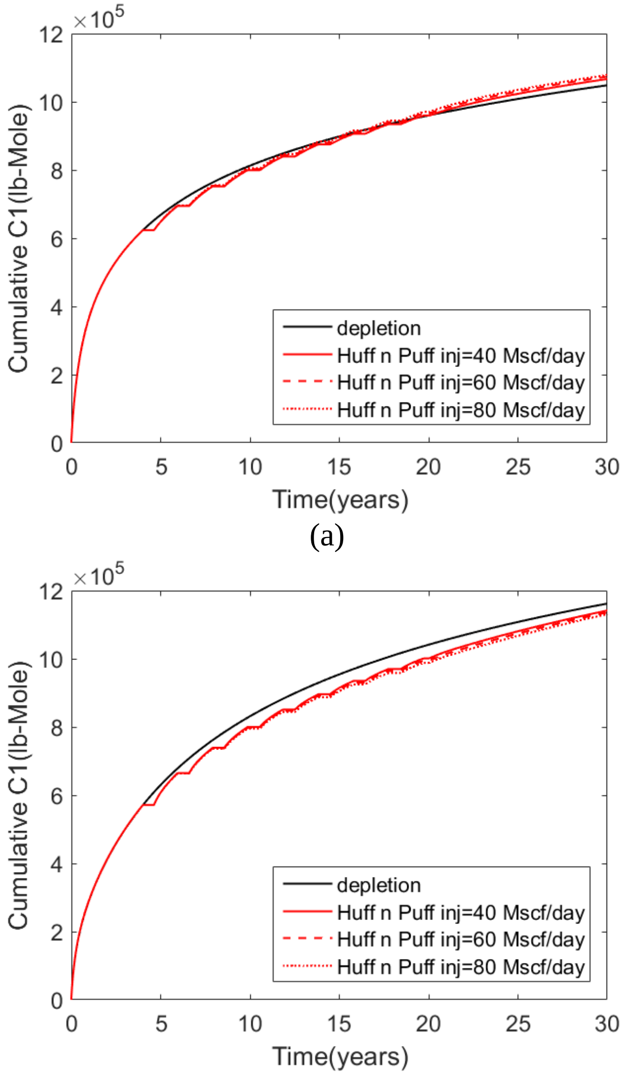

(a)

(b)

Figure 4.10 Effects of CO_2 injection rates on the cumulative production of methane when kerogen is implicit (a) and when kerogen is explicit (b).

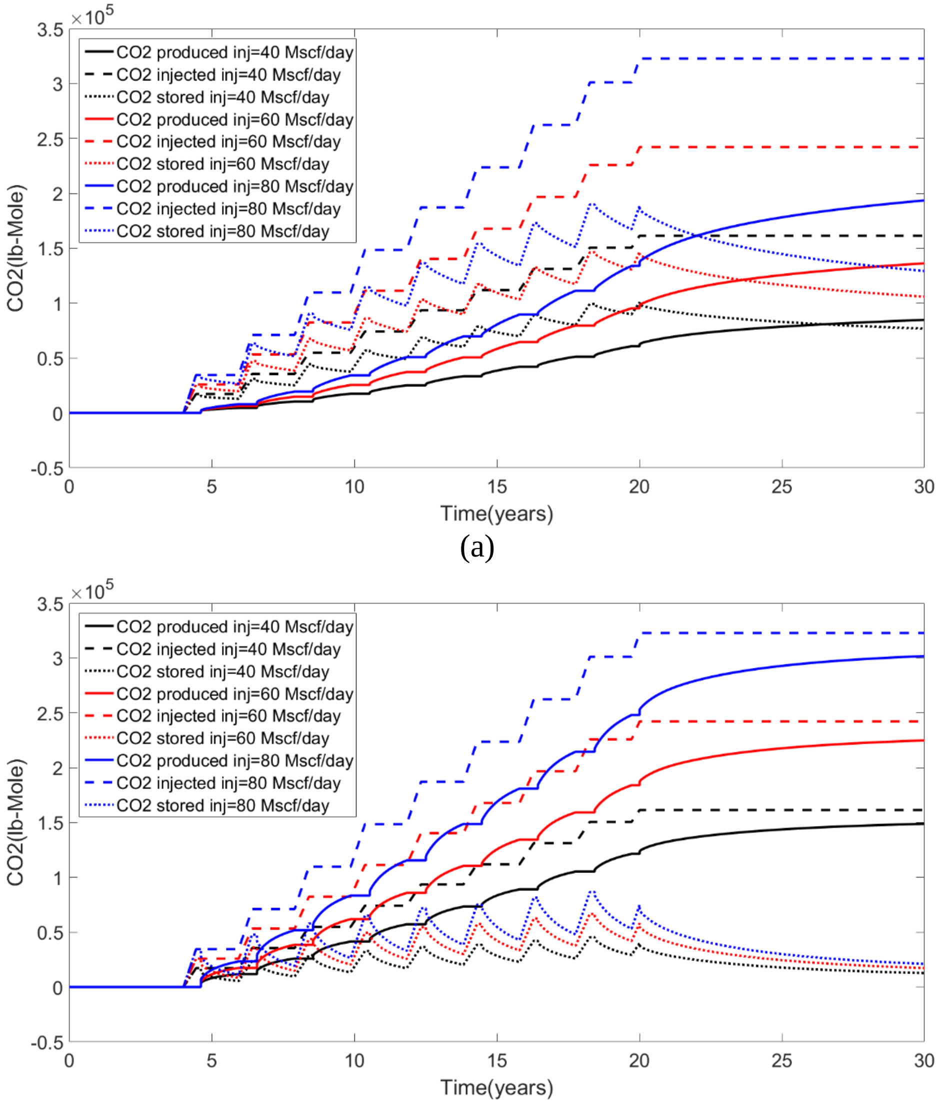

(a)

(b)

Figure 4.11 Effects of CO_2 injection rates on CO_2 storage when kerogen is implicit (a) and when kerogen is explicit (b).

4.4 Conclusions and Discussions

In this Chapter, simulation of gas injection into shale reservoir is conducted. Specifically, the dispersed distribution of kerogen in shale matrix is comprehensively evaluated for both enhanced gas recovery and permeant CO_2 sequestration. To explicitly describe kerogen, shale matrix is divided into inorganic matrix and organic matrix by using the multi-porosity model. The organic matrix is embedded inside inorganic matrix and discontinuous between simulation grids due to its dispersed nature. Hydraulic/natural fractures are described explicitly using embedded discrete fracture model and are directly connected to inorganic matrix. The mass transfers between fractures, inorganic matrix and organic matrix are in series.

Simulation results show that CO_2 flooding is not preferred for enhanced gas recovery or CO_2 storage because the CO_2 sweeping efficiency is quite low due to the ultralow permeability of shale matrix. Though all injected CO_2 can be kept underground, the gas injectivity during CO_2 flooding is not satisfactory. On the other hand, CO_2 huff-n-puff shows a better performance compared to CO_2 flooding. Gas recovery is increased if kerogen is implicit and slightly decreased if kerogen is considered explicitly, by using CO_2 huff-n-puff. In terms of CO_2 storage, more than 50% of the injected CO_2 can be stored in shale if kerogen is implicit, while only 10%-20% of injected CO_2 can be stored when kerogen is considered explicitly. When one continuum is applied in shale matrix, every matrix grid has capacity for CO_2 adsorption. Once CO_2 enters the matrix grids, methane can be replaced by CO_2 immediately via competitive adsorption. However, when dispersed distribution of kerogen is considered, most of the injected CO_2 enter inorganic matrix while limited amount of CO_2 can have contact with kerogen. Since adsorption only happens in organic matrix, the CO_2 in inorganic matrix will be reproduced quickly without replacing adsorbed methane. Therefore, the enhance gas recovery from CO_2 injection and

CO_2 storage capacity of shale reservoir can be overestimated if the dispersed nature of kerogen is not well described.

Some critical factors that affecting the performance of CO_2 injection are investigated. Firstly, different TOC can be modeled explicitly by changing the volume fraction of kerogen. It is found that a higher TOC has positive effects on both gas recovery and CO_2 storage if kerogen is implicit. High TOC simply means a larger adsorption capacity for CO_2 when only one continuum is applied in matrix. When kerogen is considered explicitly, a higher TOC does not necessarily have a positive effect because CO_2 cannot easily enter organic matrix, though more kerogen exists. Secondly, diffusion plays an important role when kerogen is considered explicitly. More CO_2 can enter organic matrix via diffusion and be stored permanently by adsorption. Effects of diffusion are negligible if only one continuum exists in shale matrix because the viscous flow will be the dominant mechanism. Thirdly, a higher injection rate increases the flooding area of CO_2 and more methane can be replaced by CO_2 if kerogen is implicit. When kerogen is considered explicitly, though more CO_2 injected using a higher injection rate, most of injected CO_2 is stored in inorganic matrix and will be reproduced quickly. Thus, a higher injection rate does not have a positive effect.

From the discussions above, we conclude that the nature of dispersed distribution of kerogen in shale matrix will decrease the efficiency of CO_2 injection into shale gas reservoirs. The highly connected and more permeable inorganic matrix make the injected CO_2 bypass the kerogen. Therefore, limited amount of CO_2 get contact with kerogen where the mechanism of competitive adsorption can happen. This study provides a profound view of accurately evaluating the capacity of CO_2 storage and the potential of enhanced gas recovery in shale gas reservoir. It reveals that the dispersed nature of kerogen acting as a crucial factor that affecting the success of CO_2 storage in field operations.

CHAPTER V

PORE-SCALE MODELS FOR PHASE EQUILIBRIUM [*]

5.1 Introduction

Simulations of multiphase equilibrium and multiphase flow are constantly needed when one attempts to predict the dynamics of natural and industrial multiphase systems. Numerical methods have been developed to solve multiphase problems including the phase field method (Cahn and Hilliard 1958; Cahn and Hilliard 1959), the density functional method (Demianov et al. 2011), and the lattice Boltzmann (LB) method (Gunstensen et al. 1991; Gunstensen and Rothman 1993; Shan and Chen 1993; Shan and Doolen 1995; Swift et al. 1995). Among these methods, LB method has shown great advantages in modeling complex multiphase problems and has been successfully applied to simulations of multiphase flows in microfluidics (Wu et al. 2012; Zhang 2011), heat/mass exchangers (Tarokh et al. 2013), and porous media (Pan et al. 2004; Li et al. 2005; Huang et al. 2017). In multiphase LB models, there is no need for explicit interface tracking or interface capturing, which serves as an attractive reason for using LB to study multiphase flow problems. In multiphase LB methods, pseudopotential LB model proposed by Shan and Chen (1993) is a popular choice due to its straightforward implementation (Chen et al. 2014). Using a pseudopotential to account for interparticle

---

[*] Part of data reported in this chapter is reprinted with permission from “Thermodynamic consistency of a pseudopotential lattice Boltzmann fluid with interface curvature” by Huang, J., Yin, X., Killough, J., 2019. Physical Review E, Volume 100, 053304, Copyright 2019 by American Physical Society.

interactions (Shane and Chen 1993), one component can spontaneously segregate into two phases with different densities at proper pressure and temperature.

Compared to the class of LB models built by free energy formulations (Wagner 2006; Wagner and Pooley 2007), thermodynamic consistency of pseudopotential LB models is a major requirement for simulation of phase separation (Chen et al. 2014). Shan and Chen (1994) proposed that thermodynamic consistency of pseudopotential models can be achieved by setting $\psi = \psi_0 \exp(-\rho_0/\rho)$, where ψ is pseudopotential, ρ is density of fluid, ψ_0 and ρ_0 are constants. However, this exponential pseudopotential (Shan 2008; Sbragalia and Shan 2011) cannot recover realistic equation of state (EOS) and thus cannot be used to model the behavior of real fluids (Khajepor et al. 2015). Yuan and Schaefer (2006) incorporated several realistic EOS into pseudopotential model by directly associating pseudopotential with pressure described by EOS. Zhang and Tian (2008) modified the equilibrium distribution function with a free parameter to incorporate EOS. Zhang and Chen (2003) proposed another scheme to incorporate arbitrary EOS into LB simulations. In their method, interactive force was expressed as a gradient of potential that can be related to EOS. These studies were all limited to relatively low density ratios and the simulated equilibrium vapor/liquid densities showed noticeable deviations from those obtained from Maxwell construction. Other researchers found that calculation of the interactive force affects phase transitions. In the original Shan-Chen model (1993), interactive force at a fluid node was calculated by multiplying the local pseudopotential with the local gradient of pseudopotential. The resulted vapor densities significantly deviated from analytical predictions, especially at low temperatures. Higher-order corrections were included into the forcing terms which lead to an accurate phase diagram and a constant pressure across the interface (Wagner 2006). Kupershtokh et al. (2009) proposed a hybrid method by combining two ways of calculating the interactive force, which were called local approximation and mean-value approximation in their paper. By tuning the weight of the two methods in their new interactive force term, larger density ratios and coexistence curves with higher accuracy were obtained. Gong and Cheng (2012) studied droplet motion and coalescence using a similar strategy. LB models with higher orders have also been developed to minimize spurious currents and improve thermodynamic consistency. These models use more neighbors when calculating interactive forces (Khajepor et al. 2015; Sbragaglia et al. 2007; Shan 2006). Khajepor et al. (2015) extended single-pseudopotential interaction to multi-pseudopotential interactions and the force at a given node consisted of contributions of more than one potential. Sbragalia et al. (2007) proposed a multi-range pseudopotential model to include interactions from more neighbors. Their approach allows density ratio and surface tension be controlled independently. On the incorporation of the calculated interactive force into LB model, many approaches have been developed. The velocity shift method modifies velocity in the equilibrium distribution function (Shan and Chen 1993) and has been applied to the original Shan-Chen model. Guo et al. (2002) proposed a forcing scheme by directly adding discrete forces into the evolution equation of distribution functions. Kupershtokh et al. (2009) derived an exact difference method (EDM) directly from Boltzmann equation. There are also other forcing schemes such as Luo’s forcing scheme (Luo 1998) and He’s forcing scheme (He et al. 1998). Researchers have evaluated the effect of different forcing schemes theoretically (Li et al. 2012) and numerically (Huang et al. 2011). It was found that with the velocity shift method the simulated vapor density was much lower than those from Maxwell construction, and density ratio and surface tension were dependent on the relaxation time (Huang et al. 2011). Larger density ratios and thermodynamic consistency can be achieved by using EDM together with the hybrid interactive force (Kupershtokh et al. 2009; Gong and Cheng 2012). Density ratio and interfacial tension were only slightly affected by relaxation time when density ratio was large and interface was curved when using EDM method (Li et al. 2012; Huang et al. 2011). Guo's forcing scheme has a higher order of accuracy (Huang et al. 2011) and the effect of relaxation time is smaller than EDM (Hu et al. 2015). Li et al. (2012) modified Guo's forcing scheme to recover correct hydrodynamics and improved numerical stability and thermodynamic consistency. Multiple-relaxation-time (MRT) model has also been applied to pseudopotential LB to enhance numerical stability at large density ratios (Li et al. 2013; Shi et al. 2015; Zhang et al. 2014). With all the aforementioned efforts made, thermodynamic inconsistency in pseudopotential LB can be largely suppressed.

In this Chapter, we first formulate the pseudo-potential lattice Boltzmann model with ability to incorporate any EOS. Then the hybrid interactive force and EDM forcing schemes (Kupershtokh et al. 2009; Gong and Cheng 2012) is applied to suppress the thermodynamic inconsistency of original pseudopotential LB. Then the model is validated by comparing the simulated phase equilibrium across a flat interface with results obtained from Maxwell construction and EOS.

5.2 Pseudo-potential lattice Boltzmann model

In the lattice Boltzmann method, fluid dynamics and equilibrium are described by the evolution and steady distribution of collections of pseudoparticles. The evolution equation when using BGK collision operator (Qian et al. 1992) can be written as

$$f_i(\boldsymbol{x} + \boldsymbol{c}_i \Delta t, t + \Delta t) - f_i(\boldsymbol{x}, t) = -\frac{1}{\tau}\left[f_i(\boldsymbol{x}, t) - f_i^{eq}(\boldsymbol{x}, t)\right] + \Delta f_i(\boldsymbol{x}, t) \tag{5.1}$$

where $f_i(\boldsymbol{x}, t)$ is the particle distribution function at position $\boldsymbol{x}$ and time t, τ is the relaxation time, $\boldsymbol{c}_i$ is a discrete set of velocity vectors, and Δt is the time step. $\Delta f_i(\boldsymbol{x}, t)$ is the external body force term. $f_i^{eq}(\boldsymbol{x}, t)$ is the equilibrium distribution function given by

$$f_i^{eq} = \rho \omega_i \left(1 + \frac{\boldsymbol{c_i}.\boldsymbol{u}}{c_s^2} + \frac{(\boldsymbol{c_i}.\boldsymbol{u})^2}{2c_s^4} - \frac{\boldsymbol{u}^2}{2c_s^2}\right) \tag{5.2}$$

where ω_i is the weighting coefficients and c_s is lattice speed of sound. For D2Q9 model, the weighting coefficient ω_i are $\omega_1 = 4/9,\ \omega_{2-5} = 1/9,\ \omega_{6-9} = 1/36$ and the discrete set of velocity vectors is

$$\boldsymbol{c}_i = \begin{cases} (0,0) \ \ i = 1 \\ (\pm 1,0), (0, \pm 1) \ \ i = 2 \sim 5 \\ (\pm 1, \pm 1) \ \ i = 6 \sim 9 \end{cases} \tag{5.3}$$

For D3Q19 model, the weighting coefficient ω_i are $\omega_1 = 1/3,\ \omega_{2-7} = 1/18,\ \omega_{8-19} = 1/36$ and $\boldsymbol{c}_i$ are given as follows

$$\boldsymbol{c}_i = \begin{cases} (0,0,0) \ \ i = 1 \\ (\pm 1,0,0), (0, \pm 1,0), (0,0, \pm 1) \ \ i = 2 \sim 7 \\ (\pm 1, \pm 1,0), (\pm 1,0, \pm 1), (0, \pm 1, \pm 1) \ \ i = 8 \sim 19 \end{cases} \tag{5.4}$$

The fluid viscosity is determined by relaxation time through

$$\upsilon = c_s^2 (\tau - 0.5) \Delta t \tag{5.5}$$

If MRT collision operator (d'Humières 2002) is applied, the evolution equation is in the following form

$$f_i(\boldsymbol{x}+\boldsymbol{c}_i\Delta t, t+\Delta t)-f_i(\boldsymbol{x},t)=-(\mathbf{M}^{-1}\mathbf{SM})_{ij}(f_j-f_j^{eq})+\Delta f_i(\boldsymbol{x},t) \qquad (5.6)$$

where $\mathbf{M}$ is the transformation matrix (d'Humières 2002) and $\mathbf{S}$ is the diagonal collision matrix in the moment space. For D2Q9 model, $\mathbf{S} \equiv \text{diag}\,(0, s_e, s_\varepsilon, 0, s_q, 0, s_q, s_\nu, s_\nu)$ and relaxation parameters are chosen as: $s_q = 8(2-1/\tau)/(8-1/\tau)$, $s_e = s_\varepsilon = s_\nu = 1/\tau$. For D3Q19 model, $\boldsymbol{S} \equiv \text{diag}\,(0, s_e, s_\varepsilon, 0, s_q, 0, s_q, 0, s_q, s_\nu, s_\pi, s_\nu, s_\pi, s_\nu, s_\nu, s_\nu, s_t, s_t, s_t)$ and relaxation parameters are chosen as: $s_q = s_t = 8(2-1/\tau)/(8-1/\tau)$, $s_e = s_\varepsilon = s_\nu = s_\pi = 1/\tau$. It is known that MRT operator can enhance numerical stability and suppress spurious currents (Zhao and Fan 2010). We therefore used MRT operator in this study. In lattice Boltzmann, fluid density and fluid velocity can be obtained from the zeroth and the first moments of the distribution function

$$\rho = \sum_i f_i \qquad (5.7a)$$

$$\rho\boldsymbol{u} = \sum_i f_i \boldsymbol{c_i} = \sum_i f_i^{eq} \boldsymbol{c_i} \qquad (5.7b)$$

In order to model phase transition, Shan and Chen (1993) introduced inter-particle interactions in their pseudopotential LB model. The original form of the interactive force is (Shan and Chen; 1993; Yuan and Schaefer 2006)

$$\boldsymbol{F}(\boldsymbol{x})_{inter} = -c_0 \mathrm{g}\psi(\boldsymbol{x})\nabla\psi(\boldsymbol{x}) \qquad (5.8)$$

where $\psi(\boldsymbol{x})$ is the effective mass, g is the strength of interaction and c_0 is a constant depending on the lattice structure. $c_0 = 6$ for D2Q9 and D3Q19 models. One way of introducing an equation of state (EOS) into pseudopotential LB is to associate the effective mass with the non-idealness of the fluid (Yuan and Schaefer 2006)

$$p = c_s^2\rho + \frac{\mathrm{g}}{2}c_0\psi^2 \tag{5.9}$$

Given pressure from a pre-determined EOS, the effective mass can be calculated as

$$\psi = \sqrt{\frac{2(p - c_s^2\rho)}{c_0\mathrm{g}}} \tag{5.10}$$

On a lattice, the interactive force can be further expressed as

$$\boldsymbol{F}(\boldsymbol{x})_{inter} = -\psi(\boldsymbol{x})\sum \mathrm{G}(\boldsymbol{x},\boldsymbol{x}')\psi(\boldsymbol{x},\boldsymbol{x}')(\boldsymbol{x}' - \boldsymbol{x}) \tag{5.11}$$

where $\mathrm{G}(\boldsymbol{x},\boldsymbol{x}')$ is Green's function that satisfies $\mathrm{G}(\boldsymbol{x},\boldsymbol{x}') = \mathrm{G}(\boldsymbol{x}',\boldsymbol{x})$. When only considering the nearest and next nearest neighbors, $\mathrm{G}(\boldsymbol{x},\boldsymbol{x}')$ is given by

$$(\boldsymbol{x},\boldsymbol{x}') = \begin{cases} \mathrm{g}_1, & |\boldsymbol{x}' - \boldsymbol{x}| = 1 \\ \mathrm{g}_2, & |\boldsymbol{x}' - \boldsymbol{x}| = \sqrt{2} \\ 0, & otherwise \end{cases} \tag{5.12}$$

where $\mathrm{g}_1 = 2\mathrm{g}, \mathrm{g}_2 = 0.5\mathrm{g}$ for D2Q9 and $\mathrm{g}_1 = \mathrm{g}, \mathrm{g}_2 = 0.5\mathrm{g}$ for D3Q19. It has been pointed out that the interactive force in Eqn. (5.8) can also be written as (Gong and Cheng 2012)

$$\boldsymbol{F}(\boldsymbol{x})_{inter} = -\frac{c_0\mathrm{g}}{2}\nabla(\psi^2(\boldsymbol{x})) \tag{5.13}$$

On a lattice, it can be further expressed as

$$\boldsymbol{F}(\boldsymbol{x})_{inter} = -\frac{1}{2}\sum \mathrm{G}(\boldsymbol{x},\boldsymbol{x}')\psi^2(\boldsymbol{x},\boldsymbol{x}')(\boldsymbol{x}' - \boldsymbol{x}) \tag{5.14}$$

It has been found that combining Eqn. (5.11) and Eqn. (5.14) can enhance numerical stability and improve thermodynamic consistency of pseudo-potential LB (Kupershtokh et al, 2009; Gong and Cheng 2012; Zarghami et al. 2015). The hybrid interactive force can be written as (Gong and Cheng 2012)

$$\boldsymbol{F}(\boldsymbol{x})_{inter} = -\beta\psi(\boldsymbol{x})\sum \mathrm{G}(\boldsymbol{x},\boldsymbol{x}')\psi(\boldsymbol{x},\boldsymbol{x}')(\boldsymbol{x}' - \boldsymbol{x}) - \frac{1-\beta}{2}\sum \mathrm{G}(\boldsymbol{x},\boldsymbol{x}')\psi^2(\boldsymbol{x},\boldsymbol{x}')$$

$$(\boldsymbol{x}' - \boldsymbol{x}) \tag{5.15}$$

where β is a weighting parameter.

As mentioned in the introduction, different types of EOS can be employed into pseudo-potential LB by changing the form of the effective mass. In this work, we used Carnahan-Starling (CS) EOS since it can handle high density ratios (Yuan and Schaefer 2006; Huang et al. 2011). The equation for CS EOS is

$$p = \rho RT \frac{1+b\rho/4+(b\rho/4)^2-(b\rho/4)^3}{(1-b\rho/4)^4} - a\rho^2 \tag{5.16}$$

where $a = 0.4963R^2T_c^2/p_c$, $b = 0.18727RT_c/p_c$, T is temperature, R is gas constant, T_c and p_c are critical temperature and critical pressure, respectively. In this study, we set a = 1, b = 4 and R = 1 for all simulations. With these constants, the critical point of CS fluid is $T_c = (0.18727a)/(0.4963bR) = 0.0943$, $P_c = 0.18727RT_c/b = 0.00442$. When using CS EOS, the corresponding effective mass can be calculated as

$$\psi(\rho) = \sqrt{\frac{2(p-c_s^2\rho)}{c_0 g}} = \sqrt{\frac{2\left(\rho RT\frac{1+b\rho/4+(b\rho/4)^2-(b\rho/4)^3}{(1-b\rho/4)^4}-a\rho^2-c_s^2\rho\right)}{c_0 g}} \tag{5.17}$$

It should be noted that g will be cancelled out when calculating $\boldsymbol{F}_{inter}$ (Yuan and Schaefer 2006).

To add the interactive force into lattice Boltzmann model, several forcing schemes have been proposed such as the velocity shift method (Shan and Chen 1993), Guo's method (Guo et al. 2002) and EDM method (Kupershtokh et al. 2009). In this study, EDM forcing method was applied. When using EDM forcing method, an extra forcing term is needed in the evolution equation (Eqn. (4.1)) following (Kupershtokh et al. 2009)

$$\Delta f_i(\boldsymbol{x},t) = f_i^{eq}(\rho(\boldsymbol{x},t), \boldsymbol{u}+\Delta\boldsymbol{u}) - f_i^{eq}(\rho(\boldsymbol{x},t), \boldsymbol{u}) \tag{5.18}$$

where $\Delta \boldsymbol{u} = (\boldsymbol{F}_{inter}\, \Delta t)/\rho(\boldsymbol{x}, t)$.

5.3 Validation LB model with EOS

In this section, we evaluate the thermodynamic consistency of pseudo-potential lattice Boltzmann model by comparing simulated results with those from Maxwell construction. 2D and 3D cases with flat interfaces were simulated. The dimension of the computation domain for 2D cases is $L_x \times L_y = 20 \times 200$ and for 3D cases is $L_x \times L_y \times L_z = 20 \times 200 \times 20$, with periodic boundary condition applied in all directions. Sub-domain $50 < y < 150$ was initialized with liquid whereas the rest was initialized with vapor. The density field was initialized using the method in (Huang et al. 2011)

$$\rho(y) = \rho_v + \frac{\rho_l - \rho_v}{2} \times abs\left(\tanh\left(\frac{2(y-50)}{\mathrm{W}}\right) - \tanh\left(\frac{2(y-150)}{\mathrm{W}}\right)\right) \tag{5.19}$$

where ρ_v and ρ_l are densities of vapor and liquid respectively from Maxwell construction. W is the initial width of interface, which was set as 5 in flat-interface cases. Each simulation was carried out for 40,000 time steps to ensure that steady state was reached.

The two different forms of interactive force, Eqn. (5.11) and Eqn. (5.15), were first compared. These two forms are henceforth mentioned as the SC method and the β method, respectively. Note that the β method is reduced to the SC method when $\beta = 1$. Relaxation time $\tau = 1$ in all simulations. Simulation results indicate that 2D and 3D cases generate the same density-pressure isotherms when interface is flat. Thus, only the results from 2D cases are presented in this section. The coexistence curves described by reduced temperature ($T_r = T/T_c$) and reduced density ($\rho_r = \rho/\rho_c$) are plotted in Figure 5.1.

Comparison with Maxwell construction shows that both liquid density and vapor density were underestimated when using the SC method, especially the vapor density at low temperatures, consistent with (Gong and Cheng 2012; Huang et al. 2011; Hu et al. 2015). When using the β method, liquid and vapor densities matched well with results from Maxwell construction after tuning the value of β. For these flat-interface cases, the best β is 1.22. Reduced saturation pressures ($p_r = p/p_c$) at different temperatures were calculated using CS EOS and they are compared to simulation results in Figure 5.2. For flat-interface cases, saturation liquid pressure and saturation vapor pressure are identical. Simulated saturation pressures from the SC method are lower than saturation pressures from CS EOS, which is not surprising given that SC method underestimates densities of both phases. Simulated saturation pressures from the β method, on the other hand, agree well with those from CS EOS when $\beta = 1.22$.

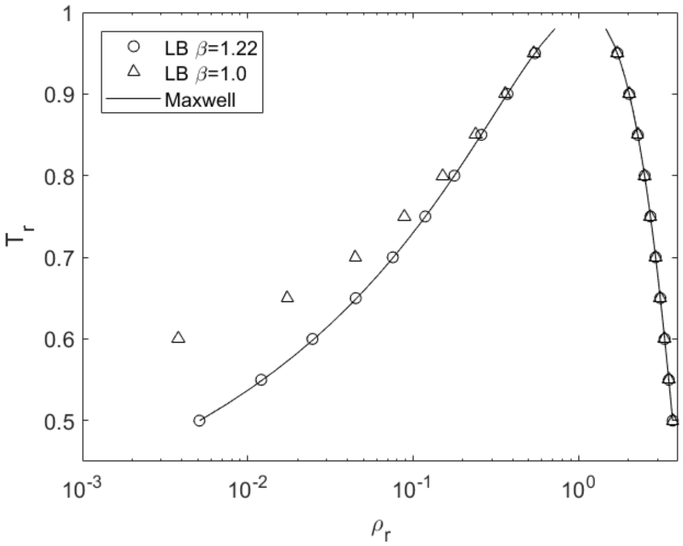

Figure 5.1 Coexistence curve of CS fluid in flat-interface cases.

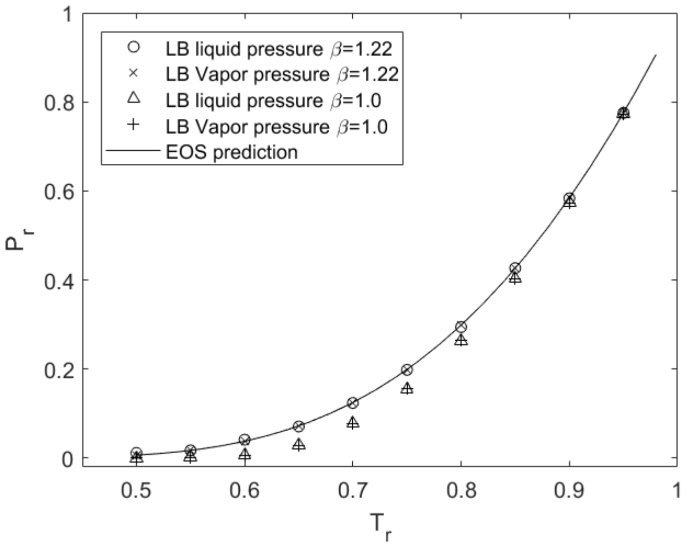

Figure 5.2 Saturation pressures of CS fluid at different temperature in flat-interface cases.

It is known that relaxation time τ could affect densities of liquid and vapor phases (Hu et al. 2015). For this reason, we next examined flat-interface cases using different relaxation times. Figure 5.3 shows liquid-vapor density ratio as a function of reduced temperature. It is seen that simulated density ratios are practically independent of τ among $\tau = 1.0$, $\tau = 0.75$, and $\tau = 1.5$.

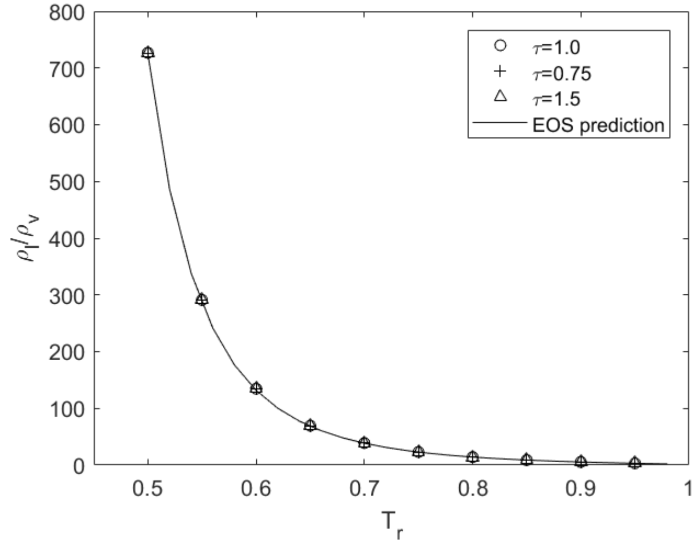

Figure 5.3 Liquid-vapor density ratios obtained for different values of τ in flat-interface cases.

5.4 Summary and Conclusions

In this Chapter, the pseudo-potential lattice Boltzmann model is introduced and formulated. By correlating the pressure using pseudo-potential and that using EOS, the phase equilibrium can be modeled with any kind of EOS. When temperature is low and density ratio between liquid and vapor is large, the effects of grid anisotropic become significant and vapor pressure can be overestimated. To overcome the thermodynamics inconsistency of pseudo-potential, a hybrid force model called β method was applied to calculate the interactive force. By tuning the weighting parameter β, thermodynamics inconsistency can be largely suppressed. When the interface is flat, simulated liquid and vapor densities using the β method agreed well with those obtained from Maxwell construction after tuning the value of β to 1.22. Simulated saturation pressures also matched well with theoretical results from EOS. Also, the effect of relaxation time was characterized. It is also found that thermodynamic consistency of pseudo-potential model is not influenced by relaxation time when interface is flat.

CHAPTER VI

PORE-SCALE SIMULATION OF PHASE BEHAVIOR IN NANOPORES [*]

6.1 Introduction

In most previous studies on the thermodynamic consistency of pseudopotential LB fluids, densities across a flat or curved interface were always directly compared to the results from Maxwell construction (Yuan and Schaefer 2006; Gong and Cheng; Huang et al. 2011). In thermodynamics of phase equilibrium, however, it is well recognized that the existence of Laplace pressure across a curved interface affects both equilibrium densities and saturation pressures. For instance, saturation vapor pressure can be enhanced over small convex liquid or solid surfaces (Sir William Thomson 1871). Equilibrium densities and saturation pressures across curved interfaces therefore should not be directly compared to those from Maxwell construction. Lee and Fischer (2006) in a 2D droplet study compared the results from a LB simulation with pressures and densities predicted by Young-Laplace equation. Kikkinides (2008) studied the effect of droplet size on equilibrium densities of liquid and vapor phases. However, there is no work that comprehensively evaluated the thermodynamic behavior of LB fluids under effect of large Laplace pressure. Shift in the phase equilibrium due to interface curvature could be critical when LB is applied to realistic nanoscale flows. In view of this, this Chapter aims to

---

[*] Part of data reported in this chapter is reprinted with permission from “Thermodynamic consistency of a pseudopotential lattice Boltzmann fluid with interface curvature” by Huang, J., Yin, X., Killough, J., 2019. Physical Review E, Volume 100, 053304, Copyright 2019 by American Physical Society.

thoroughly study the phase behavior of LB fluids with curved interface. When interface is curved, the effect of Laplace pressure on equilibrium densities and saturation pressures of both phases were examined by comparing with Kelvin equation. Besides, by non-dimensionalizing the calculated interfacial tensions, the length scale associated with the lattice spacing of pseudopotential LB was determined for different fluids. Interface thicknesses that arise from this comparison are in good agreement with those measured from experiments and molecular dynamics.

6.2 Simulation of phase equilibrium under effect of curved interface

6.2.1 Thermodynamic consistency of pseudo-potential model with curved interface

In Section 5.3, we have demonstrated that by using the β method to calculate the interactive force and tuning the value of β, thermodynamic consistency can be achieved in flat-interface cases. In this section, we evaluate the thermodynamic consistency of the β method in cases with curved interfaces. We set β as 1.22 initially, following the success of flat-interface cases. Two types of vapor-liquid configurations were studied: a droplet at the center of a continuous vapor phase and a bubble at the center of a continuous liquid phase. The density field was initialized using the method in Huang et al. (2011). For droplet cases,

$$\rho(x,y) = \frac{\rho_l+\rho_v}{2} - \frac{\rho_l-\rho_v}{2} \times \tanh\left(\frac{2(d-R_o)}{\mathrm{W}}\right) \tag{6.1}$$

and for bubble cases,

$$\rho(x,y) = \frac{\rho_l+\rho_v}{2} + \frac{\rho_l-\rho_v}{2} \times \tanh\left(\frac{2(d-R_o)}{\mathrm{W}}\right) \tag{6.2}$$

where $d = \sqrt{(x - x_0)^2 + (y - y_0)^2}$ for 2D cases and $\sqrt{(x - x_0)^2 + (y - y_0)^2 + (z - z_0)^2}$ for 3D cases. ρ_v and ρ_l are densities of vapor and liquid respectively from Maxwell construction, x_0, y_0 and z_0 are the coordinates of the center of the droplet or bubble, R_o is the initial radius of the droplet or bubble, and W is the initial width of interface which was set to 4. Each simulation was carried out for 100,000 time steps to ensure that steady state was reached. For 2D cases, four computation domains with four different sizes of droplet or bubble were conducted: Case 1 – $L_x = L_y = 100, R_o = 30$; Case 2 – $L_x = L_y = 150, R_o = 40$; Case 3 – $L_x = L_y = 200, R_o = 60$; Case 4 – $L_x = L_y = 350$, $R_o = 100$. For 3D cases, three different sizes of droplet or bubble were investigated: Case 5 – $L_x = L_y = L_z = 100$, $R_o = 30$; Case 6 – $L_x = L_y = L_z = 150$, $R_o = 40$; Case 7 – $L_x = L_y = L_z = 200$, $R_o = 60$. All droplets and bubbles are put in the center of computational domains. Relaxation time $\tau = 1$ for all cases.

Figure 6.1 shows the coexistence curves of droplet cases and bubble cases. It is noted that the numerical stability is worse in 3D droplet cases and the lowest reduced temperature can be investigated is 0.7. In other cases, the lowest reduced temperature can reach 0.5. In droplet cases, both liquid and vapor densities increase with decreasing droplet size and are higher than those in flat-interface cases or from Maxwell construction. In bubble cases, both liquid and vapor densities decrease with decreasing bubble size. The liquid densities are lower than those from Maxwell construction. The vapor densities, however, are lower than those from Maxwell construction at high temperatures and higher than those from Maxwell construction at low temperatures. The insets in Figure 6.1 show an example of the trend of vapor densities with decreasing droplet/bubble size at selected temperatures. This trend also applies at other temperatures. The pressures of liquid and vapor phases in droplet and bubble cases were also obtained and they are plotted in Figure 6.2. In droplet cases, it is observed that the saturation pressures of the vapor phase increase with decreasing droplet size and are slightly higher than those from CS EOS through Maxwell construction. The pressures of the liquid phases also increase with a decreasing droplet size and are significantly higher than predictions of EOS, especially at low temperatures. In bubble cases, the pressures of the vapor phases decrease with decreasing droplet size, and they are lower than predictions of EOS at high temperatures and higher than predictions of EOS at low temperatures. The pressures of the liquid phases decrease with a decreasing droplet size and are much lower than predictions of EOS, especially at low temperatures. Because the changes in the saturation pressures of vapor phase due to interface curvature are quite small compared to the range of pressures studied, the saturation pressures of the vapor phase at chosen temperatures are specially visualized as insets in Figure 6.2. The trends shown in the insets are also observed at other temperatures.

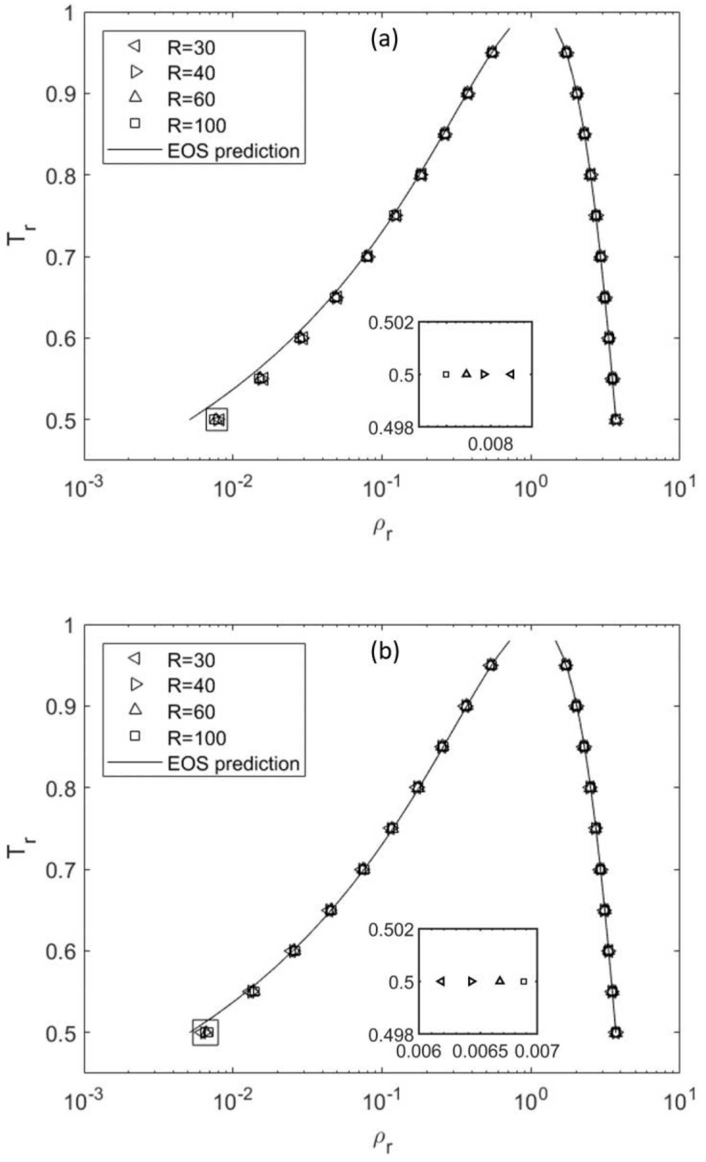

Figure 6.1 Coexistence curves of CS fluids in 2D droplet (a), 2D bubble (b), 3D droplet (c) and 3D bubble cases (d).

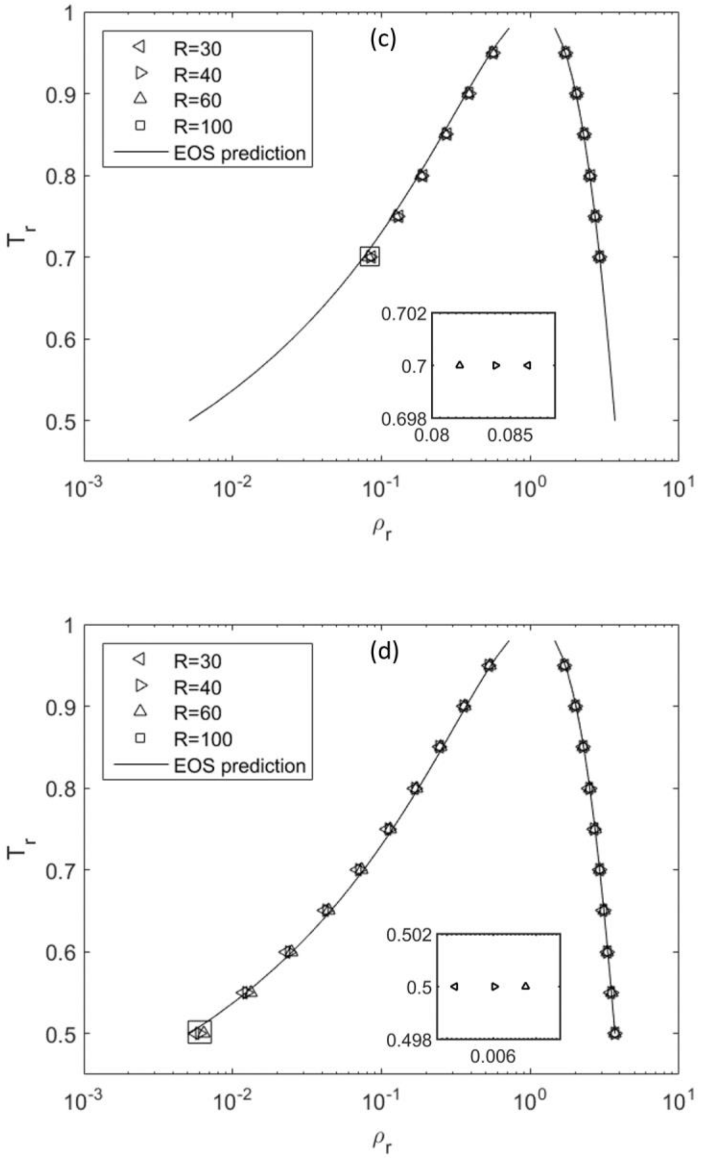

Figure 6.1 Continued.

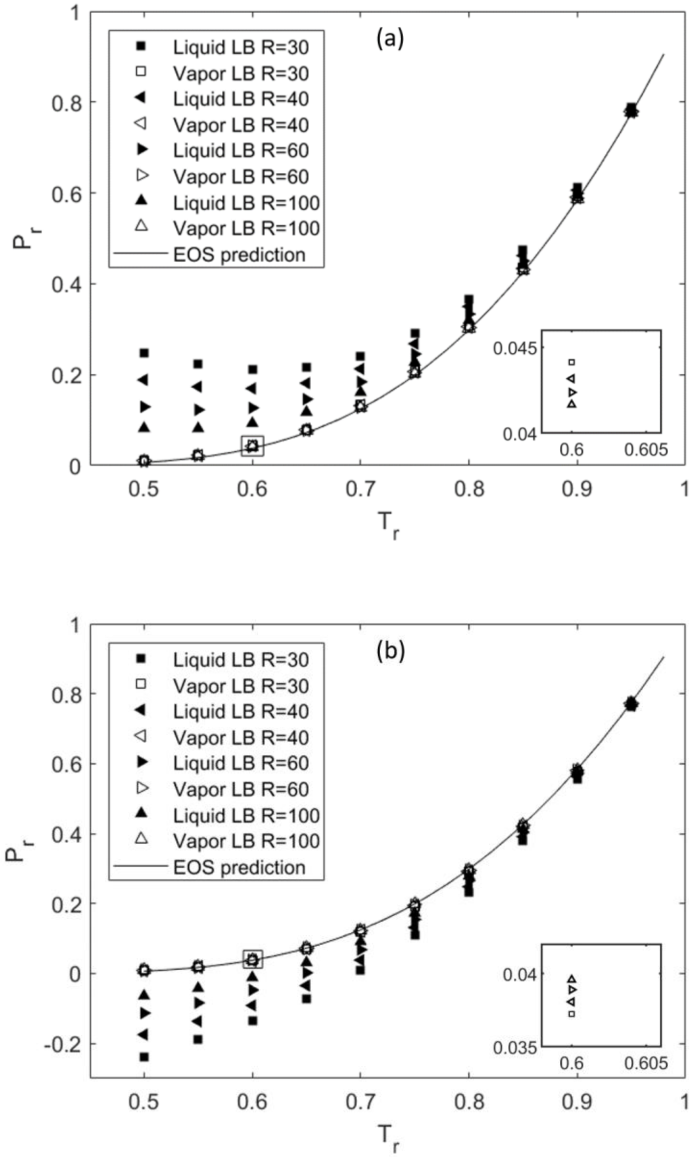

Figure 6.2 Liquid and vapor pressures of CS fluids at different temperatures in 2D droplet (a), 2D bubble (b), 3D droplet (c) and 3D bubble cases (d).

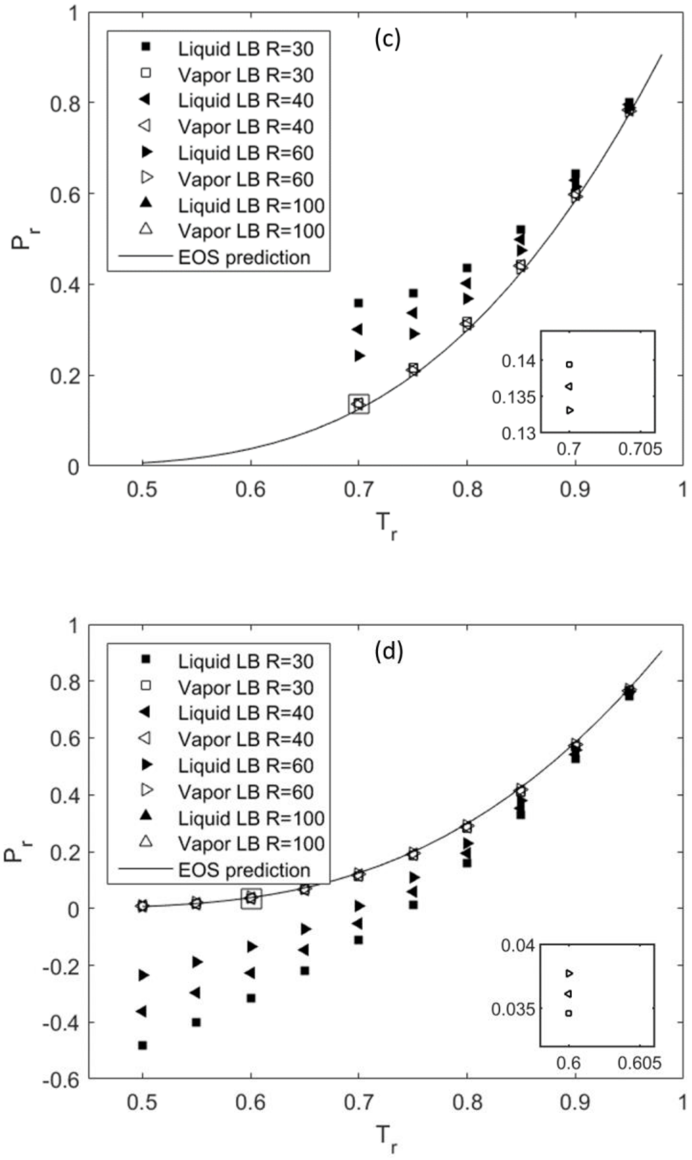

Figure 6.2 Continued.

The pressure difference between vapor and liquid phases across curved interfaces should exhibit the typical behavior of surface tension controlled Laplace pressure: it should increase with decreasing temperature or decreasing droplet (bubble) radius. Figure

6.3 shows pressure differences between vapor and liquid phases as functions of R_o. At three selectively presented temperatures, it is seen that Young-Laplace equation

$$P_{in} - P_{out} = \begin{cases} \frac{\sigma}{R_o}, \ 2D \\ \frac{2\sigma}{R_o}, \ 3D \end{cases} \tag{6.3}$$

is satisfied. σ is the interfacial tension, P_{in} is the pressure inside a droplet (bubble) and P_{out} is the pressure outside a droplet (bubble). Interfacial tensions obtained from Young-Laplace equation at different temperatures are plotted in Figure 6.4. It is seen that interfacial tension decreases with increasing temperature toward zero at the critical point. Theoretically, interfacial tension is an intrinsic property of a fluid, regardless whether a droplet or a bubble is formed. In our simulations, the interfacial tension from 2D and 3D cases are close with difference lower than 0.5%. However, we noted that the pressure differences across bubbles are slightly higher than those across droplets. Interfacial tensions evaluated from bubble tests are thus slightly higher than those from droplet tests, especially when temperature is low. These differences are always very small and they never exceeded 3%.

To further assess the validity of characterized interfacial tensions between the liquid and its saturated vapor, we chose to fit them using the parachor model proposed by Sudgen (1924). The parachor model expresses the interfacial tension of a liquid in equilibrium with its own vapor as a power-law function of the density difference:

$$\sigma^{1/n} = \chi_i(\rho_l - \rho_v) \tag{6.4}$$

where χ_i is the parachor parameter independent of temperature. In Figure 6.5, the simulated $\log(\sigma)$ is plotted as function of $\log(\rho_l - \rho_v)$ and a linear relation is indeed observed with a slope of 3.02. It is worth noting that, although bubble and droplet cases have slightly different interfacial tensions, they fit well to the same parachor model in both 2D and 3D cases.

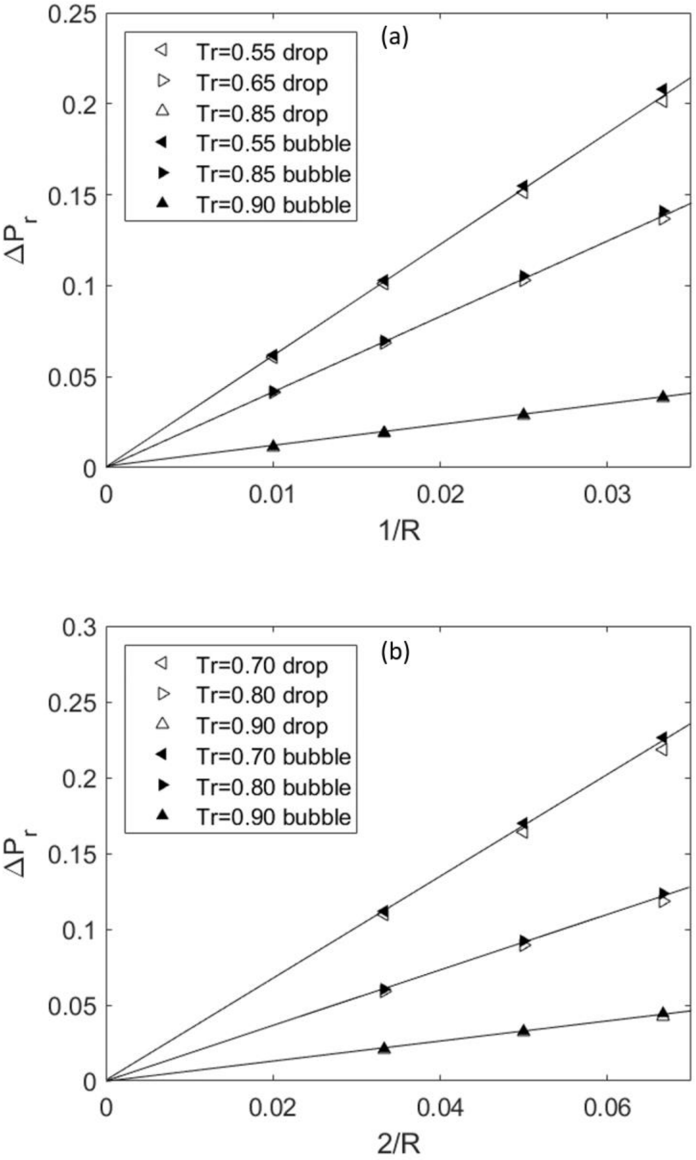

Figure 6.3 Verification of Young-Laplace equation in curved-interface cases. 2D cases are presented in (a) and 3D cases in (b).

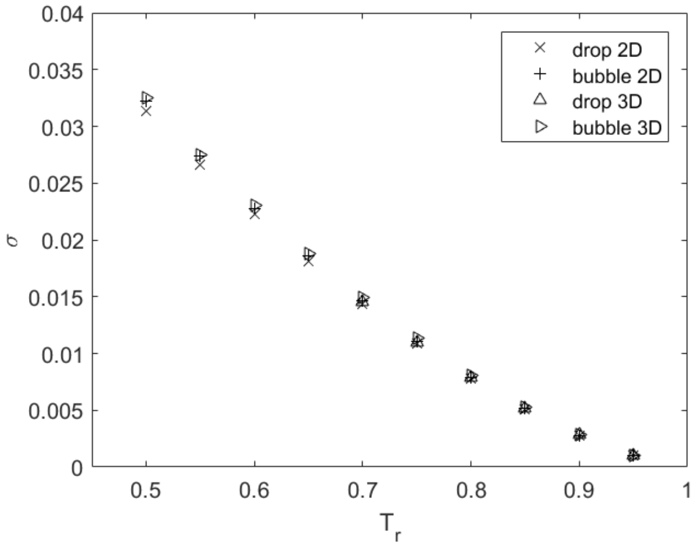

Figure 6.4 Effect of temperature on interfacial tension in curved-interface cases.

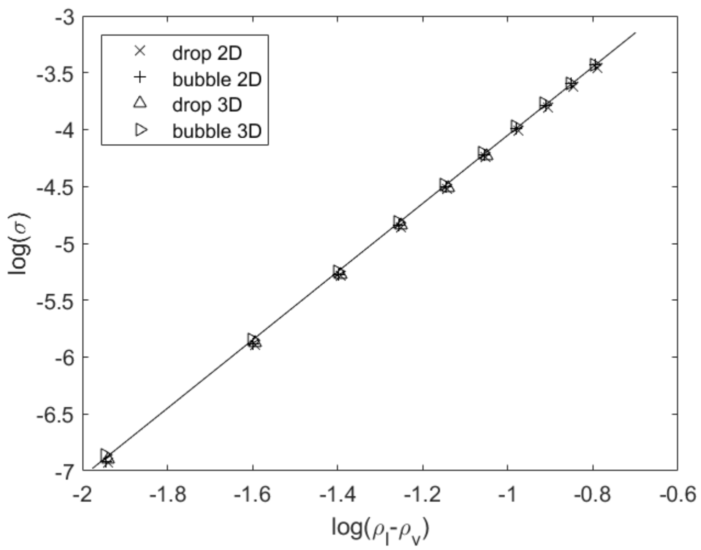

Figure 6.5 Calculated interfacial tension as a function of density difference between liquid and vapor phases.

We now examine the effect of relaxation time on the predictions of LB model for curved-interface cases. Since 2D and 3D cases have close performance, only 2D results are presented. Figure 6.6 shows liquid-vapor density ratios as functions of reduced temperature in curved-interface Case 1 using different relaxation times. Different from flat-interface cases, the effect of relaxation time on density ratios becomes noticeable especially when temperature is low. Close examination of the results shows that relaxation time slightly changes the density of the vapor. The density of liquid on the other hand is not affected by relaxation time. For example, at $T_r = 0.5$, in the droplet case the vapor densities are 0.00868, 0.00824 and 0.00813 when $\tau = 0.75$, 1.0, and 1.5 respectively, and liquid densities are 3.7198. In the bubble case ($T_r = 0.5$), the vapor densities are 0.00641, 0.00618 and 0.00612 when $\tau = 0.75$, 1.0, and 1.5 respectively and liquid densities are 3.6992. Since the effect of relaxation time on vapor density is very small, in our next analysis we will only focus on results obtained with $\tau = 1$.

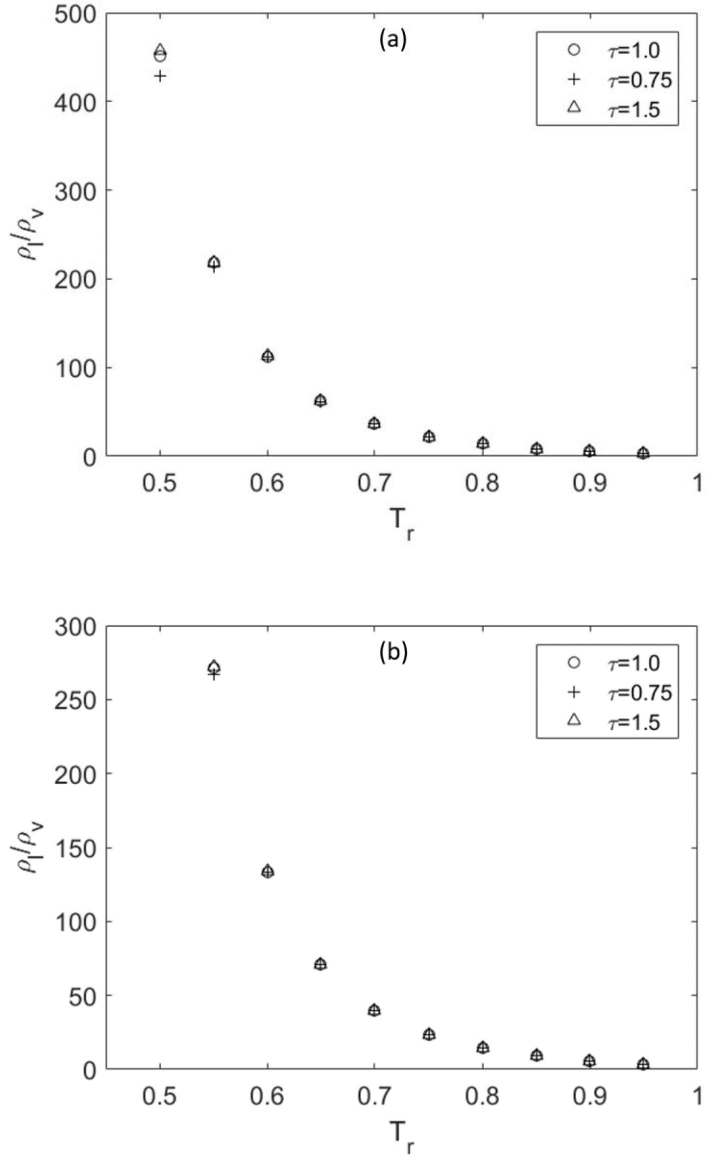

Figure 6.6 Effect of relaxation time on liquid-vapor density ratio when $R_o = 30$ for 2D droplet tests (a) and 2D bubble tests (b).

6.2.2 Consistency with Kelvin equation

In some previous studies (Yuan and Schaefer 2006; Gong and Cheng 2012; Huang et al. 2011), simulated liquid and vapor densities of curved-interface cases were only compared with equilibrium densities from EOS. Our study shows that both liquid / vapor densities and saturation pressures are changed by Laplace pressure. Because equilibrium calculation based on Maxwell construction does not consider the effects of interface curvature and Laplace pressure, Maxwell construction is not a suitable model to evaluate thermodynamic consistency of cases with curved interfaces, especially when temperature is low. We now have demonstrated that the Laplace pressure in LB simulations generated by curved interfaces is inversely proportional to the radius of curvature and therefore obeys Young-Laplace equation, and that the interfacial tension between the two phases decreases as temperature approaches the critical point and follows the parachor model. In what follows, we will apply Kelvin equation (Sir William Thomson 1871), which describes the change in the saturation vapor pressure owning to a curved interface, to evaluate more stringently the results of LB simulations. For a liquid drop surrounded by vapor phase, Kelvin equation predicts that

$$ln\frac{P^{\alpha}}{P_{vp}} = \begin{cases} \frac{v^{\beta}\sigma}{r_0RT}, \ 2D \\ \frac{2v^{\beta}\sigma}{r_0RT}, \ 3D \end{cases} \tag{6.5}$$

For a vapor bubble surrounded by liquid phase, it gives

$$ln\frac{P^{\alpha}}{P_{vp}} = \begin{cases} -\frac{v^{\beta}\sigma}{r_0RT}, \ 2D \\ -\frac{2v^{\beta}\sigma}{r_0RT}, \ 3D \end{cases} \tag{6.6}$$

where P^{α} is the saturation vapor pressure with interface curvature, P_{vp} is the saturation pressure when the interface is flat, v^{β} is molar volume of the liquid phase at equilibrium with the vapor phase when the interface is flat, σ is the interfacial tension, and r_0 is the radius of the drop or bubble.

In Section 6.2.1, we observed that the saturation vapor pressures and vapor / liquid densities of droplet cases increase with decreasing droplet size and saturation vapor pressures and vapor / liquid densities of bubble cases decrease with decreasing bubble size at all temperatures. These trends are qualitatively consistent with Kelvin equation. Saturation vapor pressures calculated using Kelvin equation and those from LB simulations are quantitatively compared in Table 6.1 through Table 6.4. It is seen that saturation vapor pressures from LB simulations agree well with those from Kelvin equation at high temperatures ($T_r \geq 0.7$). As temperature drops, however, deviations between LB simulations and Kelvin equation become more and more significant. This inconsistency caused saturation vapor pressures and vapor densities to be *higher* than those from Maxwell construction conflicting the prediction of Kelvin equation. Maximum deviation in saturation vapor pressure was about 40% at $T_r = 0.5$. Plots of $ln\ (P^\alpha/P_{vp})$ versus $1/r_0$ in Figure 6.7 for the case of $R_o = 30$ show that, although $ln\ (P^\alpha/P_{vp})$ in LB simulations appear to be linear functions of $1/r_0$, the lines deviate from Kelvin equation with a rather significant non-zero intercept when temperature is low.

Table 6.1 Saturation vapor pressures in 2D droplet cases

	R_o = 30			R_o = 40			R_o = 60			R_o = 100		
T_r	P_s^α	P_K^α	Diff.	P_s^α	P_K^α	Diff.	P_s^α	P_K^α	Diff.	P_s^α	P_K^α	Diff.
0.5	0.0106	0.0075	40.8%	0.0102	0.0073	39.7%	0.0099	0.0071	40.6%	0.0096	0.0069	40.1%
0.55	0.0226	0.0192	17.4%	0.0219	0.0187	16.9%	0.0214	0.0183	17.4%	0.0210	0.0179	17.2%
0.6	0.0441	0.0411	7.21%	0.0432	0.0403	7.08%	0.0424	0.0395	7.32%	0.0417	0.0388	7.27%
0.65	0.0795	0.0773	2.88%	0.0782	0.0760	2.87%	0.0770	0.0748	3.04%	0.0760	0.0737	3.08%
0.7	0.1327	0.1315	1.07%	0.1312	0.1298	1.11%	0.1297	0.1281	1.23%	0.1284	0.1267	1.29%
0.75	0.2080	0.2071	0.44%	0.2060	0.2050	0.49%	0.2042	0.2030	0.57%	0.2026	0.2014	0.62%
0.8	0.3080	0.3073	0.24%	0.3059	0.3051	0.27%	0.3038	0.3029	0.31%	0.3021	0.3011	0.33%
0.85	0.4355	0.4344	0.25%	0.4334	0.4324	0.24%	0.4313	0.4302	0.24%	0.4296	0.4286	0.24%
0.9	0.5925	0.5910	0.26%	0.5906	0.5894	0.22%	0.5887	0.5878	0.18%	0.5872	0.5864	0.15%
0.95	0.7805	0.7786	0.25%	0.7793	0.7778	0.19%	0.7780	0.7769	0.14%	0.7770	0.7762	0.10%

P_s^α: Reduced saturation vapor pressure from simulation. P_K^α: Reduced saturation vapor pressure from Kelvin equation.
Diff: $(P_s^\alpha - P_K^\alpha)/P_K^\alpha \times 100\%$

Table 6.2 Saturation vapor pressures in 2D bubble cases

	R_o = 30			R_o = 40			R_o = 60			R_o = 100		
T_r	P_s^α	P_K^α	Diff.	P_s^α	P_K^α	Diff.	P_s^α	P_K^α	Diff.	P_s^α	P_K^α	Diff.
0.5	0.0080	0.0058	37.5%	0.0083	0.0060	38.1%	0.0086	0.0062	38.6%	0.0089	0.0064	39.1%
0.55	0.0181	0.0156	16.5%	0.0186	0.0160	16.7%	0.0192	0.0164	16.8%	0.0196	0.0168	16.9%
0.6	0.0372	0.0347	7.36%	0.0381	0.0355	7.35%	0.0389	0.0362	7.32%	0.0396	0.0369	7.27%
0.65	0.0697	0.0674	3.44%	0.0709	0.0686	3.37%	0.0721	0.0698	3.29%	0.0731	0.0708	3.23%
0.7	0.1201	0.1181	1.72%	0.1217	0.1197	1.63%	0.1233	0.1214	1.55%	0.1245	0.1227	1.47%
0.75	0.1927	0.1909	0.97%	0.1946	0.1929	0.90%	0.1965	0.1949	0.83%	0.1980	0.1965	0.78%
0.8	0.2911	0.2896	0.52%	0.2933	0.2918	0.49%	0.2954	0.2941	0.45%	0.2971	0.2958	0.42%
0.85	0.4185	0.4175	0.24%	0.4206	0.4197	0.24%	0.4228	0.4218	0.24%	0.4245	0.4235	0.24%
0.9	0.5774	0.5775	-0.03%	0.5793	0.5793	0.01%	0.5812	0.5810	0.04%	0.5828	0.5823	0.07%
0.95	0.7703	0.7715	-0.16%	0.7716	0.7724	-0.11%	0.7729	0.7734	-0.06%	0.7739	0.7741	-0.02%

P_s^α: Reduced saturation vapor pressure from simulation. P_K^α: Reduced saturation vapor pressure from Kelvin equation.
Diff: $(P_s^\alpha - P_K^\alpha)/P_K^\alpha \times 100\%$

Table 6.3 Saturation vapor pressures in 3D droplet cases

		R_o = 30			R_o = 40			R_o = 60	
T_r	P_s^α	P_K^α	Diff.	P_s^α	P_K^α	Diff.	P_s^α	P_K^α	Diff.
0.7	0.1394	0.1387	0.50%	0.1363	0.1351	0.94%	0.1331	0.1316	1.12%
0.75	0.2158	0.2156	0.09%	0.2121	0.2115	0.31%	0.2082	0.2071	0.49%
0.8	0.3167	0.3165	0.08%	0.3126	0.3120	0.18%	0.3082	0.3074	0.26%
0.85	0.4444	0.4432	0.27%	0.4401	0.4389	0.27%	0.4357	0.4345	0.26%
0.9	0.6004	0.5979	0.42%	0.5967	0.5946	0.34%	0.5926	0.5911	0.26%
0.95	0.7861	0.7823	0.48%	0.7835	0.7806	0.37%	0.7806	0.7787	0.25%

P_s^α: Reduced saturation vapor pressure from simulation. P_K^α: Reduced saturation vapor pressure from Kelvin equation.
Diff: $(P_s^\alpha - P_K^\alpha)/P_K^\alpha \times 100\%$

Table 6.4 Saturation vapor pressures in 3D bubble cases

		R_o = 30			R_o = 40			R_o = 60	
T_r	P_s^α	P_K^α	Diff.	P_s^α	P_K^α	Diff.	P_s^α	P_K^α	Diff.
0.5	0.0072	0.0051	42.2%	0.0078	0.0054	43.1%	0.0082	0.0058	41.7%
0.55	0.0166	0.0139	19.3%	0.0176	0.0147	19.3%	0.0185	0.0156	19.0%
0.6	0.0346	0.0317	9.11%	0.0361	0.0332	8.91%	0.0377	0.0347	8.70%
0.65	0.0656	0.0627	4.55%	0.0678	0.0650	4.33%	0.0702	0.0674	4.13%
0.7	0.1144	0.1116	2.50%	0.1173	0.1147	2.25%	0.1205	0.1181	2.07%
0.75	0.1854	0.1827	1.47%	0.1891	0.1867	1.29%	0.1930	0.1908	1.13%
0.8	0.2827	0.2805	0.78%	0.2869	0.2849	0.69%	0.2913	0.2896	0.60%
0.85	0.4098	0.4086	0.30%	0.4141	0.4129	0.28%	0.4186	0.4175	0.27%
0.9	0.5695	0.5702	-0.12%	0.5733	0.5737	-0.08%	0.5774	0.5775	-0.01%
0.95	0.7647	0.7674	-0.35%	0.7674	0.7694	-0.26%	0.7703	0.7715	-0.15%

P_s^α: Reduced saturation vapor pressure from simulation. P_K^α: Reduced saturation vapor pressure from Kelvin equation.
Diff: $(P_s^\alpha - P_K^\alpha)/P_K^\alpha \times 100\%$

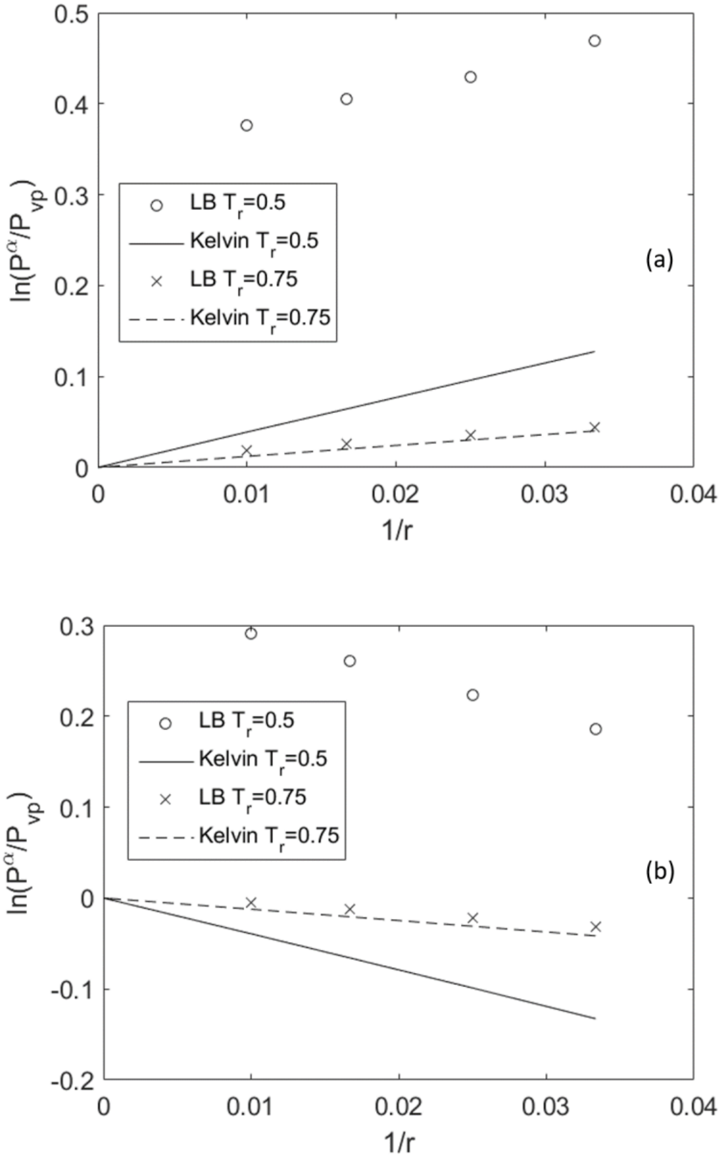

Figure 6.7 Comparison with theoretical (Kelvin equation) plot of $ln\ (P^{\alpha}/P_{vp})$ versus $1/r$ with simulated results, in 2D droplet (a), 2D bubble (b), 3D droplet (c) and 3D bubble cases (d).

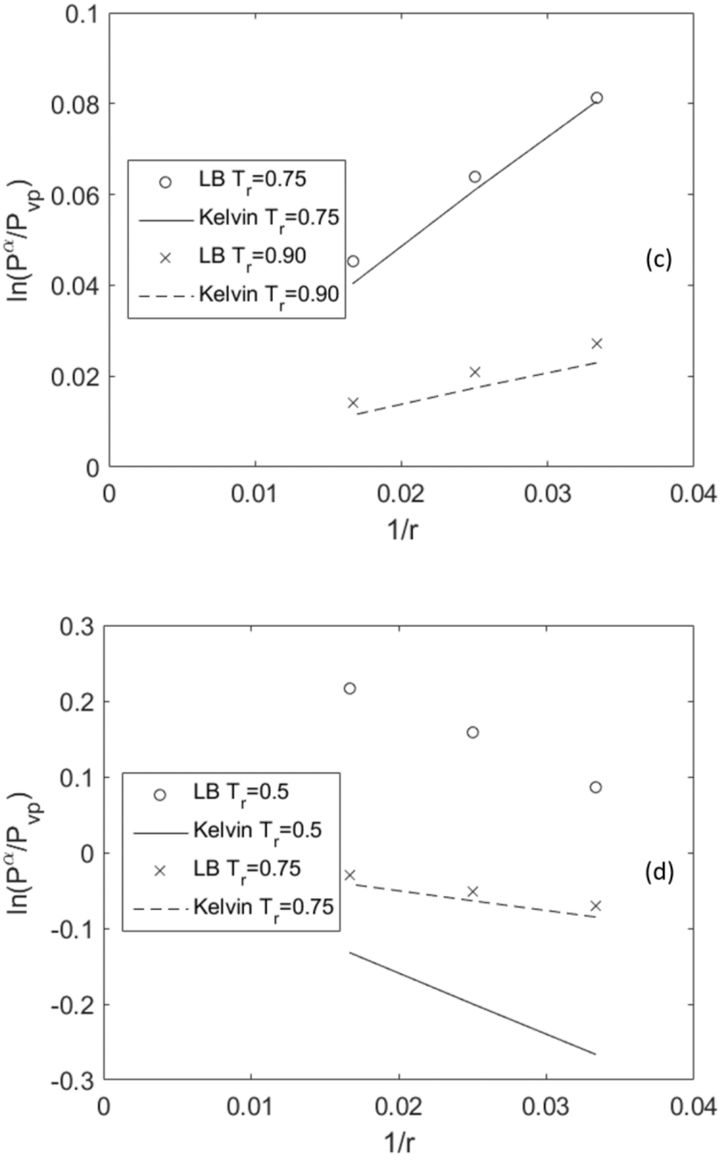

Figure 6.7 Continued.

It is known that pseudo-potential LB models can suffer from thermodynamic inconsistency and vapor density may deviate from theoretical predictions when temperature is low and liquid-vapor density ratio is large (Hu et al. 2015). In flat-interface cases, we have shown that the inaccuracy in vapor density (pressure) can be suppressed by tuning parameter β. So far in the curved-interface cases, we have kept $\beta = 1.22$, a value obtained from flat-interface cases that leads to thermodynamic consistency. We find that by tuning β, better agreement with Kelvin equation can be reached. As shown in Figure 6.8, by setting $\beta = 1.183$ in 2D cases and $\beta = 1.187$ in 3D cases, simulated vapor pressures became much closer to those from Kelvin equation when $T_r = 0.5$. Clearly, the behavior of the saturation vapor pressure in this LB model when interface possesses curvature is only consistent with Kelvin equation when β is properly tuned.

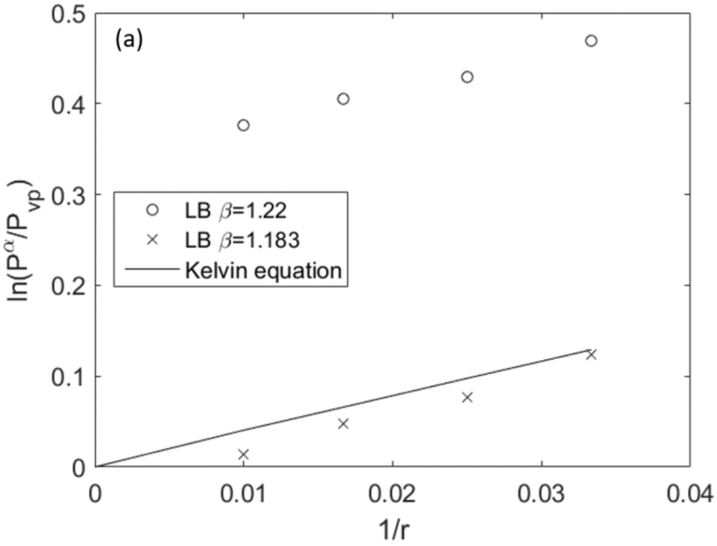

Figure 6.8 Effect of tuning parameter $\boldsymbol{\beta}$ on saturation vapor pressures ($\boldsymbol{T_r = 0.5}$), in 2D droplet (a), 2D bubble (b), and 3D bubble cases (c).

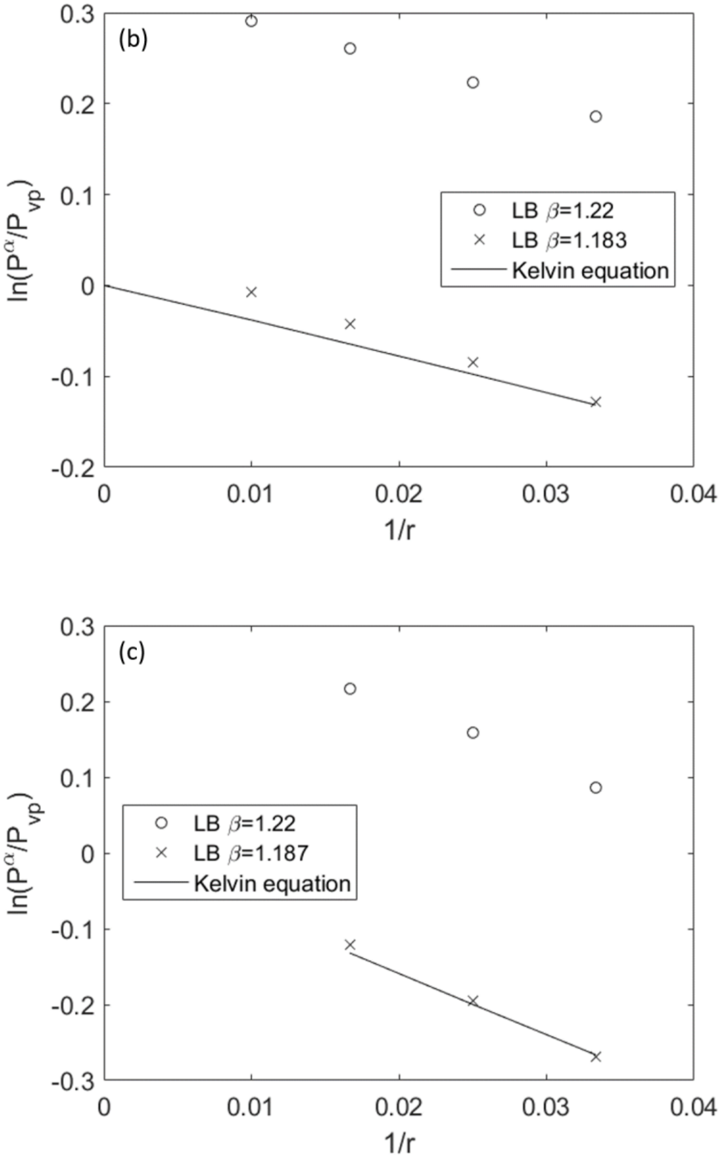

Figure 6.8 Continued.

To better understand the role of β, we examined cases with flat *but inclined* interfaces. We note that flat interfaces studied in Section 5.3 are all aligned with a primary lattice direction (x) as in many previous works (Huang et al. 2011; Hu et al. 2015). To obtain a flat but inclined interface, a *modified* periodic boundary condition needs to be applied. Take the periodic boundary condition in the x direction as an example. The neighbor of lattice node $(1, y)$ in the direction of $(-1, 0)$ was set to $(L_x, y + L_x \tan\theta)$, and the neighbor of lattice (L_x, y) node in the direction of $(1, 0)$ was set to $(1, y - L_x \tan\theta)$. θ is the angle of inclination between the interface and the x direction. When $\theta = 0^{\mathrm{o}}$, this periodic boundary condition reduces to the ordinary one. As shown in Figure 6.9, a case with a flat but inclined interface with $\theta = 45^{\mathrm{o}}$ was simulated. Similar to Section A, the computation domain is $L_x \times L_y = 20 \times 200$. The central region between the lines $y = x + 50$ and $y = x + 150$ was initialized with liquid whereas the rest was initialized with vapor. The density field was initialized by

$$\rho(y) = \rho_v + \frac{\rho_l - \rho_v}{2} \times abs\left(\tanh\left(\frac{2(y-x-50)}{\mathrm{W}}\right) - \tanh\left(\frac{2(y-x-150)}{\mathrm{W}}\right)\right) \tag{6.7}$$

We first set $\beta = 1.22$. The coexistence curves of this inclined-interface case ($\theta = 45^{\mathrm{o}}$) and the case in Section 6.2.1 ($\theta = 0$) are compared to those from Maxwell construction in Figure 6.10. It is observed that vapor densities in the case of $\theta = 45^{\mathrm{o}}$ are larger than those from EOS when temperature is low. To match the results from Maxwell construction, a different value of β is needed in the inclined-interface case. As shown in Figure 6.10, more accurate vapor densities can be obtained when β is tuned to 1.17. This result demonstrates that the vapor density (pressure) is affected by the orientation and thus isotropy of the grid and the effect becomes more significant at lower temperatures as the thickness of interface is reduced. A bubble / drop has a circular (2D) or spherical (3D) interface that samples all orientations and thus Kelvin equation was not well recovered with β established from flat-interface cases.

Figure 6.9 Liquid-vapor equilibrium with a flat but inclined interface ($\theta = 45^o$); Red: liquid phase; Blue: vapor phase.

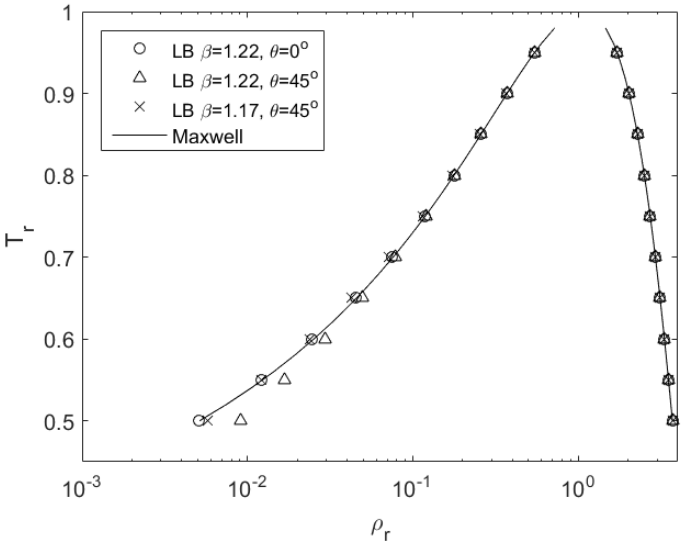

Figure 6.10 Coexistence curve of CS fluid separated by flat (0°) and flat-but-inclined (45°) interfaces.

6.2.3 Intrinsic length scale of pseudo-potential LB model

Pseudo-potential lattice Boltzmann models have been widely applied to simulate multiphase equilibriums and flows. In most such applications, however, whether the lattice spacing is tied to an actual length scale or not is a largely unaddressed question. In many phase behavior studies (Gong and Cheng 2012; Huang et al. 2011; Li et al. 2013), focus was set on equilibrium conditions and length scale was simply not discussed. In simulations of multiphase flows in real systems such as microfluidics and porous media, length scale is often introduced into simulations by using a certain number of lattices to resolve a characteristic length of a real system; this number can be arbitrarily chosen without providing any quantitative procedure (Liu et al. 2016; Kang and Yun 2018; Yu et al. 2007). When flow is single-phase or multiphase but interfacial properties are not important, such a practice could be acceptable. However, when simulating multiphase problems where the properties of interface are critical, a connection between lattice spacing and interface properties is needed.

Kikkinides (2008) studied thermodynamic consistencies of several LB models based on He et al. (1998) and Lee and Fischer (2006). They found that only when the lattice spacing is on the order of a few molecular diameters that the examined LB models can correctly predict bulk and interfacial thermodynamic properties. Siebert et al. (2014) studied coexistence curves using a higher-order LB model. A term, interface geometric resolution, which is defined as the ratio between interface thickness and Cartesian distance between two contiguous sites, was evaluated. It was found that this resolution affected numerically stability and thermodynamic consistency of their model. Although the above work investigated effect of lattice spacing, it is still not clear how lattice size and interface thickness relate to real length scales when using a multiphase LB model. In Sections 6.2.1 and 6.2.2, we showed that the behaviors of pseudo-potential fluids with interface curvature are consistent with Young-Laplace and Kelvin equations at higher temperatures or after β is tuned. This suggests us that similarity principle applied to the interfacial tension can be used to obtain the length scale of lattice spacing in a pseudo-potential LB model from its thermodynamically consistent interfacial properties. Specifically, a length scale in real unit, λ_{REAL}, and a length scale in lattice spacing, λ_{LB}, are considered equal if they generate the same dimensionless interfacial tension $\sigma/(\lambda P_c)$.

Take water as an example. In real units, the critical properties of water are $\mathrm{T}_{c,water} = 647.096\ K,\ \mathrm{P}_{c,water} = 22060\ kPa$. In the pseudopotential LB model with CS EOS, the critical properties are $T_{c,LB} = 0.0943,\ P_{c,LB} = 0.00442$ for any fluid when a = 1, b = 4 and R = 1. When λ_{LB} is selected to be Δx the lattice spacing, dimensionless relation

$$\frac{\sigma_W(T_r)/\lambda_1}{\mathrm{P}_{c,w}} = \frac{\sigma_{LB}(T_r)/\Delta x}{P_{c,LB}} \tag{6.8}$$

should give the *intrinsic* length scale λ_1 in real units that is equivalent to Δx. In Eqn. (6.8), σ_w is the interfacial tension of water in real units and σ_{LB} is the interfacial tension of the LB fluid. In Figure 6.11, the interfacial tension of water in real units (NIST Standard Reference Database Number 69) are plotted as a function of T_r. λ_1 calculated using Eqn. (6.8) at different temperatures and is also shown in Figure 6.11. It can be observed that the intrinsic length scale of the lattice spacing in this pseudo-potential model increases with increasing temperature and ranges from 0.43 nm to 1.09 nm. The droplet radii studied in this work, which are 30, 40, 60, and 100 in lattice units, therefore correspond to real dimensions of tens of nanometers.

The validity of these estimated intrinsic length scale λ_1 corresponding to Δx of the LB model can be verified by comparing the thickness of vapor-liquid interfaces of water in real units with that from LB simulations after the interface thickness in LB units are converted to real units. This comparison is shown in Figure 6.12. The simulated interface thickness of water using the pseudo-potential model is compared with those from experiments (Kinosita and Yokota 1965) and molecular dynamics (MD) simulations (Vins et al. 2016). In the range of temperature studied ($T_r \geq 0.5$), LB simulations have correctly captured the trend that interface thickness should increase with increasing temperature. Compared to molecular dynamics simulations, the interface of water from LB simulation is clearly much thicker. The interface thickness from experiment, though only available at relative low temperatures, is closer to the results from LB if its trend continues to higher temperatures. Two-phase lattice Boltzmann methods are often criticized for that the diffusive interfaces of LB are much thicker than real interfaces. This study, by comparing the interface thickness (equals to or greater than 5 lattices) of pseudo-potential LB to that measured from experiments and MD, we show that if the lattice resolution of pseudo-potential LB is established on the order of a few angstroms on the basis of thermodynamic consistency of the interfacial tension, thickness of the diffusive interface generated from LB may be regarded as real.

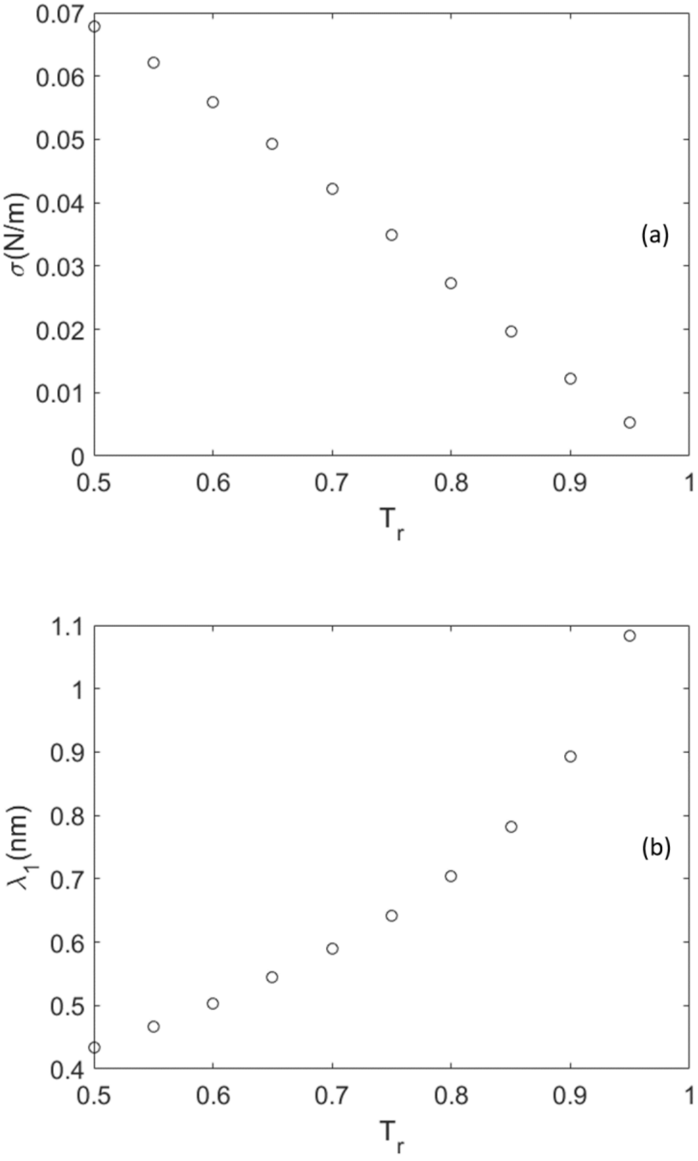

Figure 6.11 (a) Experimental measured interfacial tension of water (NIST Standard Reference Database Number 69) and (b) intrinsic length of pseudo-potential LB model (b) as a function of reduced temperature T_r.

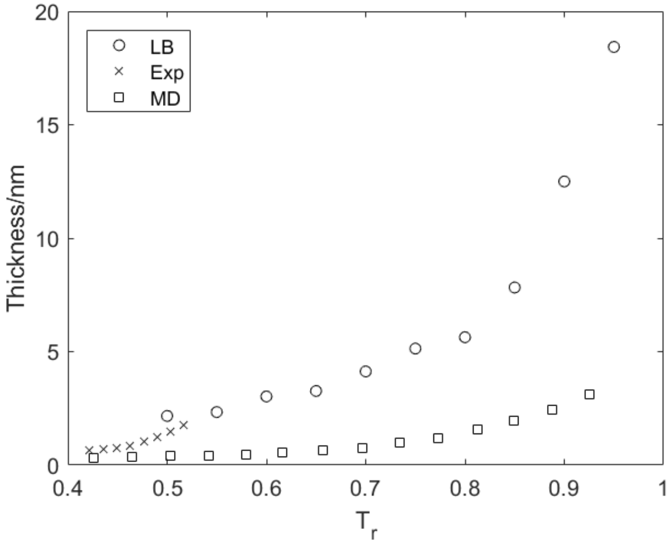

Figure 6.12 Temperature dependence of interface thickness of water from experiments (Kinosita and Yokota 1965), MD simulations (Vins et al. 2016), and LB simulations (this study).

Using this procedure, the intrinsic length scales of this pseudo-potential LB when simulating other fluids can also be obtained. Figure 6.13 shows the interfacial tensions of methane, ethane, carbon dioxide and nitrogen in real units (NIST Standard Reference Database Number 69) and the calculated intrinsic length scales of LB. They all show trends similar to those in Figure 6.11: intrinsic length scale of LB increases with increasing temperature and it is on the order of a few angstroms.

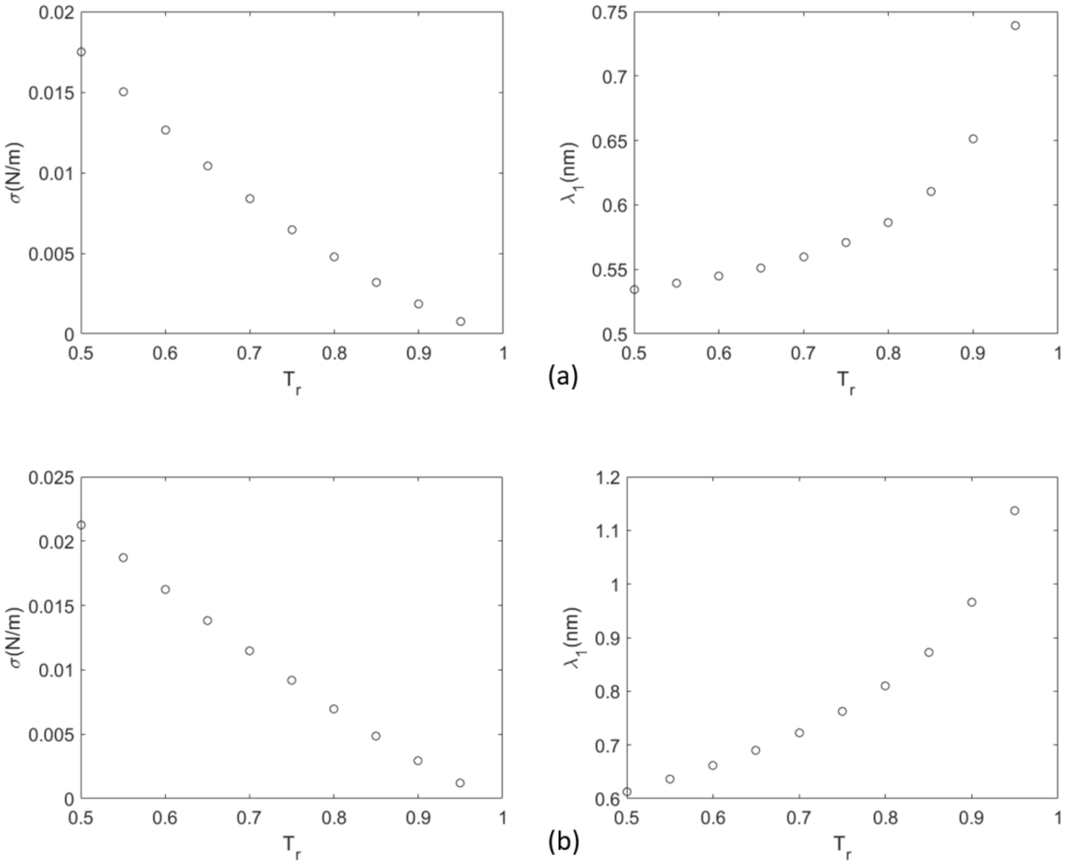

Figure 6.13 Experimentally measured interfacial tensions (left) (NIST Standard Reference Database Number 69) and intrinsic lengths of pseudo-potential LB model as a function of reduced temperature T_r for methane (a), ethane (b), carbon dioxide (c) and nitrogen (d).

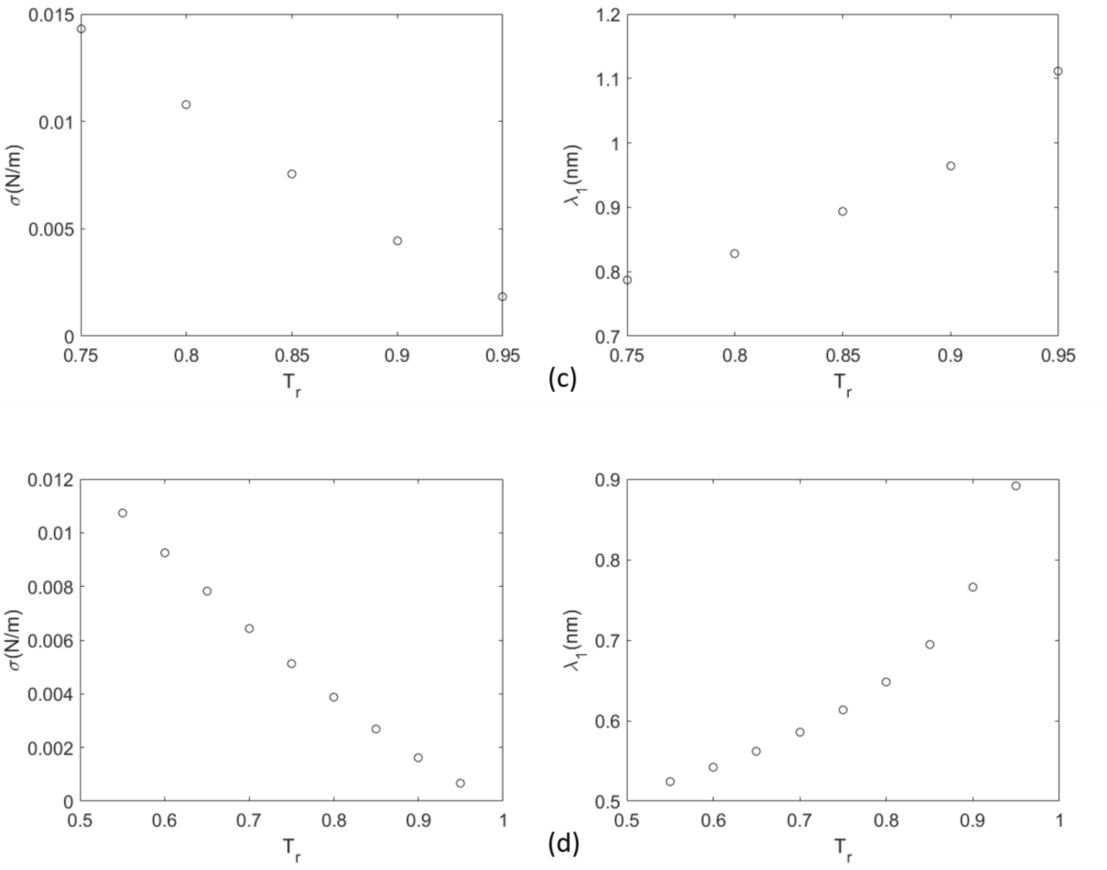

Figure 6.13 Continued.

6.3 Conclusions and Discussions

In the present Chapter we investigated the thermodynamic consistency of pseudo-potential lattice Boltzmann models under effect of interface curvature. When interface is curved, equilibrium densities and saturation pressures obtained from simulations cannot be directly compared to Maxwell construction and EOS due to the effect of Laplace pressure. Evaluation of thermodynamic consistency thus used two steps. In the first step, we found that pseudo-potential model used in this study generated interfacial tensions that are consistent with Young-Laplace equation and these interfacial tensions can be well described by the parachor model. Equilibrium densities, however, are slightly influenced by relaxation time in curved-interface cases especially at low temperatures. In the second step, the change in saturation vapor pressure caused by curved interface was quantitatively compared to the predictions of Kelvin equation. It is found that the behavior of the saturation vapor pressure is consistent with predictions of Kelvin equation at high temperatures. Deviations, however, were noted at low temperatures. These deviations can be reduced when β is tuned. The need for tuning β appears to be associated with the orientations of a curved interface. We observed that β is tied to the orientation of the interface relative to the primary lattice directions. For instance, β needs to be tuned to 1.17 when simulating an inclined interface with 45° of inclination. The obvious shift in the phase equilibrium due to interface curvature needs to be carefully considered when one applies LB to nanoscale problems.

Results obtained from non-dimensionalizing the interfacial tension suggests that pseudo-potential model is simulating fluids at nanoscale naturally. The length scales of lattice spacing of pseudo-potential model can be determined quantitatively for different fluids. Results show that these length scales changes with temperature and are on the order of angstroms. To check the validity of these calculated length scales, interface thicknesses in pseudo-potential model, after converted to real units using the calculated length scale, were measured and compared with thicknesses from experiments and molecular dynamics simulations. Interface thicknesses from LB simulation are thicker than those from molecular dynamics but are close to experimental results. This work shows that the pseudo-potential LB models can be tuned to describe phase equilibrium with Laplace pressure. They may be particularly suitable for nano-scale applications, because lattice spacing from non-dimensionalizing the interfacial tension is on the order of angstroms, which is the typical length scale of inter-molecular interactions.

Our procedure for evaluating thermodynamic consistency in the presence of interface curvature was applied to a free energy lattice Boltzmann model (Swift et al. 1995). Findings from the free energy model are consistent with those from the pseudopotential model. Saturation vapor pressures from free energy model were approximately in line with Kelvin equation at high temperatures. At low temperatures, deviations that are larger compared with pseudopotential model were observed. These deviations are likely caused by lack of accuracy in predicting saturation vapor densities and low interface thickness. Intrinsic length scales of the free energy model were slightly higher than those of the pseudopotential model but derived thicknesses in real units were very close. Results from the free energy model can be found in the Appendix B.

CHAPTER VII

CONCLUSIONS AND FUTURE WORK

7.1 Conclusions

In this work, we implemented both reservoir-scale and pore-scale approaches to model unconventional reservoirs. In the reservoir scale, a multi-porosity model is used to distinguish different kind of pores in shale matrix and embedded discrete fracture model is applied to describe fractures. The prediction of shale formations is conducted by using an unstructured compositional simulator which enable us considering multi-physics in different continua. Besides, the lattice Boltzmann model is used to study the phase equilibrium at nanoscale. A multiphase lattice Boltzmann model is extended to incorporate equation of state based on pore-scale simulator originally designed for multiphase flow. The pore-scale study serves as a fundamental tool to study the physics in nanopores. The knowledge learned from pore-scale study can be applied to the reservoir-scale simulation. The main conclusions made in this work can be summarized as below:

Pore size distribution in shale reservoir can be modeled by subdividing the shale matrix into multiple continua based on experimental pore size data. Compositional simulations show lower pressure decline, lower oil and gas production can be observed when considering pore size distribution in matrix. The existence of small pore reduces both oil and gas recovery due to their low permeability. Also, lighter residual oil is found in smaller pores. Besides, oil production is decreased when capillary pressure is considered, especially in one continuum case. Gas production are also suppressed with capillary pressure in all cases. Considering pore size distribution allows different kinds of fluids at the same location and the complex flow properties and phase behaviors in different kind of nanopores can be captured.

Mixed-wettability in shale can be characterized by dividing shale matrix into organic matter and inorganic matter which are oil-wet and water-wet respectively. Water-oil relative permeability and oil-gas relative permeability can be calculated separately for different matters. The water-oil relative permeability can be obtained by simulating two-phase flow directly on digital rock samples. Oil-gas relative permeability is extracted from oil-gas capillary pressure curve. In mixed-wet shale reservoir, we found that the rich hydrocarbon in organic matrix is hard to be produced due to its low flow conductivity to hydraulic fractures. A higher TOC in shale matrix leads to lower production rates at early stage but a higher production at later stage. The relative permeability in inorganic matrix, which is affected by wettability, is a dominant factor that controls the overall production rates in mixed-wet shale.

The potential of CO_2 injection into shale reservoir has been comprehensively evaluated for both enhanced gas recovery and permeant CO_2 sequestration. The dispersed distribution of kerogen is modeled by assigning organic matter as a sphere embedded inside inorganic matter. Simulation results show that CO_2 flooding is not preferred for enhanced gas recovery or CO_2 storage due to the low CO_2 sweeping efficiency and CO_2 huff-n-puff has a better performance. The nature of dispersed distribution of kerogen in shale matrix decreases the efficiency of CO_2 injection because the injected CO_2 will easily bypass the kerogen where competitive adsorption could happen.

The lattice Boltzmann model incorporated with equation of state is presented and validated by comparing with results from Maxwell construction and equation of state. The thermodynamic consistency of pseudo-potential model can be achieved when interface is flat. When interface is curved, it is found that pseudo-potential model generated interfacial tensions that are consistent with Young-Laplace equation and these interfacial tensions can be well described by the parachor model. The change in saturation vapor pressure caused by curved interface can be quantitatively analyzed by using Kelvin equation. Results obtained from non-dimensionalizing the interfacial tension suggests that pseudo-potential model is simulating fluids at nanoscale naturally. The length scales of pseudo-potential model change with temperature and are on the order of angstroms. Interface thicknesses in pseudo-potential model, after converted to real units using the calculated length scale, are reasonable by comparing with thicknesses from experiments and molecular dynamics simulations.

7.2 Future work

With the work presented in this study, we would like to provide recommendations for future work:

(1) Injection of CO_2 as well as other gases such as produced gas into shale oil reservoir for enhanced oil recovery can be studied.

(2) The current pseudo-potential model can be extended to model phase equilibrium of multicomponent mixtures by flowing the idea of mixing rules in flash calculation

(3) By incorporating fluid-solid interaction into pseudo-potential model. The adsorption of shale gas in nanopores and real digital rocks can be simulated.

(4) The phase equilibrium in nanopores under both effect of capillary pressure and force between solid-fluid interaction can be characterized.

REFERENCES

Aguilera, R. 2014. Flow Units: From Conventional to Tight Gas to Tight Oil to Shale Oil Reservoirs. *SPE Res Eval & Eng* 17 (2): 190-208. SPE-165360-PA. SPE-165360-PA.

Akkutlu, I.Y., Fathi, E. 2012. Multiscale gas transport in shales with local Kerogen heterogeneities SPE J 17:1002–1011.

Alharthy, N., Teklu, T., Kazemi, H., Graves, R., Hawthorne, S., Braunberger, J., Kurtoglu, B. 2018. Enhanced oil recovery in liquid-rich shale reservoirs: laboratory to field. SPE Reservoir Evaluation & Engineering 21(1): 137-159.

Alizadeh, A.H., Piri, M. 2014. The effect of saturation history on three-phase relative permeability: An experimental study, Water Resource Research 50: 1636–1664.

Ambrose, R.J., Hartman, R.C., Akkutlu, I.Y. 2011. Multi-component sorbed phase considerations for Shale Gas-in-place Calculations. Presented at SPE Production and Operations Symposium, 27-29 March, Oklahoma City, Oklahoma, USA. SPE-141416-MS.

Ambrose, R.J., Hartman, R.C., Diaz-Campos, M., Akkutlu, I.Y., Sondergeld, C.H. 2012. Shale gas-in-place calculations part I: new pore-scale considerations. SPE J 17(01): 219–229.

Arora, V., Cai, Y. 2014. US natural gas exports and their global impacts. Appl Energy 120: 95–103.

Baker, L.E. 1988. Three-Phase Relative Permeability Correlations. Paper presented at SPE Enhanced Oil Recovery Symposium, 16-21 April, Tulsa, Oklahoma.

Basquet, R., Bourbiaux, B.J., and Cohen, C.E. 2005. Fracture Flow Property Identification: An Optimized Implementation of Discrete Fracture Network Models. Presented at SPE Middle East Oil and Gas Show and Conference, 12-15 March, Kingdom of Bahrain.

Cahn, J.W., Hilliard, J.E., 1958. Free energy of a nonuniform system. I. Interfacial free energy. J. Chem. Phys. 28, 258.

Cahn, J.W., Hilliard, J.E., 1959. Free energy of a nonuniform system III. Nucleation in a two-component incompressible fluid. J. Chem. Phys. 31, 688.

Cantisano, M.T., Restrepo, D.P., Cespedes, S., Toelke, J., Grader, A., Suhrer, M., Walls, J. 2013. Relative Permeability in a Shale Formation in Colombia Using Digital Rock Physics. Paper URTEC-1562626 presented at the Unconventional Resources Technology Conference held in Denver, Colorado, USA, 12-14 August 2013.

Chai, Z., Yan, B., Killough, J.E., and Wang, Y. 2018a. An efficient method for fractured shale reservoir history matching: The embedded discrete fracture multi-continuum approach. J. Pet. Sci. Eng. 160: 170-181.

Chai, Z., Tang, H., He, Y., Killough, J.E., Wang, Y., 2018b. Uncertainty Quantification of the Fracture Network with a Novel Fractured Reservoir Forward Model. Presented at SPE Annual Technical Conference and Exhibition, 24-26 September, Dallas, Texas, USA. SPE-191395-MS.

Chen, L., Kang, Q., Mu, Y., He, Y., Tao, W. 2014. A critical review of the pseudopotential multiphase lattice Boltzmann model: Methods and applications. International Journal of Heat and Mass Transfer 76, 210-236.

Chen, T.Y., Feng, X., Pan, Z. 2015. Experimental study of swelling of organic rich shale in methane. Int. J. Coal. Geol. 150: 64–73.

Civan, F. 2010. Effective Correlation of Apparent Gas Permeability in Tight Porous Media. Transp Porous Med 82: 375.

Civan, F., Rai, C.S., Sondergeld, C.H. 2011. Shale-gas permeability and diffusivity inferred by improved formulation of relevant retention and transport mechanisms. Transp. Porous Media 86(3): 925–944.

Clarkson, C.R., Solano, N., Bustin, R.M., Bustin, A.M.M., Chalmers, G.R.L., He, L., Melnichenko, Y.B., RadliÅski, A.P., Blach T.P. 2013. Pore structure characterization of north american shale gas reservoirs using usans/sans, gas adsorption, and mercury intrusion. Fuel 103: 606-616.

Corey, A.T., Rathjens, C.H., Henderson, J.H., Wyllie, M.R.J. 1956. Three-Phase Relative Permeability. J. Pet. Tech. 8: 63-65.

Danesh, A.S., Dandekar, A.Y., Todd, A.C., Sarkar, R. 1991. A Modified Scaling Law and Parachor Method Approach for Improved Prediction of Interfacial Tension of Gas-Condensate Systems. Paper presented at the SPE Annual Technical Conference and Exhibition, Dallas. Society of Petroleum Engineers 1991.

Demianov, A., Dinariev, O., Evseev, N. 2011. Density functional modelling in multiphase compositional hydrodynamics. Can J Chem Eng 89, 206–226.

Dong, H., Blunt, M.J. 2009. Pore-network extraction from micro-computerized-tomography images. Physical Review E 80, 036307.

Du, F., Ma, H., Gu, Y. 2019. Three different periods of CO2 dissolution into a light crude oil. The Canadian Journal of Chemical Engineering 97 (1): 330-343.

Du, F., Nojabaei, B. 2019a. A Review of Gas Injection in Shale Reservoirs: Enhanced Oil/Gas Recovery Approaches and Greenhouse Gas Control. Energies 12(12): 2355.

Du, F., Nojabaei, B., and Johns, R.T. 2018. A Black-Oil Approach to Model Produced Gas Injection for Enhanced Recovery of Conventional and Unconventional Reservoirs. Presented at SPE Annual Technical Conference and Exhibition, 24-26 September, Dallas, Texas, USA. SPE-191454-MS.

Du, F., Nojabaei, B. 2019b. Estimating diffusion coefficients of shale oil, gas, and condensate with nano-confinement effect. Paper presented in Society of Petroleum Engineers Eastern Regional Meeting, 15−17 October, Charleston, West Virginia, USA. SPE-MS-196589; 2019.

d'Humières, D. 2002. Multiple–relaxation–time lattice Boltzmann models in three dimensions. Philosophical Transactions of the Royal Society of London. Series A: Mathematical, Physical and Engineering Sciences 360; 437-451.

Eleri, O.O., Graue, A., Skauge, A., Larsen J.A. 1995. Calculation of three-phase relative permeabilities from displacement experiments with measurements of in-situ saturation, paper SCA 9509 presented at the International Symposium of the Society of Core Analysts, San Francisco, California, 12–14 Sept.

Eshkalak, M.O., Al-Shalabi, E.W., Sanael, A., Aybar, U., Sepehrnoori, K. 2014. Enhanced gas recovery by CO_2 storage versus re-fracturing treatment in unconventional shale gas reservoirs. Presented at the Abu Dhabi International Petroleum Exhibition and Conference, Abu Dhabi, UAE, 10–13 November. SPE-172083-MS; 2014.

Fassihi, M.R., Potter, G.F. 2009. Analysis of transient data during relative permeability measurements using steady-state technique, paper SPE-123676-MS presented at SPE Annual Technical Conference and Exhibition, Society of Petroleum Engineers, New Orleans, La.,4–7 Oct.

Fathi, E., Akkutlu, I.Y. 2014. Multi-component gas transport and adsorption effects during CO2 injection and enhanced shale gas recovery. Int J Coal Geol 123:52–61.

Godec, M., Koperna, G., Petrusak, R., Oudinot, A. 2013. Potential for enhanced gas recovery and CO_2 storage in the Marcellus shale in the Eastern United States. Int J Coal Geol 118: 95–104.

Godec, M., Koperna, G., Petrusak, R., Oudinot, A. 2014. Enhanced Gas Recovery and CO_2 Storage in Gas Shales: A Summary Review of its Status and Potential. Energy Procedia 63: 5849-5857.

Gong, S., Cheng, P. 2012. Numerical investigation of droplet motion and coalescence by an improved lattice Boltzmann model for phase transitions and multiphase flows, Comput. Fluids 53, 93–104.

Gunstensen, A.K., Rothman, D.H., Zaleski, S., Zanetti, G. 1991. Lattice Boltzmann model of immiscible fluids. Physical Review A 43, 4320.

Gunstensen, A.K., Rothman, D.H. 1993. Lattice-Boltzmann studies of immiscible two-phase flow through porous media. Journal of Geophysical Research: Solid Earth 98, 6431-6441.

Guo, Z., Zheng C., Shi, B. 2002. Discrete lattice effects on the forcing term in the lattice Boltzmann method, Phys. Rev. E 65 (4) 046308.

He, X., Shan X., Doolen, G.D. 1998. Discrete Boltzmann equation model for nonideal gases, Phys. Rev. E 57 (1) R13–R16.

Hinkley, R., Gu, Z., Wong, T., Camilleri, D., 2013. Multi-porosity Simulation of Unconventional Reservoirs. Society of Petroleum Engineers. Presented at SPE Unconventional Resources Conference Canada, 5-7 November, Calgary, Alberta, Canada. SPE-167146-MS.

Hu, A., Li, L., Uddin R. 2015. Force method in a pseudo-potential lattice Boltzmann method. Journal of Computational Physics 294, 78-89.

Huang, H., Krafczyk M., Lu, X. 2011. Forcing term in single-phase and Shan–Chen type multiphase lattice Boltzmann models, Phys. Rev. E 84 (4) 046710.

Huang, J., Jin, T., Chai, Z., Barrufet, M., Killough, J.E. 2019a. Compositional simulation of fractured shale reservoir with distribution of nanopores using coupled multi-porosity and EDFM method. Journal of Petroleum Science and Engineering 179: 1078-1089.

Huang, J., Xiao, F., Dong, H., Yin, X. 2019b. Diffusion tortuosity in complex porous media from pore-scale numerical simulations. Computers & Fluids 183: 66-74.

Huang, J., Jin, T., Chai, Z., Barrufet, M., Killough, J. 2020. Compositional simulation of three-phase flow in mixed shale oil reservoir. Fuel 260,116361.

Huang, J., Xiao, F., Yin, X. 2017. Lattice Boltzmann simulation of pressure-driven two-phase flows in capillary tube and porous medium. Computers & Fluids 155: 134-145.

Jackson, M.D., Valvatne, P.H., Blunt, M.J. 2003. Prediction of wettability variation and its impact on flow using pore- to reservoir-scale simulations. Journal of Petroleum Science and Engineering 39: 231–246.

Javadpour, F. 2009. Nanopores and Apparent Permeability of Gas Flow in Mudrocks (Shales and Siltstone). J Can Pet Technol 48 (8): 16-21.

Jerauld, G.R., Rathmell, J.J. 1997. Wettability and relative permeability of Prudhoe Bay: A case study in mixed-wet reservoirs. SPE Reservoir Eng. 12(1): 58–65.

Jia, B., Tsau, J.S., Barati, R. 2019. A review of the current progress of CO2 injection EOR and carbon storage in shale oil reservoirs. Fuel 236: 404-427.

Jiang, J., Younis, R.M. 2016. Compositional modeling of enhanced hydrocarbons recovery for fractured shale gas-condensate reservoirs with the effects of capillary pressure and multicomponent mechanisms. Journal of Natural Gas Science and Engineering 34: 1262-1275.

Jimenez, BA. L., Hernandez G., Czenia, B, Killough, J.E., and Barrufet, M.A, 2018. Effects of Thermodynamic and Rock Properties on the Performance of Liquids-Rich Nano-Porous Shale Reservoirs. Presented at SPE Argentina Exploration and Production of Unconventional Resources Symposium, 14-16 August, Neuquen, Argentina. SPE-191813-MS.

Jin, L., Hawthorne, S., Sorensen, J., Pekot, L., Kurz, B., Smith, S., Heebink, L., Herdegen, V., Bosshart, N., Torres, J., Dalkhaa, C., Peterson, K., Gorecki, C., Steadman, E., Harju, J. 2017. Advancing CO_2 enhanced oil recovery and storage in unconventional oil play—Experimental studies on Bakken shales. Appl Energy 208: 171–183.

Jin, X., Wang, X., Yan, W., Meng, S., Liu, X., Jiao, H., Su, L., Zhu, R., Liu, H., Li, J. 2019. Exploration and casting of large scale microscopic pathways for shale using electrodeposition. Appl Energy 247: 32-39.

Kalantari-Dahaghi, A. 2010. Numerical simulation and modeling of enhanced gas recovery and CO_2 storage in shale gas reservoirs: a feasibility study. Presented at the SPE international conference on CO_2 capture, storage, and utilization, New Orleans, Louisiana, 10–12 November. SPE-139701-MS; 2010.

Kalarakis, A.N., Burganos, V.N., Payatakes, A.C. 2002. Galilean-invariant lattice-Boltzmann simulation of liquid-vapor interface dynamics. Physical Review E 65: 056702.

Kalarakis, A.N., Burganos, V.N., and Payatakes, A.C. 2003. Three-dimensional lattice-Boltzmann model of van der Waals fluids. Physical Review E 67: 016702.

Kang, D.H., Yun, T.S. 2018. Minimized capillary end effect during CO2 displacement in 2-D micromodel by manipulating capillary pressure at the outlet boundary in Lattice Boltzmann method. Water Resources Research, 54, 895-915.

Kang, S.M., Fathi, E., Ambrose, R.J., Akkutlu, I.Y., Sigal, R.F. 2011. Carbon dioxide storage capacity of organic-rich shales. SPE J 16(4): 842−855.

Karimi-Fard, M., Durlofsky, L.J., Aziz, K., 2004. An Efficient Discrete-fracture Model Applicable for General-purpose Reservoir Simulators. SPE J. 9 (02): 227-236.

Khajepor, S., Wen, John., Chen, B. 2015. Multipseudopotential interaction: A solution for thermodynamic inconsistency in pseudopotential lattice Boltzmann models. Physical Review E 91, 023301.

Kianinejad, A., Chen, X., DiCarlo, D.A. 2015. The effect of saturation path on three-phase relative permeability. Water Resource Research 51: 9141-9164.

Kikkinides, E.S. 2008. Thermodynamic consistency of liquid-gas lattice Boltzmann methods: Interfacial property issues. Physical Review E 78, 036702.

Kim, T.H., Cho, J., Lee, K.S. 2017. Evaluation of CO_2 injection in shale gas reservoirs with multi-component transport and geomechanical effects. Appl Energy 190: 1195–1206.

Kinosita, K., and Yokota, H. 1965. Temperature dependence of the optical surface thickness of water. J. Phys. Soc. Japan 20, 1086.

Kuila, U., and Prasad, M. 2013. Specific surface area and pore‐size distribution in clays and shales. Geophysical Prospecting 61: 341-362.

Kupershtokh, A.L., Medvedev, D.A., Karpov, D.I. 2009. On equations of state in a lattice Boltzmann method. Comput. Math. Appl. 58 (5) 965–974.

Land, C.S. 1968. Calculation of Imbibition Relative Permeability for Two- and Three-Phase Flow from Rock Properties. Soc. Pet. Eng. J. 8: 149-156.

Landry, C.J. Karpyn, Z.T. Ayala, O. 2014. Relative permeability of homogenous-wet and mixed-wet porous media as determined by pore-scale lattice Boltzmann modeling. Water Resource Research 50: 3672- 3689.

Latva-Kokko, M., Rothman, D.H. 2005. Diffusion properties of gradient-based lattice

Boltzmann models of immiscible fluids. Phys. Rev. E 71, 056702.

Lee, S.H., Jensen, C.L., Lough, M.F., 2000. Efficient Finite-difference Model for Flow in a Reservoir with Multiple Length-scale Fractures. SPE J. 5 (03): 268-275.

Lee, T., Fischer, P.F. 2006. Eliminating parasitic currents in the lattice Boltzmann equation method for nonideal gases. Phys. Rev. E 74, 046709.

Li, H., Pan, C., Miller, C.T. 2005. Pore scale investigation of viscous coupling effects for two-phase flow in porous media. Phys Rev E 72, 026705.

Li, L., Lee, S.H., 2008. Efficient Field-scale Simulation of Black Oil in a Naturally Fractured Reservoir through Discrete Fracture Networks and Homogenized Media. SPE J. 11 (04): 750-758.

Li, L. and Sheng, J.J. 2017. Nanopores Confinement Effects on Phase Behavior and Capillary Pressure in a Wolfcamp Shale Reservoir. *J. Taiwan Inst. Chem. Eng*. 78: 317-328.

Li, Q., Luo, K.H., Li, X.J. 2012. Forcing scheme in pseudopotential lattice Boltzmann model for multiphase flows, Phys. Rev. E 86 (1) 016709.

Li, Q., Luo, K.H., and Li, X.J. 2013. Lattice Boltzmann modeling of multiphase flows at large density ratio with an improved pseudopotential model. Physical Review E 87, 053301.

Liu, F., Ellett, K., Xiao, Y., Rupp, J.A. 2013. Assessing the feasibility of CO_2 storage in the New Albany Shale (Devonian-Mississippian) with potential enhanced gas recovery using reservoir simulation. Int J Greenhouse Gas Control 17: 111–126.

Liu, H., Valocchi, A.J., Kang, Q. 2012. Three-dimensional lattice Boltzmann model for immiscible two-phase flow simulations. Phys. Rev E 85, 046309.

Liu H., Kang, Q., Leonard C.R., Schmieschek, S., Narvaez, A., Jones, B., Williams, J. R., Valocchi, A.J., Harting, J. 2016. Multiphase lattice Boltzmann simulations for porous media applications. Comput Geosci 20:777–805.

Lohrenz, J., Bray, B.G., and Clark, C.R. 1964. Calculating viscosities of Reservoir Fluids from their Compositions. Journal of Petroleum Technology 16(10). SPE-915-PA.

Lu, Y., Ao, X., Tang, J., Jia, Y., Zhang, X., Chen, Y. 2016. Swelling of shale in supercritical carbon dioxide. J. Nat. Gas Sci. Eng. 30: 268–275.

Luo, F., Xu, R.N., J, P.X. 2013. Numerical investigation of the influence of vertical permeability heterogeneity in stratified formation and of injection/production well perforation placement on CO2 geological storage with enhanced CH4 recovery. Appl Energy 102: 1314–1323.

Luo, L.-S. 1998. Unified theory of lattice Boltzmann models for non-ideal gases, Phys. Rev. Lett. 81 (8) 1618–1621.

Middleton, R.S., Gupta, R., Hyman, J.D., Viswanathan, H.S. 2017. The shale gas revolution: Barriers, sustainability, and emerging opportunities. Appl Energy 199: 88–95.

Moinfar, A., Varavei, A., Sepehrnoori, K., Johns, R.T., 2014. Development of an Efficient Embedded Discrete Fracture Model for 3D Compositional Reservoir Simulation in Fractured Reservoirs. SPE J. 19 (02): 750-758.

Naar, J., Wygal, R.J. 1961. Three-Phase Imbibition Relative Permeability. Soc. Pet. Eng. J. 1: 254-258.

Nakornthap, K. and Evans, R.D. 1986. Temperature-Dependent Relative Permeability and Its Effect on Oil Displacement by Thermal Methods. SPE Reservoir Engineering 1(3): 230-242.

NIST Standard Reference Database Number 69.

Nojabaei B., Johns, R.T., Chu, L. 2013. Effect of Capillary Pressure on Phase Behavior in Tight Rocks and Shales. SPE Res Eval & Eng 16 (3): 281-289. SPE-159258-PA.

Nuttall, B.C. 2010. Reassessment of CO_2 storage capacity and enhanced gas recovery potential of middle and upper devonian black shales in the appalachian basin. In: MRCSP Phase II Topical Report, 2005 October–2010 October. Kentucky Geological Survey, Lexington, Kentucky.

Nuttall, B.C., Eble, C.F., Drahovzal, J.A., Bustin, R.M. 2005. Analysis of Devonian black shales in kentucky for potential carbon dioxide storage and enhanced natural gas production. Report Kentucky Geological Survey/University of Kentucky (DE-FC26-02NT41442).

Olorode, O.M., Akkutlu, I.Y., Efendiev, Y. 2017. Compositional reservoir-flow simulation for organic rich gas shale. SPE J, 22(06): 1963–1983.

Pan, C., Hilpert, M., Miller, C.T. 2004. Lattice-Boltzmann simulation of two-phase flow in porous media. Water Resource Research 40, W01501.

Pan, Y., Hui, D., Luo, P., Zhang, Y., Sun, L., Wang, K. 2018. Experimental investigation of the geochemical interactions between supercritical CO_2 and shale: implications for CO2 storage in gas-bearing shale formations. Energy & Fuels 32 (2): 1963−1978.

Péneloux, A., Rauzy, E., and Fréze, R. 1982. A consistent correction for Redlich-Kwong-Soave Volumes. Fluid Phase Equilib 8(1): 7-23.

Piri, M., Blunt, M.J. 2005. Three-dimensional mixed-wet random pore-scale network modeling of two-and three-phase flow in porous media. I. model description, Phys. Rev. E 71(2), 026301.

Piri, M., Blunt, M.J. 2005. Three-dimensional mixed-wet random pore-scale network modeling of two-and three-phase flow in porous media. II. Results, Phys. Rev. E 71(2), 026302.

Pommer, M., and Milliken, K. 2015. Pore types and pore-size distributions across thermal maturity, Eagle Ford Formation, southern Texas. AAPG Bulletin, 99(9): 1713-1744.

Qian, Y.H., d'Humières D., Lallemand, P. 1992. Lattice BGK models for Navier-Stokes equation. Europhys Lett, 17: 479-484.

Rachford, H.H., and Rice, J.D. 1952. Procedure for Use of Electronic Digital Computers in Calculating Flash Vaporization Hydrocarbon Equilibrium. *Journal of Petroleum* Technology 4(10). SPE-952327-G.

Sandve, T.H., Berre, I., Nordbotten, J.M., 2012. An efficient multi-point flux approximation method for Discrete Fracture-Matrix simulations. *J. Comput. Phys*. 231(9), 3784-3800.

Saraf, D.N. Fatt, I. 1967. Three-Phase Relative Permeability Measurement Using a Nuclear Magnetic Resonance Technique for Estimating Fluid Saturation. Soc. Pet. Eng. J. 7:235-242.

Sarda, S., Jeannin, L., Basquet, R., Bourbiaux, B., 2002. Hydraulic Characterization of Fractured Reservoirs: Simulation on Discrete Fracture Models. *SPE J*. 5 (02): 154-162.

Sarem, A.M. 1966. Three-Phase Relative Permeability Measurements by Unsteady-State Method. Soc. Pet. Eng. J. 6: 199-205.

Sbragaglia, M., Benzi, R., Biferale, L, Succi, S., Sugiyama, K., Toschi, F. 2007. Generalized lattice Boltzmann method with multirange pseudopotential, Phys. Rev. E 75 (2) 026702.

Sbragalia, M., and Shan, X. 2011. Consistent pseudopotential interactions in lattice

Boltzmann models. Physical Review E 84, 036703.

Schepers, K.C., Nuttall, B., Oudinot, A.Y., Gonzalez, R. 2009. Reservoir modeling and simulation of the Devonian gas shale of Eastern Kentucky for enhanced gas recovery and CO_2 storage. Presented at the SPE international conference on CO_2 capture, storage, and utilization, San Diego, California, 2–4 November. SPE-126620-MS; 2009.

Shah, M., Shah, S., Sircar, A. 2017. A comprehensive overview on recent developments in refracturing technique for shale gas reservoirs. Journal of Natural Gas Science and Engineering 46: 350–364.

Shahverdi, H., Sohrabi, M., Fatemi, S.M., Jamiolahmady, M., Ireland, S., Rabertson, G. 2011. Evaluation of three-phase relative permeability models for WAG injection using water-wet and mixed-wet core flood experiments, paper SPE-143030-MS presented at SPEEUROPEC/EAGE Annual Conference and Exhibition, Society of Petroleum Engineers, Vienna, Austria, 23–26 May, 2011.

Shan, X., Chen, H. 1993. Lattice Boltzmann model for simulating flows with multiple phases and components. Physical Review E 47, 1815.

Shan, X., Chen, H. 1994. Simulation of nonideal gases and liquid-gas phase transitions by the lattice Boltzmann equation. Physical Review E 49, 2941.

Shan, X., Doolen, G. 1995. Multicomponent lattice-Boltzmann model with interparticle interaction. Journal of Statistical Physics 81, 379-393.

Shan, X. 2006. Analysis and reduction of the spurious current in a class of multiphase lattice Boltzmann models, Phys. Rev. E 73 (4) 047701.

Shan, X. 2008. Pressure tensor calculation in a class of nonideal gas lattice Boltzmann models. Physical Review E 77, 066702.

Shi, Y., Tang, G.H., Xia, H.H. 2015. Investigation of coalescence-induced droplet jumping on superhydrophobic surfaces and liquid condensate adhesion on slit and plain fins. International journal of heat and mass transfer 88, 445-455.

Siebert, D.N., Philippi, P.C., Mattila, K.K. 2014. Consistent lattice Boltzmann equations for phase transitions. Physical Review E 90, 053310.

Sir William Thomson F.R.S. 1871. LX. On the equilibrium of vapour at a curved surface of liquid. The London, Edinburgh, and Dublin Philosophical Magazine and Journal of Science, 42:282, 448-452.

Siripatrachai, N., Ertekin, T., and Johns, R.T. 2017. Compositional simulation of Hydraulically fractured tight formation considering the effect of Capillary Pressure on Phase Behavior. SPE J. 22 (04): 1046-1063.

Skauge, A., and Larsen, J.A. 1994. Three-phase relative permeabilities and trapped gas measurements related to WAG processes, paper SCA 9421 presented Proceedings of the International Symposium of the Society of Core Analysts, Stavanger, Norway.

Spiteri, E.J., Juanes, R., Blunt, M.J., Orr, F.M. 2008. A new model of trapping and relative permeability hysteresis for all wettability characteristics. SPE J. 13(3): 277–288.

Stimpson, B.C. and Barrufet, M.A. 2016. Thermodynamic Modeling of Pure Components Including the Effects of Capillarity. J. Chem. Eng. Data, 2016, 61 (8): 2844-2850.

Stimpson, B., Barrufet, M. 2017. Constructing Oil/Gas Capillary Pressure and Relative Permeability Curves from a Distribution of Pores in Shale Reservoirs. Paper URTEC-2670123-MS Presented at SPE/AAPG/SEG Unconventional Resources Technology Conference, 24-26 July, Austin, Texas, USA, 2017.

Stone, H.L. 1970. Probability Model for Estimating Three-Phase Relative Permeability. J. Pet. Tech. 22: 214-218.

Stone H.L. 1973. Estimation of Three-Phase Relative Permeability and Residual Oil Data. J. Can. Pet. Tech. 12(4): 53-61

Sudgen., S. 1924. The variation of surface tension with temperature and some related functions. J. Chem. Soc., 25, 32-41.

Sun, J., Schechter, D., 2015. Optimization-based Unstructured Meshing Algorithms for Simulation of Hydraulically and Naturally Fractured Reservoirs with Variable Distribution of Fracture Aperture, Spacing, Length, and Strike. Presented at SPE Annual Technical Conference and Exhibition, 27-29 October, Amsterdam, The Netherlands. SPE-170703-MS.

Swift, M.R., Osborn, W.R., Yeomans, J.M. 1995. Lattice Boltzmann simulation of nonideal fluids. Physical Review Letters 75, 830.

Tang, H., Hasan, A.R., and Killough, J.E. 2018. Development and Application of a Fully Implicitly Coupled Wellbore/Reservoir Simulator To Characterize the Transient Liquid Loading in Horizontal Gas Wells. SPE J. 23 (05): 1615-1629.

Tarokh, A., Mohamad, A. A. Jiang, L. 2013. Simulation of conjugate heat transfer using the lattice Boltzmann method, Numerical Heat Transfer, Part A: Applications, 63:3, 159-178.

Tölke, J., Krafczyk, M., Schulz, M., Rank, E. 2002. Lattice Boltzmann simulations of binary fluid flow through porous media. Trans. R. Soc. London 360, 535.

Travalloni, L., Castier, M., Tavares, F.W. 2014. Phase Equilibrium of Fluids Confined in Porous media from an extended Peng-Robinson Equation of State. *Fluid Phase* Equilib 362: 335-341.

Urban, E., Orozco, D., Fragoso, A., Selvan, K., Aguilera, R. 2016. Refracturing Vs. Infill Drilling - A Cost Effective Approach to Enhancing Recovery in Shale Reservoirs. Presented at SPE/AAPG/SEG Unconventional Resources Technology Conference, 1-3 August, San Antonio, Texas, USA. URTEC-2461604-MS; 2016.

Vermylen, J.P. 2011. Geomechanical studies of the Barnett shale, Texas, USA. Ph.D. Thesis. Stanford, California: Stanford University.

Vins, V., Celny, D., Plankova, B., Nemec, T., Duska, M., Hruby J. 2016. Molecular Simulations of the Vapor–Liquid Phase Interfaces of Pure Water Modeled with the SPC/E and the TIP4P/2005 Molecular Models. EPJ Web of Conference 114, 02136, 2016.

Wagner, A.J. 2006. Thermodynamic consistency of liquid-gas lattice Boltzmann simulations. Physical Review E 74, 056703.

Wagner, A.J., and Pooley A.J. 2007. Interface width and bulk stability: Requirements for the simulation of deeply quenched liquid-gas systems. Physical Review E 76, 045702(R).

Wang, L., Yu, W. 2019. Mechanistic simulation study of gas Puff and Huff process for Bakken tight oil fractured reservoir. Fuel 239: 1179–1193.

Warren, J.E., Root, P.J., 1963. The Behavior of Naturally Fractured Reservoirs. *SPE J.* 3 (03): 245-255.

Wasaki, A., Akkutlu. I.Y. 2015. Permeability of organic-rich shale. SPE J 20(6): 1384–1396.

Weijermars, R. 2014. US shale gas production outlook based on well roll-out rate scenarios. Appl Energy 124: 283–297.

Weinaug C.F. and Katz D.L. 1943. Surface Tensions of Methane-Propane Mixtures. Ind. Eng. Chem. 35(2): 239-246.

Wu, M., Ding, M., Yao, J., Li, C., Li, X., Zhu, J. 2019. Development of a multi-continuum quadruple porosity model to estimate CO_2 storage capacity and CO_2 enhanced shale gas recovery. Journal of Petroleum Science and Engineering 178: 964–974.

Wu, M., Xiao, F., Johnson-Paben, R.M., Retterer, S.T., Yin, X., Neeves, K.B. 2012. Single- and two-phase flow in microfluidic porous media analogs based on Voronoi tessellation. Lab Chip 12, 253-261.

Xiao, F., Yin, X. 2016. Geometry models of porous media based on Voronoi tessellations and their porosity–permeability relations. Computers & Mathematics with Applications 72(2): 328-348.

Yan, B., Alfi, M., An, C., Cao, Y., Wang, Y., Killough, J.E. 2016. General Multi-Porosity simulation for fractured reservoir modeling. Journal of Natural Gas Science and Engineering 33: 777–791.

Yan, B., Alfi, M., Wang. Y., and Killough, J.E. 2013. A New Approach for the Simulation of Fluid Flow in Unconventional Reservoirs through Multiple Permeability Modeling. Presented at SPE Annual Technical Conference and Exhibition, 30 September-2 October, New Orleans, Louisiana, USA. SPE-166173-MS.

Yan, B., Mi, L., Chai, Z., Wang, Y., Killough, J.E. 2018a. An Enhanced Fracture Network model for multiphase flow in fractured reservoirs. Journal of Petroleum Science and Engineering 161: 667-682.

Yan, B., Mi, L., Wang, Y., Tang, H., An, C., and Killough, J.E. 2018b. Multi-porosity multi-physics compositional simulation for gas storage and transport in highly heterogeneous shales. J. Pet. Sci. Eng. 160: 498-509.

Yan, B., Wang, Y., and Killough, J.E. 2016. Beyond dual-porosity modeling for the simulation of complex flow mechanisms in shale reservoirs. Comput Geosci 20: 69.

Yan, B., Wang Y., and Killough, J.E. 2017. A fully compositional model considering the effect of nanopores in tight oil reservoirs. J. Pet. Sci. Eng. 152: 675-682.

Yassin, M.R., Dehghanpour, H., Wood, J., Lan, Q. 2016. A Theory for Relative Permeability of Unconventional Rocks with Dual-Wettability Pore Network. SPE J. 21(6): 1970-1980.

Yu, W., Al-Shalabi, E.W., Sepehrnoori, K. 2014. A sensitivity study of potential CO_2 injection for enhanced gas recovery in Barnett shale reservoirs. Presented at the SPE unconventional resources conference, Woodlands, Texas, 1–3 April. SPE-169012-MS; 2014.

Yu, W., Lashgari, H.R., Wu, K, Sepehrnoori, K. 2015. CO2 injection for enhanced oil recovery in Bakken tight oil reservoirs. Fuel 159: 354-363.

Yu, W., Sepehrnoori K. 2018. Shale Gas and Tight Oil Reservoir Simulation Gulf Professional Publishing. Elsevier.

Yu, Z., Hemminger, O., Fan, L.S. 2007. Experiment and lattice Boltzmann simulation of two-phase gas–liquid flows in microchannels. Chemical Engineering Science 62, 7172–7183.

Yuan, J., Luo, D., Feng, L. 2015. A review of the technical and economic evaluation techniques for shale gas development. Appl Energy 148: 49–65.

Yuan, P., Schaefer, L. 2006. Equations of state in a lattice Boltzmann model, Phys. Fluids 18 (4) 042101–042111.

Yuan, W., Pan, Z., Li, X., Yang, Y., Zhao, C., Connell, L.D., Li, S., He, J. 2014. Experimental study and modeling of methane adsorption and diffusion in shale. Fuel 117: 509−519.

Zarghami, A., Looijie, N., Akker, H. V. d. 2015. Assessment of interaction potential in simulating nonisothermal multiphase systems by means of lattice Boltzmann modeling. Physical Review E 92, 023307.

Zarragoicoechea, G.J., and Kuz, V.A. 2004. Critical Shift of a Confined Fluid in Nanopore. Fluid Phase Equilib 220: 7-9. https://doi.org/10.1016/j.fluid.2004.02.014.

Zhang, D., Papadikis, K., Gu, Sai. 2014. Three-dimensional multi-relaxation time lattice-Boltzmann model for the drop impact on a dry surface at large density ratio. International journal of heat and mass transfer 64, 11-18.

Zhang, J. 2011. Lattice Boltzmann method for microfluidics: models and applications. Microfluid Nanofluid 10, 1-28.

Zhang, J., Tian, F. 2008. A bottom-up approach to non-ideal fluids in the lattice Boltzmann method. EPL, V81, 66005.

Zhang, R., Chen, H. 2003. Lattice Boltzmann method for simulations of liquid-vapor thermal flows. Physical Review E 67, 066711.

Zhao, Y., Fan, L. 2010. Multirelaxation-time interaction-potential-based lattice Boltzmann model for two-phase flow. Phys Rev E 82, 046708.

APPENDIX A

CALCULATION OF FUGACITY COEFFICIENT

Fugacity coefficient of each component in a hydrocarbon mixture is calculated by

$$ln\phi_i = -\ln(Z-B) + (Z-1)\frac{b_i}{b} - \frac{A}{2\sqrt{2}B}[\frac{1}{a}\left(2\sqrt{a_i}\sum_{j=1}^{N_c} x_j\sqrt{a_j}(1-k_{ij})\right)$$

$$-\frac{b_i}{b}]\ln(\frac{Z+(1+\sqrt{2})B}{Z+(1-\sqrt{2})B}) \tag{A.1}$$

where

$$A = aP/(R^2T^2) \tag{A.2}$$

$$B = bP/(RT) \tag{A.3}$$

$$a = \sum_{j=1}^{N_c}\sum_{i=1}^{N_c} x_i x_j (1-k_{ij})\sqrt{a_i a_j} \tag{A.4}$$

$$b = \sum_{i=1}^{N_c} x_i b_i,\ a_i = 0.45724\alpha(T)(RT_{ci})^2/P_{ci} \tag{A.5}$$

$$b_i = 0.07780RT_{ci}/P_{ci} \tag{A.6}$$

$$\alpha(T) = [1 + m_i(1-\sqrt{T/T_{ci}})]^2 \tag{A.7}$$

R is the gas constant, k_{ij} is binary interaction coefficient, T_{ci} and P_{ci} are critical temperature and critical pressure respectively, and

$$m_i = \begin{cases} 0.37464 + 1.54226\omega_i - 0.2699\omega_i^2 & \omega_i < 0.49 \\ 0.379642 + 1.48503\omega_i - 0.164423\omega_i^2 + 0.01167\omega_i^3 & otherwise \end{cases} \tag{A.8}$$

where ω_i is the acentric factor.

APPENDIX B

EVALUATION ON THERMODYNAMIC CONSISTENCY OF FREE-ENERGY LB MODEL

In this appendix, we present additional tests performed to evaluate the thermodynamic consistency of a free-energy (FE) LB fluid with interface curvature. Different from pseudopotential models, FE models simulate vapor-liquid co-existence by implementing a pressure tensor into the equilibrium distribution (Swift et al. 1995). While some studies established co-existence curves using FE LB (Swift et al. 1995; Wagner 2006; Wagner and Pooley 2007) and many used pressure differences across curved interfaces to establish interfacial tensions (Swift et al. 1995; Kalarakis et al. 2002; Kalarakis et al. 2003), no previous study has examined consistency with Kelvin equation. In this evaluation, the classical FE model by Swift et al. (1995) is applied. For brevity, we refer the readers to Swift et al. (1995) for details of the model. To be consistent with tests performed for pseudopotential models, Carnahan-Starling (CS) equation of state was used. All results presented in this appendix were obtained using the D2Q9 velocity model.

The thermodynamic consistency of FE LB fluid with a flat interface was first evaluated. The computational domain and the method used to initialize the phases are the same as those presented in Section 6.2.1. Relaxation time was set as 1. It is known that κ in the FE model affects the interfacial tension, interface thickness and equilibrium densities at phase equilibriums (Swift et al. 1995; Wagner 2006). Thus, coexistence curves obtained using different κ were compared to those from Maxwell construction. Figure B.1

shows that $\kappa = 0.3$ generated the most accurate coexistence curve. Calculated saturation pressures at $\kappa = 0.3$ also matched well with those from Maxwell construction, as indicated by Figure B.2. However, compared to the β-pseudopotential model, which can handle a reduced temperature as low as 0.5, the FE model of Swift et al. (1995) with $\kappa = 0.3$ can only simulate liquid-vapor equilibriums at relatively high temperatures ($T_r \geq 0.82$).

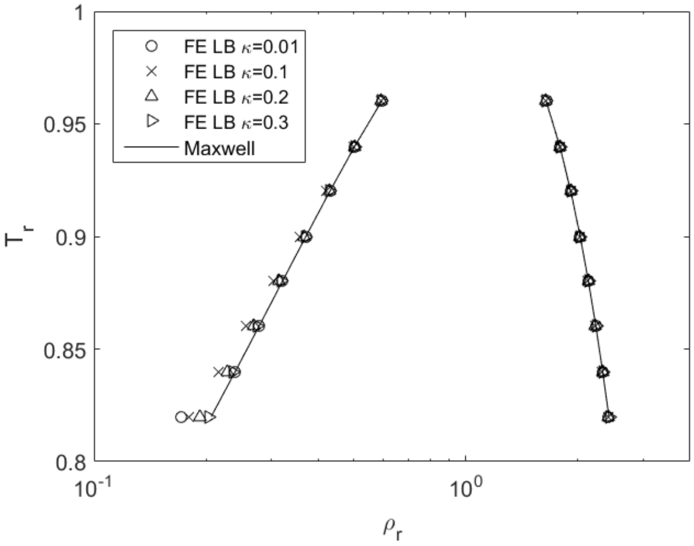

Figure B.1 Coexistence curve of CS fluid with a flat interface using the FE model of Swift et al. (1995).

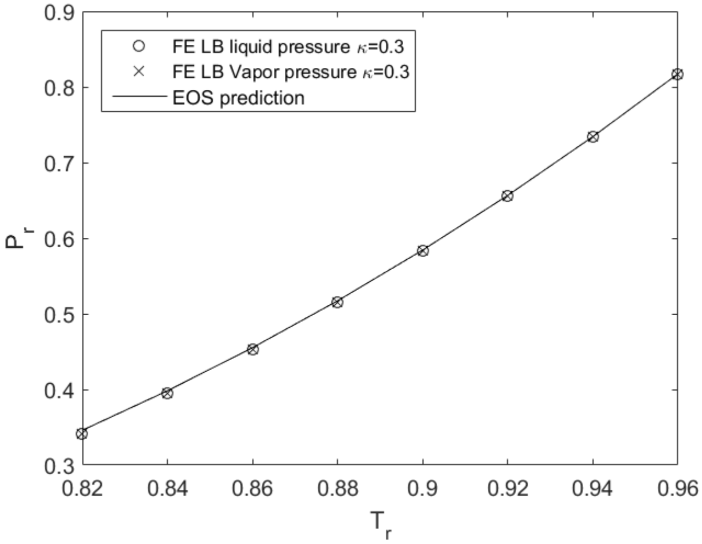

Figure B.2 Saturation pressures of CS fluid at various reduced temperatures with a flat interface using the FE model of Swift et al. (1995) with κ = 0.3.

Using $\kappa = 0.3$, we characterized Laplace pressures of spherical bubbles and drops of different interface curvatures given by the FE model. Computational domain and initialization procedure are the same as those presented in Section 6.2.2. As Figure B.3 shows, saturation pressures of the liquid phase were higher and lower than those in the flat-interface cases, respectively, in droplet and bubble cases. Saturation pressures of the vapor phase increased with decreasing droplet size and decreased with decreasing bubble size. These observations are consistent with those presented in Section 6.2.2 from the pseudopotential model. Figure B.4 indicates that Young-Laplace equation is satisfied. Obtained temperature-dependent interfacial tensions demonstrated a linear relation between log (σ) and log $(\rho_l - \rho_v)$ with a slope of 2.97 (Figure B.5). Note that the slope of this relation was 3.02 when using the β-pseudopotential model.

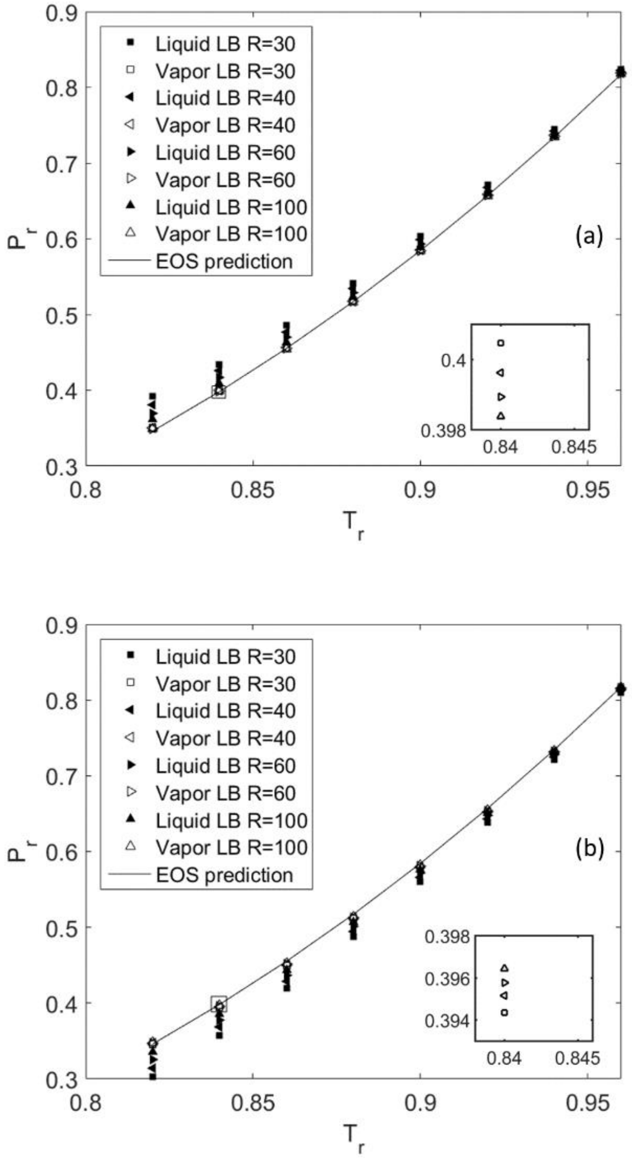

Figure B.3 Saturation pressures of liquid and vapor phases of CS fluid from simulations of droplets (a) and bubbles (b) using the FE model of Swift et al. (1995).

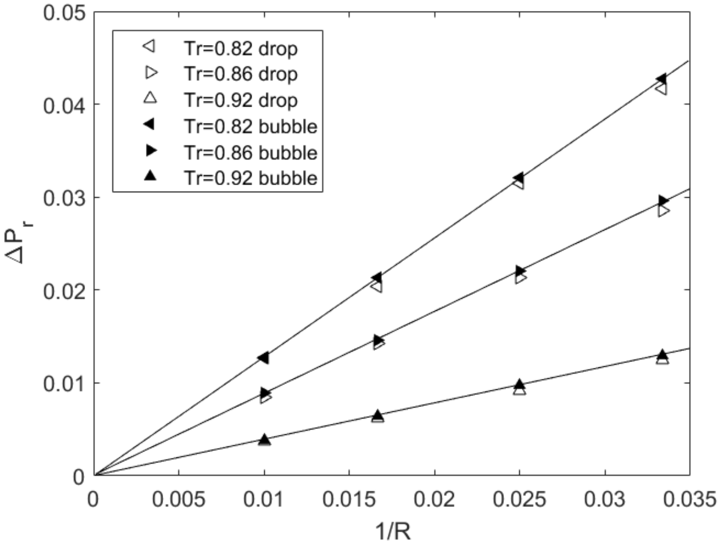

Figure B.4 Verification of Young-Laplace equation.

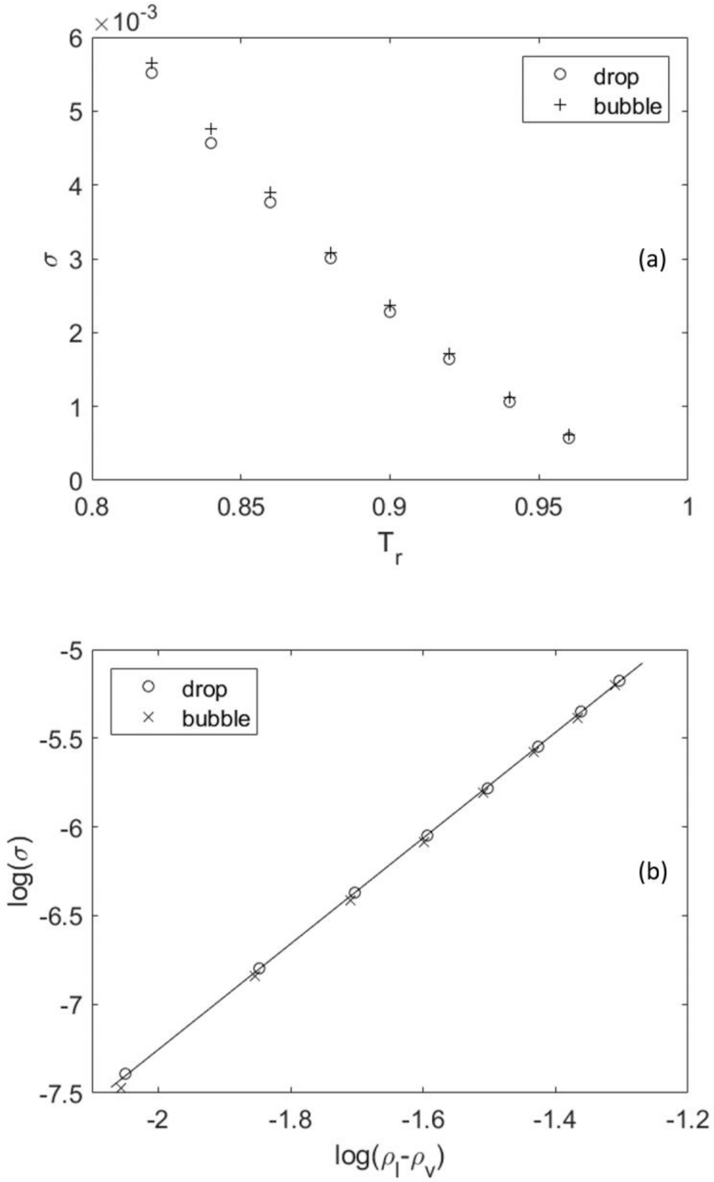

Figure B.5 Temperature-dependent interfacial tensions of CS fluid using the FE model of Swift et al. (1995) (a) and inspection of their alignment with the parachor model (b).

Simulated saturation vapor pressures in different droplet and bubble cases were then compared to those predicted by Kelvin equation in Figure B.6 and B.7. Discrepancies were observed at all reduced temperatures. In droplet cases, at the two higher temperatures

(T_r = 0.94 and 0.90) the slopes of $ln\ (P^{\alpha}/P_{vp})$ to $1/r$ were close to the predictions of Kelvin equation. The intercepts, however, were not zero as required by Kelvin equation. At low temperatures (T_r = 0.86 and 0.82), both slopes and intercepts showed rather significant deviations from Kelvin equation. In bubble cases, except at the highest temperature, neither the slope nor the intercept was in good agreement with Kelvin equation. The saturation vapor pressures from the β-pseudopotential model were also plotted in Figure B.6 and B.7. It is seen that results from the β-pseudopotential model are usually in better agreement with Kelvin equation than those from the FE model, especially at low temperatures.

The ability of these models to simulate Kelvin equation seems to be tied to the accuracy of densities and the thickness of interfaces. When temperature is low, vapor densities from LB simulations often do not match well with those from Maxwell construction across a flat interface. In the pseudopotential model, β was tuned to reduce the errors in vapor densities at low temperatures, and Kelvin equation was matched. In the FE model, the errors in vapor densities were larger than those from the pseudopotential model at the same temperature. For instance, at T_r = 0.82, the error in the vapor density from the β-pseudopotential model was 0.1% and that from the FE model was 1.9%. When temperature is low, there is also a reduction of interface thickness that leads to poorer isotropy or more distinct lattice effect. It was found that interface thickness from the FE model is thinner than that from the β-pseudopotential model at the same reduced temperature. For example, at T_r = 0.82, interface thickness was 6 lattices from the FE model and 9 lattices from the pseudopotential model. The relatively poor performance of the FE model in recovery of Kelvin equation, therefore, could be attributed to both factors: lack of accuracy in prediction of vapor density and lack of isotropy when interface becomes thin. Improving vapor density prediction of FE LB models, using parameters that can maintain the thickness of the interface, or employing LB models of higher isotropy should have the potential to improve consistency with Kelvin equation, at least at high temperatures.

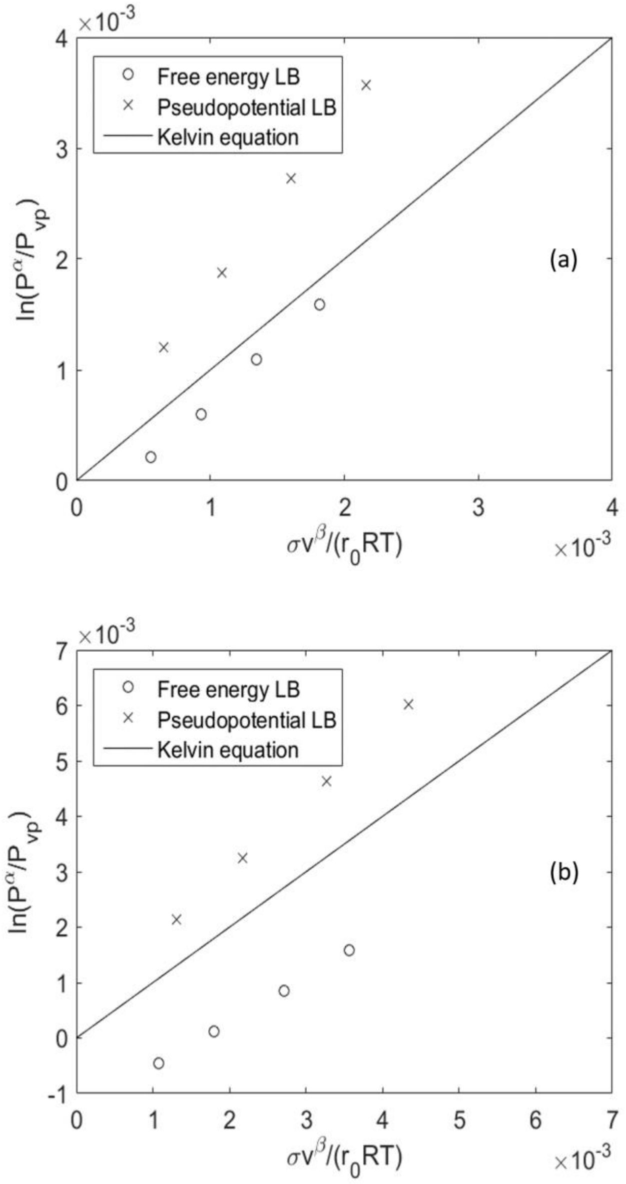

Figure B.6 Simulated saturation vapor pressures from the FE model and the β-pseudopotential model from droplet cases. Kelvin equation is represented by the solid line. (a) T_r = 0.94; (b) T_r = 0.90; (c) T_r = 0.86; (d) T_r = 0.82.

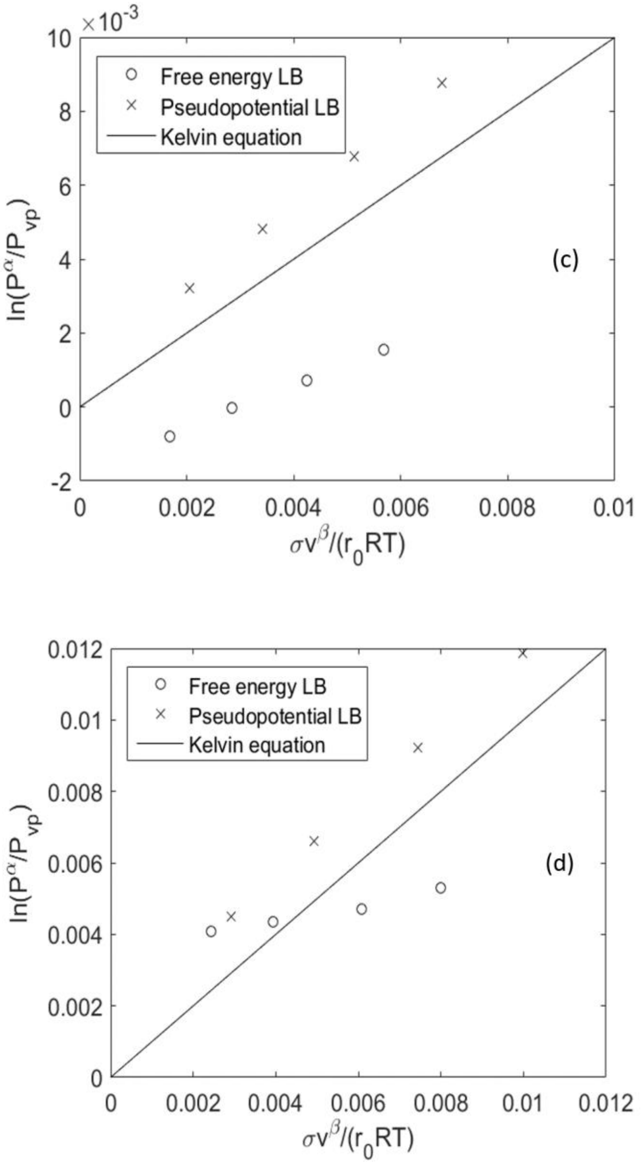

Figure B.6 Continued.

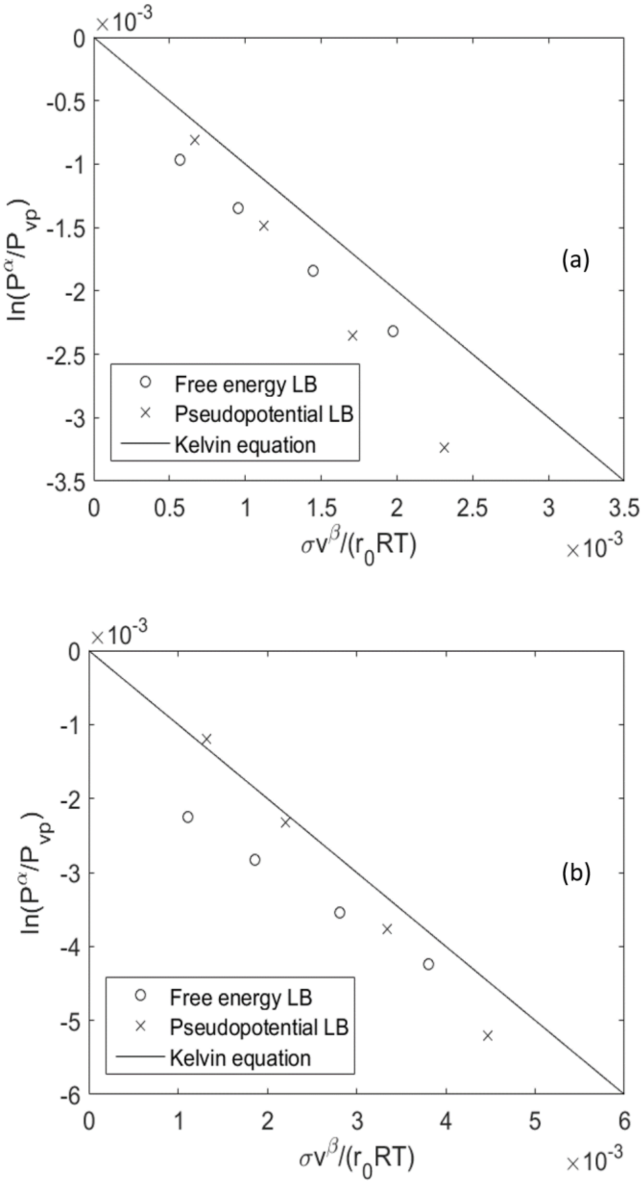

Figure B.7 Simulated saturation vapor pressures from the FE model and the β-pseudopotential model from bubble cases. Kelvin equation is represented by the solid line. (a) T_r = 0.94; (b) T_r = 0.90; (c) T_r = 0.86; (d) T_r = 0.82.

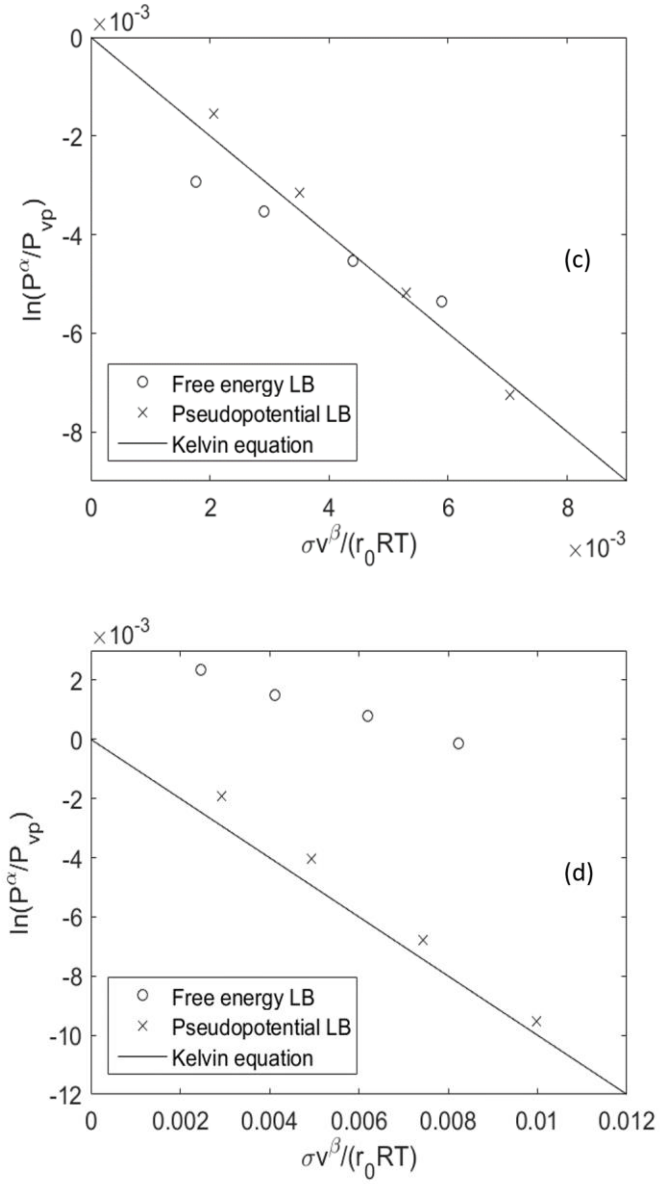

Figure B.7 Continued.

In Section 6.2.3, we showed that the lattice spacing of the pseudopotential LB model should be on the order of several molecular diameters when scaled using the interfacial tension of the co-existing phases. Similarly, by comparing the interfacial tensions of the FE LB fluid to those of a real fluid (Eqn. (6.8)), the intrinsic length scale of the lattice spacing of the FE LB model can be obtained. Figure B.8 shows that the intrinsic length scales of the FE model are slightly larger than those of the pseudopotential model when the real fluid is taken to be water. Derived thicknesses of vapor-liquid interface in real units from pseudopotential and FE models are very close as expected of the scaling procedure. These comparisons further support that these lattice Boltzmann methods simulate nano-scale liquid-vapor equilibriums based on their scaled interfacial properties. The length scales of the FE model when parameters of other pure substances are used are presented in Figure B.9.

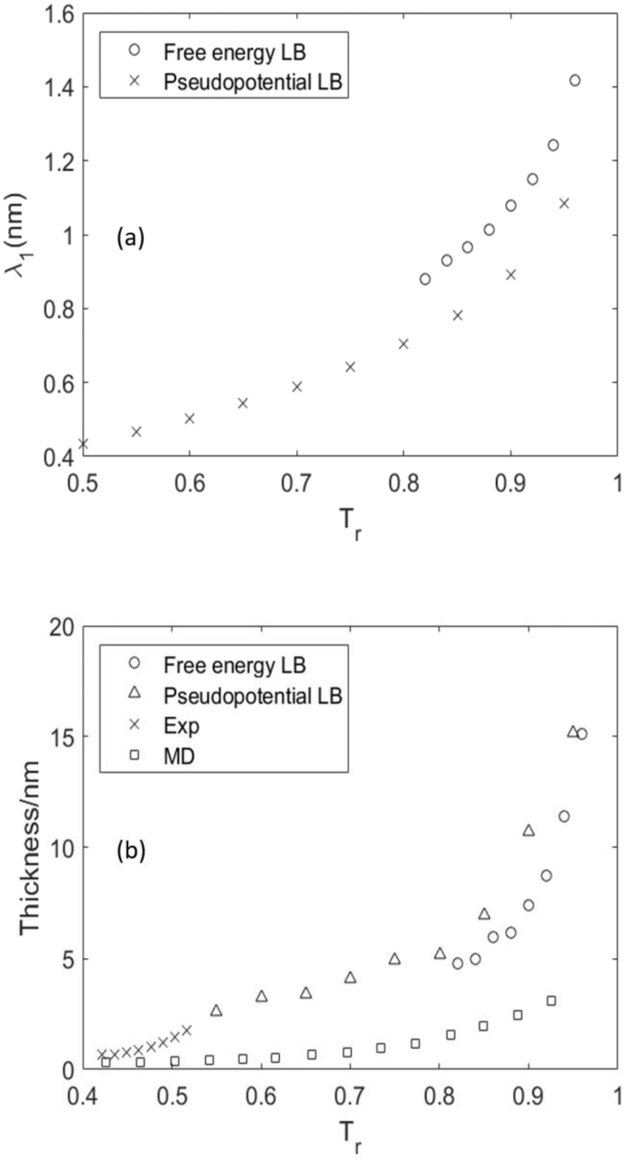

Figure B.8 Intrinsic lengths of lattice spacing (a) and interface thicknesses (b) using the FE model when simulating water.

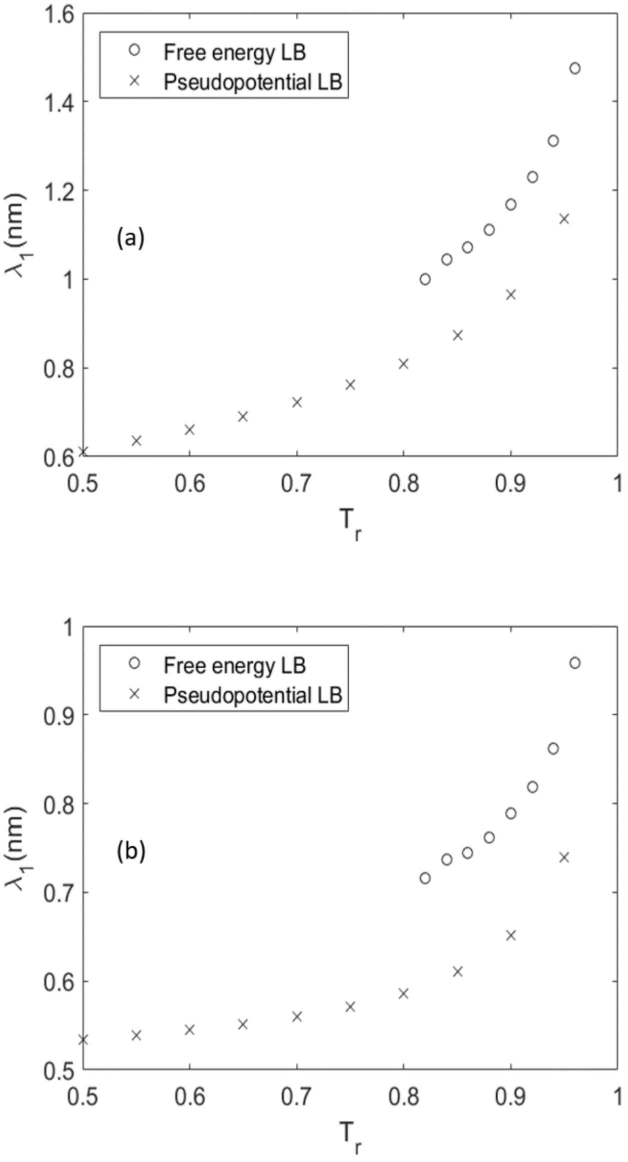

Figure B.9 Intrinsic lengths of lattice spacing when simulating methane (a), ethane (b), carbon dioxide (c) and nitrogen (d) using the FE model.

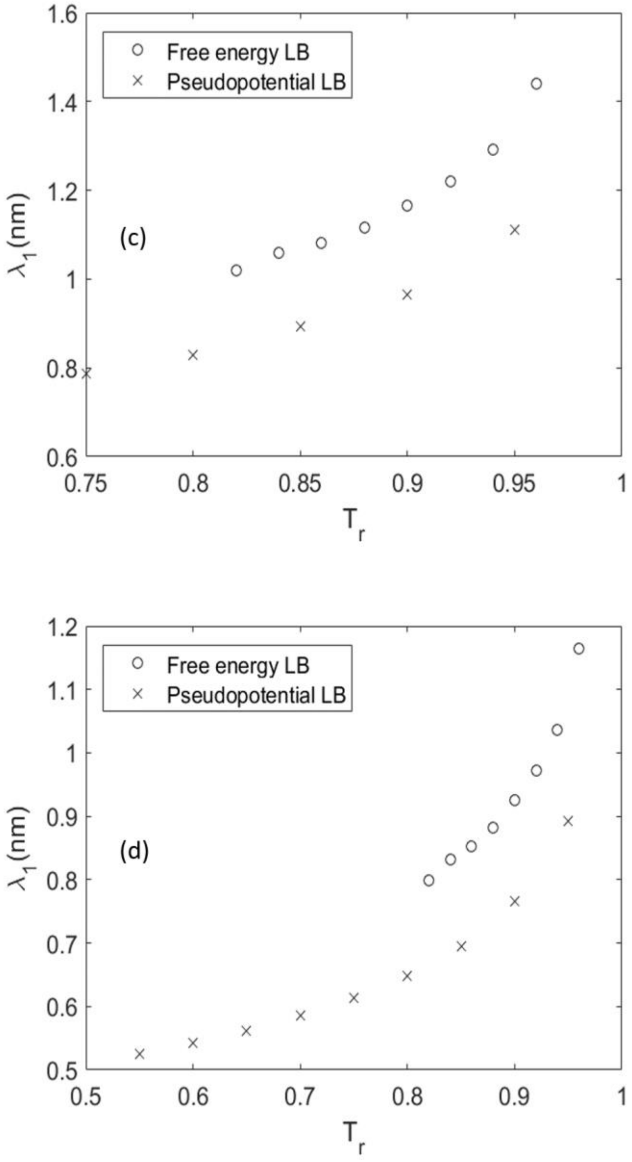

Figure B.9 Continued.